BRNO UNIVERSITY OF TECHNOLOGY
VYSOKÉ UČENÍ TECHNICKÉ V BRNĚ

FACULTY OF ELECTRICAL ENGINEERING AND COMMUNICATION
FAKULTA ELEKTROTECHNIKY
A KOMUNIKAČNÍCH TECHNOLOGIÍ

DEPARTMENT OF MICROELECTRONICS
ÚSTAV MIKROELEKTRONIKY

GECKO MIMICKING SURFACES
MIKROSTRUKTURY MIMIKUJÍCÍ POVRCH TLAPKY GEKONA

MASTER'S THESIS
DIPLOMOVÁ PRÁCE

AUTHOR — **Bc. Peter Fecko**
AUTOR PRÁCE

SUPERVISOR — **Ing. Jan Pekárek, Ph.D.**
VEDOUCÍ PRÁCE

BRNO 2019

VYSOKÉ UČENÍ TECHNICKÉ V BRNĚ
FAKULTA ELEKTROTECHNIKY A KOMUNIKAČNÍCH TECHNOLOGIÍ

Diplomová práce

magisterský navazující studijní obor **Mikroelektronika**
Ústav mikroelektroniky

Student: Bc. Peter Fecko ***ID:*** 173643
Ročník: 2 ***Akademický rok:*** 2018/19

NÁZEV TÉMATU:

Mikrostruktury mimikující povrch tlapky gekona

POKYNY PRO VYPRACOVÁNÍ:

Navrhněte a pomocí dostupných technologií vytvořte mikrostruktury mimikující povrch tlapky gekona. Tyto mikrostruktury modifikujte pomocí vhodného crosslinkeru (SiO2-APTES/GTA) tak, aby na ně bylo možné navázat keratin. Na závěr změřte a vyhodnoťte mechanické vlastnosti vytvořených a modifikovaných mikrostruktur např. pomocí mikroskopie atomárních sil (AFM).

DOPORUČENÁ LITERATURA:

According to recommendations of supervisor

Termín zadání: 4.2.2019 ***Termín odevzdání:*** 21.5.2019

Vedoucí práce: Ing. Jan Pekárek, Ph.D.
Konzultant:

doc. Ing. Lukáš Fujcik, Ph.D.
předseda oborové rady

BRNO UNIVERSITY OF TECHNOLOGY
FACULTY OF ELECTRICAL ENGINEERING AND COMMUNICATION

Master's Thesis

Master's study field **Microelectronics**
Department of Microelectronics

Student: Bc. Peter Fecko ***ID:*** 173643
Year of study: 2 ***Academic year:*** 2018/19

TITLE OF THESIS:

Gecko mimicking surfaces

INSTRUCTION:

Design and use available technologies to create microstructures that mimic surface of gecko feet. Modify these microstructures using a suitable crosslinker (SiO2-APTES/GTA) so that keratin could be bound to them. Finally, measure and evaluate the mechanical properties of those manufactured and modified microstructures, e.g. using atomic force microscopy (AFM).

REFERENCE:

According to recommendations of supervisor

Assigment deadline: 4. 2. 2019 ***Submission deadline:*** 21. 5. 2019

Head of thesis: Ing. Jan Pekárek, Ph.D.

doc. Ing. Lukáš Fujcik, Ph.D.
Subject Council chairman

ABSTRACT

Adhesive capabilities of a gecko lizard have been the subject of many studies and an inspiration for many artificial imitations and inventions. This work proposes a design version of synthetic gecko structures in a form of micro-pillars, that would have similar adhesion capabilities as gecko setae. Structures made of Parylene C polymer have been created using photolithography and silicon etching techniques. Following focus was on various methods of surface modifications and characterisation of these structures to determine the adhesion forces on their surface, before and after modifications.

ABSTRAKT

Adhezní schopnosti gekona byly předmětem mnoha studií a inspirací pro vytvoření mnoha napodobenin. Tato práce navrhuje vlastní verzi umělých gekoních struktur ve tvaru mikroskopických pilířů, které by vykazovaly adhezní vlastnosti srovnatelné s tlapkou gekona. Vyrobeny byli struktury z polymeru Parylen C pomocí fotolitografie a technik na leptání křemíku. Dalším cílem bylo různými metodami pro modifikaci povrchu a charakterizaci vytvořených struktur, které určí adhezní síly těchto povrchů, před a po modifikacích.

KEYWORDS

gecko adhesion, adhesive setae, biomimetics, van der Waals force, reactive ion etching, XeF_2 etching, Parylene C, atomic layer deposition (ALD), adhesion promotors, scanning electron microscopy (SEM), contact angle measurement, atomic force microscopy (AFM)

KLÍČOVÁ SLOVA

adheze gekona, adhezní struktury, biomimetika, van der Waalsovy síly, leptání reaktivní plasmou, leptání v XeF_2, Parylen C, depozice atomárních vrstev (ALD), adhezní promotéry, rastrovací elektronová mikroskopie (SEM), měření kontaktního uhlu, mikroskopie atomárních sil (AFM)

BIBLIOGRAPHIC CITATION

FECKO, P. Gecko mimicking surfaces. Brno: Vysoké učení technické v Brně, Fakulta elektrotechniky a komunikačních technologií, 2019. 52 s. Vedoucí diplomové práce Ing. Jan Pekárek, Ph.D..

Prohlášení autora o původnosti díla

„Prohlašuji, že svou diplomovou práci na téma Mikrostruktury mimikující povrch tlapky gekona jsem vypracoval samostatně pod vedením vedoucího diplomové práce a s použitím odborné literatury a dalších informačních zdrojů, které jsou všechny citovány v práci a uvedeny v seznamu literatury na konci práce.
Jako autor uvedené diplomové práce dále prohlašuji, že v souvislosti s vytvořením této diplomové práce jsem neporušil autorská práva třetích osob, zejména jsem nezasáhl nedovoleným způsobem do cizích autorských práv osobnostních a jsem si plně vědom následků porušení ustanovení § 11 a následujících autorského zákona č. 121/2000 Sb., včetně možných trestněprávních důsledků vyplývajících z ustanovení části druhé, hlavy VI. díl 4 Trestního zákoníku č. 40/2009 Sb.

.

V Brně dne: 21. května 2019 ……

Peter Fecko, podpis

ACKNOWLEDGEMENT

I would like to thank my supervisor Ing. Jan Pekárek, Ph.D for an effective methodological, pedagogical and technical support during my work at this master's thesis. I would also like to thank doc. Ing. Pavel Neužil Dr., DSc. for an opportunity to work on his project.

My thanks goes to my parents, and friends, who encouraged me during my studies and writing of this thesis.

Brno ....

(author's signature)

SIX research centre
sensor, information and communication systems

Faculty of Electrical Engineering
and Communication

Brno University of Technology
Technicka 12, CZ-61600 Brno, Czechia

http://www.six.feec.vutbr.cz

Experimentální část této diplomové práce byla realizována na výzkumné infrastruktuře vybudované v rámci projektu CZ.1.05/2.1.00/03.0072
Centrum senzorických, informačních a komunikačních systémů (SIX)
operačního programu Výzkum a vývoj pro inovace.

MINISTERSTVO ŠKOLSTVÍ, MLÁDEŽE A TĚLOVÝCHOVY

EVROPSKÁ UNIE
EVROPSKÝ FOND PRO REGIONÁLNÍ ROZVOJ
INVESTICE DO VAŠÍ BUDOUCNOSTI

2007–13
OP Výzkum a vývoj pro inovace

CEITEC
Středoevropský technologický institut
BRNO | ČESKÁ REPUBLIKA

VYSOKÉ UČENÍ TECHNICKÉ V BRNĚ

„Část práce byla provedena za podpory výzkumné infrastruktury CEITEC Nano (ID LM2015041, MŠMT, 2016–2019), CEITEC Vysoké učení technické v Brně.“

MINISTERSTVO ŠKOLSTVÍ, MLÁDEŽE A TĚLOVÝCHOVY

EVROPSKÁ UNIE
EVROPSKÝ FOND PRO REGIONÁLNÍ ROZVOJ
INVESTICE DO VAŠÍ BUDOUCNOSTI

2007–13
OP Výzkum a vývoj pro inovace

TABLE OF CONTENTS

INTRODUCTION

Many centuries ago, philosophers during their studies of nature noticed how geckos are capable of climbing almost any surface. In modern studies, scientists try to understand the principals behind gecko adhesion and how does the smart adhesive, that are the toe pads of gecko, work in a micro scale. Geckos are also capable of detaching their pads in milliseconds while running on vertical and inverted surfaces.[1] Last decade there have been numerous successful attempts (at some degree) of creating surfaces inspired by this animal [2, 3], or making use of such structures as a form of dry adhesives [4-6], that in the future could effectively replace traditional (wet) adhesives, which are used today.

Past studies propose, that the adhesion forces, which play a role in clinging ability of the Tokay Gecko (*Gekko Gecko)* animal, are due to capillary forces or van der Waals forces. These are conventionally considered as main sources of adhesion. But a recent study suggests, that fine fibrillar features of gecko toes exchange significant numbers of electric charges with the contacted substrate via the contact electrification (CE) phenomenon. They demonstrate, that the contribution of CE effectively dictates the strength of gecko adhesion [7]. However, this work does not argue, which forces of adhesion (van der Waals, capillary or those caused by CE) are prevalent, but only deals with creating gecko mimicking structures and their characterization using available analytical tools. Regardless, all three types of forces will be discussed in the following chapter.

The main aim of the first chapter is also to clarify forms of surface adhesion of some animals and insects, and the microscopic texture of gecko feet specifically. Secondly, three main ideas of factors, which play some role in adhesion forces of the surface contact are explored.

The second chapter discusses technological and analytical options that are utilized in fabrication of the design inspired by gecko features. The whole process is very similar to the micro-electro-mechanical systems (MEMS) fabrication processes, therefore materials, such as silicon (wafers) are used, lithography techniques are studied, ways of etching the substrates and deposition of other useful materials and surface adhesion modification methods are described. The chapter is concluded by which imaging and measurement techniques were used for sample characterisation.

Third chapter explains specific steps of fabrication using tools described in previous chapter. It starts with the proposed topology of gecko mimetics and a step-by-step production of samples with measurable structures. Also, the results are shown on form of magnified images of the microscopic structures.

The last chapter deals with measuring adhesion properties of the created structures using contact angle method and atomic force microscopy (AFM). The results are discussed in the ending chapter.

1 ADHESION PROPERTIES OF GECKO SETAE

Besides the tokay gecko, many other species of animals evolved forms of adhesive organs on their foot in order to effectively adhere to surfaces present in their environment, like trees or other plants. These organs usually form small pads and based on their functionality, they come in two designs as 1) pads with relatively smooth surface and 2) pads covered with micron or sub-micron sized setae (hairs) of high density per pad. [8]

1.1 Advantages of "hairy" pad design

1) Rough surface compatibility

There is no practical difference of hairy adhesive surfaces and those made of solids on a smooth surface. But when the roughness of the surface starts increasing, the effective contact area between the adherents decreases and a smooth solid pad has trouble adhering to the topology of the surface if it is not made of soft material (which has low elastic modulus – material's resistance to elastic deformation). But these soft materials are more susceptible to creep, degradation (wear) and contamination. By bending and stretching of setae, the hairy pads behave as these soft solids (their apparent elastic modulus is low) even though they are made of relatively hard materials. The advantage of the micro- or nanoscale sized tips is also, that they easily adapt to the topography of rough surface of a hard material on a microscale and form an intimate surface contact, which increases adhesion and frictional forces (see fig. 1-1). [8]

2) Self-cleaning properties

Geckos keep their feet clean without any active grooming. The morphology of a hairy pad may be less contaminated with small particles, because of greater adhesion of these particles to the surface, than to the very fine tips of gecko spatula. So, the gecko setae are cleaned with every step the animal takes. [8]

3) Effortless and controllable detachment

Gecko setae were observed to generate large detachment forces by only being slightly pulled in proximal direction with a small preload by the animal. The adhesion forces decreased after the angle between setae and the surface exceeded the critical value of 30° and could be easily detached. This can help animals to quickly switch between attachment and detachment by making gross limb movements. [8]

4) Maximised adhesion

It has been confirmed, that even on a smooth substrate, a hairy pad morphology may maximise adhesion, despite the smaller contact area. [8]

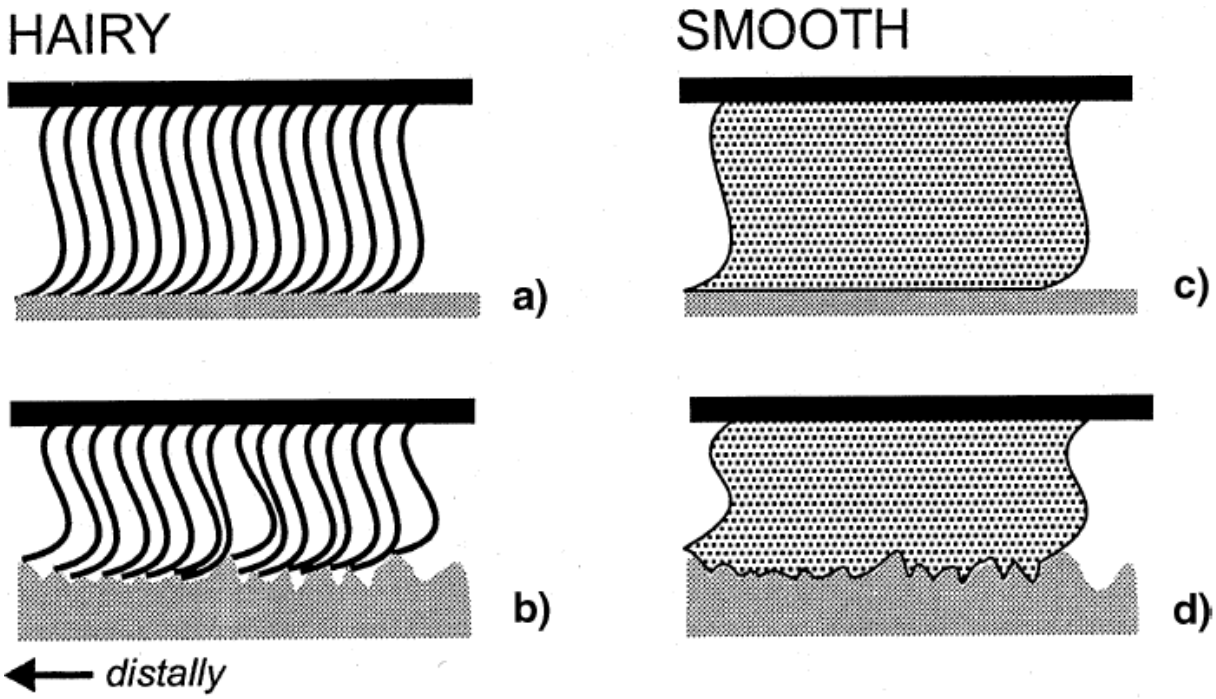

Fig. 1-1. Functionality difference between (a, b) "hairy" and (c, d) "smooth" pad designs on (a, c) smooth and (b, d) rough surface profile. [9]

1.2 Gecko toe pads

Gecko's extraordinary ability to stick to most of the surfaces is thanks to uniform microarrays of hair like setae formed from β-keratin of which his toes are covered in series of lamellae. Each seta branches to form a nanoarray of hundreds of spatula structures, that can essentially make ultimate contact with the surface. [1]

The gecko setae: (1) are directional, (2) attach strongly with minimal preload (pushing force), (3) detach quickly and with minimal effort, (4) stick to nearly every material, (5) exhibit rate-dependent adhesion, (6) do not stay dirty or (7) self-adhere, and by default (8) are non-sticky. [1]

A single seta of the tokay gecko is approximately 110 μm in length and 4,2 μm in diameter, they are also uniformly distributed on lamellae. Setae branch a number of times at the tips into 100-1000 terminal structures known as spatulae. These are approximately 0,2 μm long with a similar width at the tip. All is shown on fig. 1-2. [1]

It was estimated, that two front feet of Gecko can withstand ~20 N of force parallel to the surface across 227 mm^2 of toe-pad area. Individual setae have proved both less sticky and much more sticky than predicted by whole-animal measurements under varying experimental conditions, implying that attachment and detachment in gecko setae are mechanically controlled. [1]

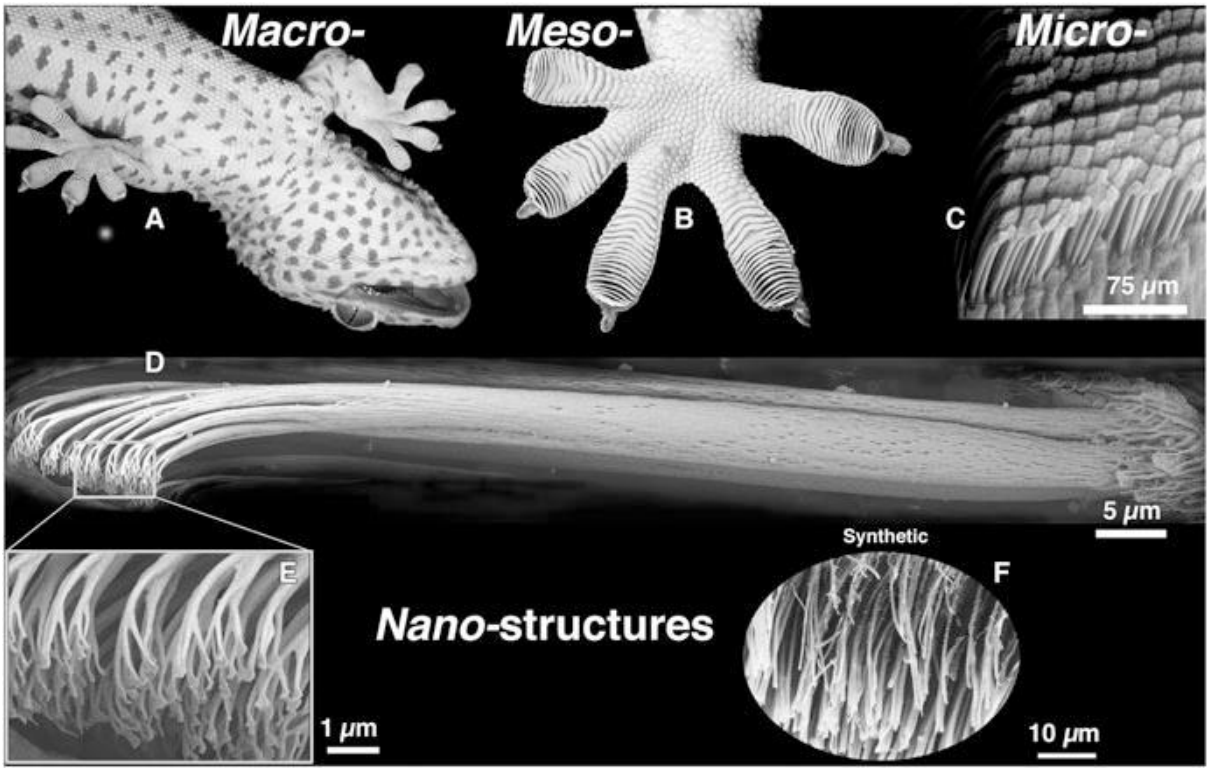

Fig. 1-2 Structural hierarchy of the gecko adhesive system. (a) Gecko climbing a vertical surface; (b) view on the foot of the tokay gecko (adhesive lamellae visible); (c) setae arranged in a grid like pattern; (d) detail on an individual gecko seta; (e) close-up on a nanoscale array of hundreds of spatula tips of a single seta; (f) synthetic spatulae fabricated from polyimide using nanomolding. [1]

1.3 Effective forces

The beliefs about what primarily causes adhesion of gecko setae vary among researchers. There is no clear consensus, but three main forces are believed to have some level of impact on the overall adhesion: (1) van der Waals forces, (2) capillary forces, and (3) electrostatic forces. But the question about which from these factors is dominant is still a subject of today's research.

1.3.1 Van Der Waals force

This force is weak and becomes significant only at a very short distance. If we take very small particles (<1 μm), this attraction force whereas the influence of gravity becomes negligible. Taking two nanoparticles of same radii, that are separated by a distance *S* the simplified expression of van der Waals attraction is:

$$\Phi_{\mathrm{A}} = -\frac{A_{\mathrm{i}} \cdot r}{12 \cdot S}, \tag{1}$$

where the negative sign represents the attraction nature of the interaction, the r is the radius of one sphere, and the A_{i} is a Hamaker constant (magnitude on the order of 10^{-19} to 10^{-20} J). [10]

Table 1-1: Hamaker constants of some common materials. [10]

Materials	Metals	Gold	Oxides	Al_2O_3
A_i [10^{-20} J]	16,2-45,5	45,3	10,5-15,5	15,4
Materials	SiO_2 (fused)	SiO_2 (quartz)	Polymers	Water
A_i [10^{-20} J]	6,5	8,8	6,15-6,6	4,35

Table 1-2: Variations of equation (1) depending on different assumptions about two particles. [10]

Particles	Φ_A	
Two spheres of unequal radii, r_1 and r_2 (r_1, r_2 >> S)	$-\frac{A \cdot r_1 \cdot r_2}{6 \cdot S \cdot (r_1 + r_2)}$,	[J]
Two parallel plates with thickness of δ	$\frac{-A}{12 \cdot \pi} \cdot \left(\frac{1}{S^2} + \frac{1}{(2\delta + S)^2} + \frac{1}{(\delta + S)^2}\right)$,	[J/m²]
Two blocks	$\frac{-A \cdot r}{12 \cdot S}$,	[J/m²]

1.3.2 Capillary forces

At microscale, the Young-Laplace equation is used to define the equilibrium of liquid surface (e.g., capillary surface) [11]:

$$\Delta p = \gamma \left(\frac{1}{R_1} + \frac{1}{R_2}\right) \quad , \tag{2}$$

where γ is the liquid surface tension (liquid-air surface), Δp is the pressure difference across the liquid surface, and R_1, R_2 are the principal radii of surface curvature. In a narrow tube (with radius a), the liquid surface will be a portion of spherical surface (with radius R). The relation between R and a is a cosine function of the liquid-solid contact angle Θ ($\cos \Theta = a.R^{-1}$). Thus, the equation (2) can be modified as [11]:

$$\Delta p = \frac{2\gamma \cdot \cos\theta}{a} \quad . \tag{3}$$

The surface tension represents the potential energy change caused by per unit liquid surface area change, which is typically considered to be a constant, e.g., the γ of water is measured as 72 $mN.m^{-1}$ at room temperature. It is also reported that the surface tension of water decreases with the temperature, and slightly increases with the electrolyte ion concentration. Currently, the Young-Laplace equation is also widely used to describe the capillary pressure when the channel/pore size is down to nanoscale. [11]

1.3.3 Contact electrification

A spontaneous charge transfer between materials in contact can increase adhesion between them. To better describe this situation, two smooth dissimilar insulating materials, e.g. mica and fused silica (both have near atomic smoothness) are brought into contact and separated, while the charge transferred during contact and of the resulting electrostatic force, respectively, are directly measured by two electrometers. To determine the sign and quantity of charge on the front surfaces (those in contact), electrical contacts are coated with silver (see fig. 1-3). [12]

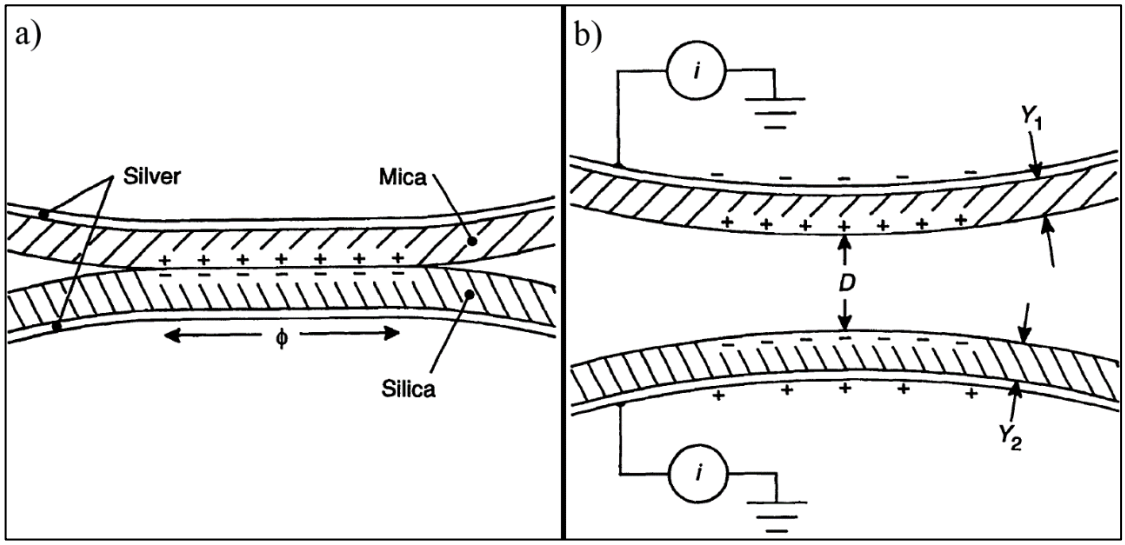

Fig. 1-3 Schematic arrangement of thin solid film (a) in contact (of size ϕ); (b) upon separation. [12]

In calculating the force, one must consider four layers of charge: the two front surfaces plus two grounded silver electrodes a few micrometres behind them. The field across the gap decreases even with constant charge on the front surfaces. the force per unit area at surface separation D is given by

$$F_{\mathrm{A}} = -\frac{\sigma_{\mathrm{s}}^2}{2\epsilon_{\mathrm{o}}}\left(\frac{B}{B+D}\right)^2 \tag{4}$$

where σ_s is the magnitude of charge per unit area, ϵ_o is the permittivity of vacuum and $B = Y_1/K_1 + Y_2/K_2$, with Y_1, Y_2 and K_1, K_2, *a*s the thicknesses and relative dielectric constants of the two substrates.[12]

The analysis of the distance dependence of electrostatic force is possible if certain simplifying assumptions are made: (1) surface deformation is ignored (in reality, the electrostatic attraction is strong enough to deform materials elastically), (2) the two surfaces are modelled as infinite parallel plates ($D << \phi$), and (3) the charge density of the plates is assumed to be uniform and equal to the total charge divided by the maximum contact area. [12]

2 FABRICATION AND ANALYTICAL TECHNIQUES

2.1 Lithography

To implement the fine design proportions from previous chapter onto a silicon wafer substrate a set of very accurate lithography methods are required. This includes making a mask with the design imprint (positive or negative), then transferring the design onto an appropriate substrate, e.g. coated with a photoresist film that will be later developed.

With some lithography techniques it is possible to implement a desired image onto the substrate directly and with precision in nanoscale (nanolithography). But this approach is very time consuming and usually unnecessary. A better approach is to transfer the image with high precision and accuracy onto a glass mask carrying a durable and thin metallic film. This mask carrier can be then used repeatedly on sample substrates using faster lithographic methods while a high level of precision is preserved.

2.1.1 Photolithography

Fig. 2-1 shows basic steps of photolithography process, consisting of using the mask carrier to transfer a desired image onto a photosensitive film (photoresist - PR). The areas exposed to light with a certain level of energy (wavelength and dosage) change their chemical properties. The exposed material can be rendered more soluble in some developing solvent (developer), thereby producing a positive image of the mask (the photosensitive material is then called a positive PR) or in case it is less soluble in the developing solvent, it produces a negative tone image of the mask (negative PR). Conventional photolithography is capable of fabricating features of 200 nm and above. [10]

The minimum size of individual elements, or in other words, the maximum resolution of photolithography is limited by diffraction. The diffraction is a result of light being projected into places of geometrical shadow under the carrier mask. The uniformity of exposure close to the edges is compromised, and the developed line edges of the resulting pattern become blurred or diffused at the resist surface. This effect can be partially reduced by bringing the carrier mask in contact with the PR surface. Proximity can be enhanced by creating vacuum in-between (uniformity and cleanliness of the PR surface is very critical). [10]

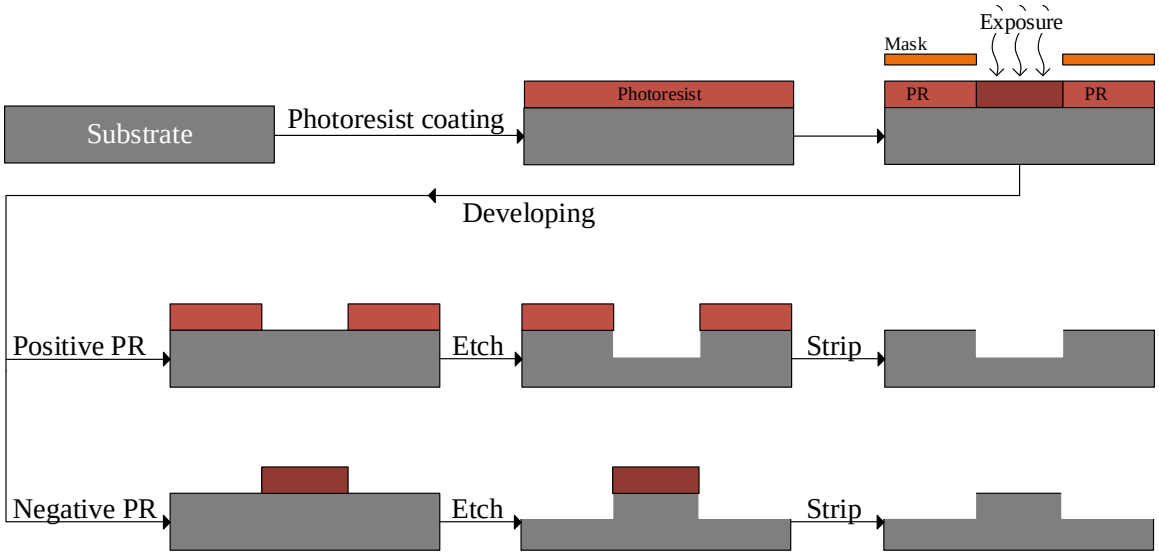

Fig. 2-1 Basic scheme of the photolithographic process steps – transferring images onto a surface using a mask.

Higher resolutions can be obtained using light with shorter wavelengths and lens systems with large numerical apertures, one can obtain. Deep Ultra-Violet lithography (DUV) based on exposure at wavelengths below 300 nm allows one to obtain patterns with a minimal size of ~100 nm. For this, mercury arc lamps and excimer lasers (higher resolutions) are used. Excimer lasers are gas-based light systems filled with inert and halide gases (Kr, Ar, Xe, F and Cl). Examples of excimer lasers are: KrCl and KrF (wavelengths 222 and 249 nm), ArF (193 nm) and F_2 (157 nm). Extreme UV (EUV) lithography with wavelengths of 11-13 nm has also been explored for fabricating features with even smaller dimensions of 70 nm and below. [10]

2.2 Etching of silicon and silicon dioxide

Creating structures in micro and nanoscale (e.g. MEMS, NEMS) might require a high level of etching process controllability and material versatility. Generally, we have two basic options to etch a wide range of materials: wet and dry etching. Wet etching usually requires chemical solutions and buffered etchants in liquid forms. Dry etching is done with energized plasma – gas ionized using radio frequency (RF) power sources.

Some advantages of dry etching over wet etching:

- The biggest difference is directional (anisotropic) nature of plasma technology, while wet etching is very isotropic (etching in all directions).
- Another desirable trait of plasma process is, that they are easily controllable through RF power, pressure, time, and gas selection.
- Less sensitive to atmospheric changes such as temperature, humidity, and pressure.
- Plasma etching leaves no residues and consumes less raw materials than wet etching.
- Waste product are mostly gaseous and are liberated directly into atmosphere. Most of the gases are nontoxic, but some might be very hazardous (e.g. SF_6 is a greenhouse gas). The processes don't require extensive safety trainings and are easily programmable.
- A photoresist can be used as a mask for etching patterns into hard materials. [13]

For the purposes of this work, the dry etching techniques are most suitable. The idea is to etch deep into silicon substrate using the SiO_2 and PR as masks patterned with dots. The result would be deep holes with smooth walls serving as a form for long nano-pillars mimicking Gecko spatula. Therefore, a high aspect ratio and high anisotropy is needed, those are the requirements, which wet etching doesn't meet.

2.2.1 Reactive ion etching – RIE

Reactive ion etching (RIE) is a plasma process where using RF discharge creates excited species (ions and radicals) in low vacuum. RIE etching utilizes etching of chemically active species and also physical ion bombardment of the surface. Ion bombardment is directional thanks to electrical field present, so the etching is highly anisotropic, with reduced lateral etch rate and vertical (or nearly vertical) sidewalls. It is used where narrow lines or channels or structures with high aspect ratio need to be fabricated. RIE of silicon is independent of crystal planes, and therefore any shape can be fabricated, unlike anisotropic wet etching. Deep reactive ion etching (DRIE) is an extension of RIE that enables high-rate etching of deep structures. [14]

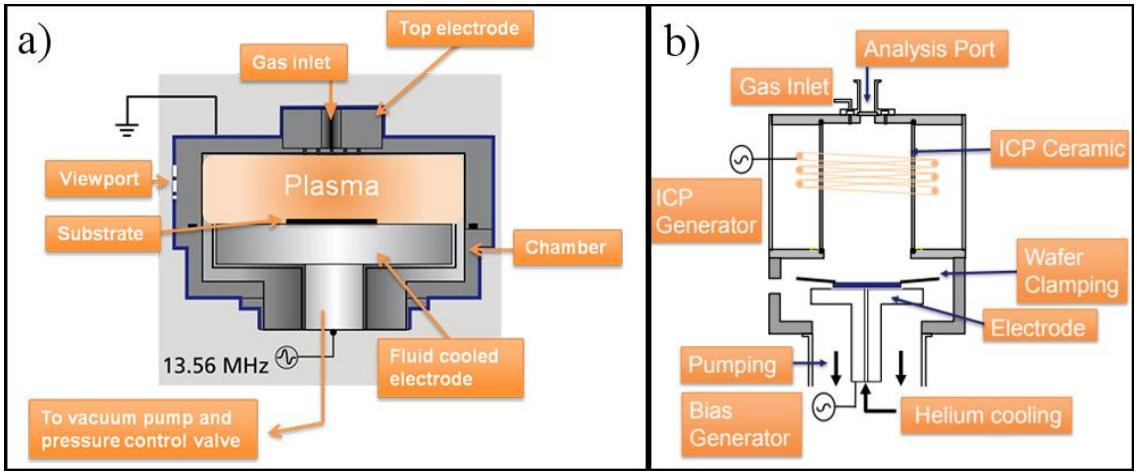

Fig. 2-2 Description of (a) capacitively coupled plasma (CCP) and (b) Inductively coupled plasma (ICP) sources. [14]

Reactive Ion Etching equipment can be made of two different power source types: capacitively coupled plasma (CCP) (fig. 2-2a) or inductively coupled plasma (ICP) (fig. 2-2b). RIE processes are usually carried out using CCP power source, where a discharge of plasma occurs between two capacitive electrodes. The bottom electrode is also a substrate chuck, so the substrates are directly exposed to plasma particles, which can be a disadvantage (decreased anisotropy). Also, the chamber needs to be pumped into high vacuum after every process and that takes time. [14]

ICP power source is found in DRIE processes. Inductively coupled plasma is ignited high above the substrate table. Because of that, this plasma equipment also requires CCP electrodes to create voltage bias for extracting and accelerating ions from ICP onto the surface of the wafer. [14] The wafer is held with a clamp against the bottom electrode, which also provides cooling for the wafer, using helium gas as a mediator. These machines usually come with a load-lock, which is pumped independently from the plasma chamber, so that it can be under high vacuum constantly. [15]

Typical highlights of (D)RIE processes:

- **Etch rate** of silicon varies from 0,1-1 μm for RIE and in DRIE it can reach rates of 10-50 μm, but it depends on actual process parameters and the HW configuration.
- **Selectivity** (etch rates of mask:etched material) – during Si etching, polymeric, metallic or silicon oxide/nitride masks can be utilised. The selectivity varies with used masks but can be from 1:1 to 10:1 for RIE and 10:1 up to 100:1.
- **Anisotropy –** determined from direction of the accelerated ions and radicals, and is better in DRIE
- **Aspect ratio** (depth:width) in RIE are limited to around 2:1 and for DRIE it can rise up to 20:1 (achieved by Bosch technique)

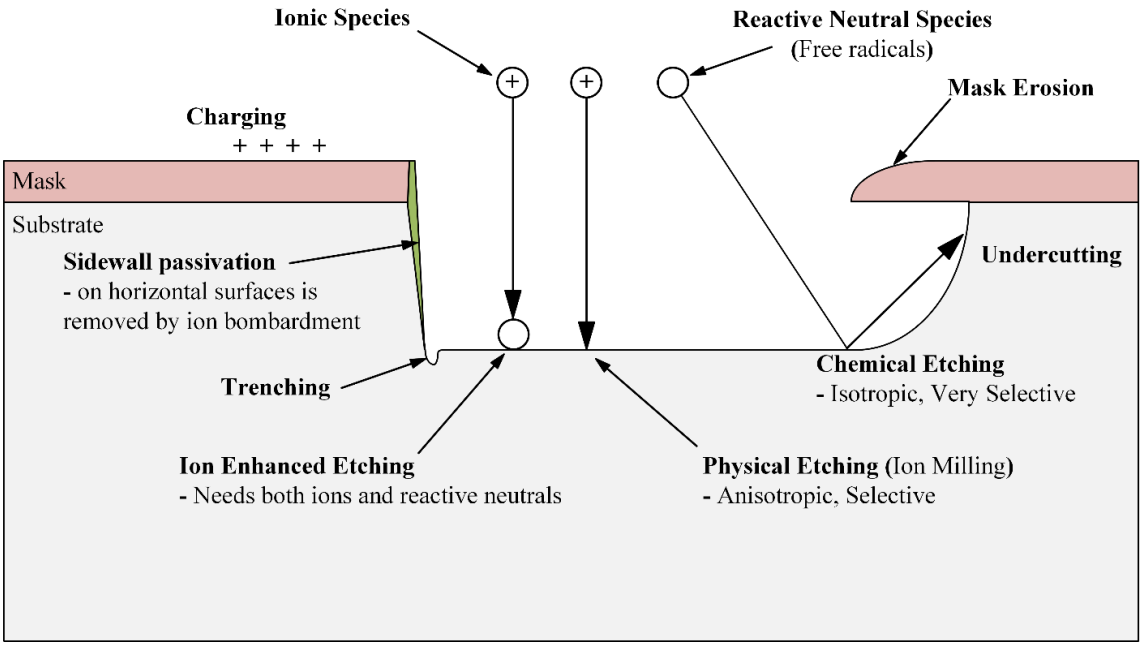

Fig. 2-3 Summary of some of the phenomena occurring during reactive ion etching.

The number of controlled parameters is an advantage, but on the other hand, it makes this process the most critical fabrication step for this work. The complexity of process dependencies during reactive plasma etching are summarized in fig. 2-3.

Materials and etching gases

Among all the materials, that could be etched with RIE, the most frequently etched are silicon, silicon dioxide/nitride, and some refractory metals (aluminium, tungsten, etc.). Silicon and its compounds can be etched in chlorine and fluorine (SF_6) plasmas, but because the chlorine gas is hazardous, it's less popular. Silicon nitride (Si_3N_4) is etched in CF_4- or SF_6- based plasmas. It is not possible to achieve selectivity nitride-silicon in fluorine plasmas, but using plasmas based on CHF_3, C_2F_6, or C_4F_8 it is possible to obtain nitride-silicon selectivities from 5:1 to 50:1. SiO_2 etching can be done using the same plasmas. [14]

As far as masks are concerned, the easiest and fastest way is to use a photoresist mask, since it is broadly used in many technological processes. The downsides of using polymeric PR are little selectivity and thermal sensitivity. In RIE plasmas the temperatures can easily range from -150°C to +450°C. Very low temperatures cause PR to form cracks and high temperatures, caused by ion bombardment, will burn the PR. Other options are "hard masks" like SiO_2 for its relatively high SiO_2-Si selectivity and metallic masks but coating them onto Si can create impurities and tension in the Si crystal. [14]

2.2.2 Deep reactive ion etching (DRIE)

The most useful and most critical process step of Gecko fabrication is etching deep holes relative to the diameter of the dot. That is why high aspect ratio is needed, and good anisotropy for perpendicular "deep drilling". Other important variables are etching rate, how big is the undercut and how smooth are the walls. Two popular DRIE techniques fulfil these requirements to some extent: Bosch process and Cryogenic process.

Bosch process

Bosch process was developed and patented by Franz Lärmer and Andrea Schilp in year 1994. On fig. 2-4 is shown a simple method for "deep drilling" called also the "switched process" and "time domain multiplexed process" It works by alternating etching steps with Si etchant gas (SF_6), that produces fluorine radicals and passivation steps, when fluorocarbon film is deposited, forming polymeric chains (c-C_4F_8). The SF_6 step is not fully anisotropic, but with the passivation layer on the sidewalls, horizontal surfaces are primarily etched due to ion bombardment. When these steps are cycled several times, it results in deep vertical sidewalls. But, as seen on the picture, the microscopic cross section shows scalloping, because of the pulsed nature of the process. [14, 15]

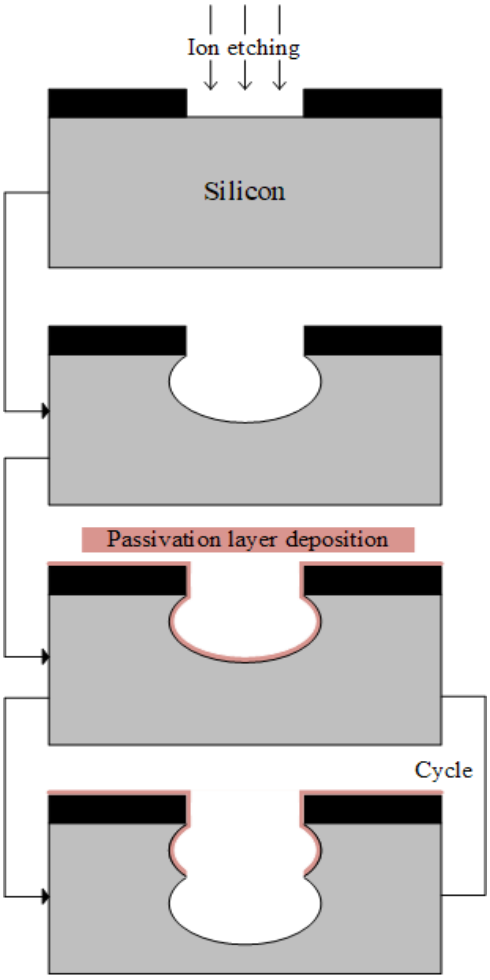

Fig. 2-4 Bosch process etching steps. The last two steps, polymer deposition and etching, are cycled until the desired depth is achieved.

The etch and passivation times are usually from 5-15 s, and changing this step durations and ratio, one can easily control the profile character, like etch rate, selectivity, profile angle and scalloping. [15]

Cryogenic process

Cryogenic RIE etching was first introduced in1988 by Tachi, Kazunori, and Okudaria. By cooling the wafer during RIE the chemical etching is reduced, improving anisotropy and sidewall smoothness. Additionally, selectivity between the mask and the etched material is increased. The reason for little chemical reactions is silicon oxyfluoride (SiO_xF_y), which inhibits lateral etching, so it can proceed downwards with accelerated ions removing the passivation layers on the bottom. Controlling the etch rate is done by changing the high concentrations of fluorine radicals in SF_6/O_2 plasma where O_2 controls the quality of passivating layer. Too much oxygen results in over-passivation and formation of so-called black silicon (silicon micro-grass). [14]

2.2.3 XeF_2 etching of Silicone

Another way of dry etching Si is in XeF_2 gas (plasma-less) – vapor-phase etch. It is completely isotropic and the etch rates are about a few microns per minute divided in several cycles of gas inflow and pumping. It's highly popular in MEMS technologies (releasing AlN/ZnO resonators, micro-mirrors, cantilevers, etc.), microfluidics (fig. 2-5), etc.

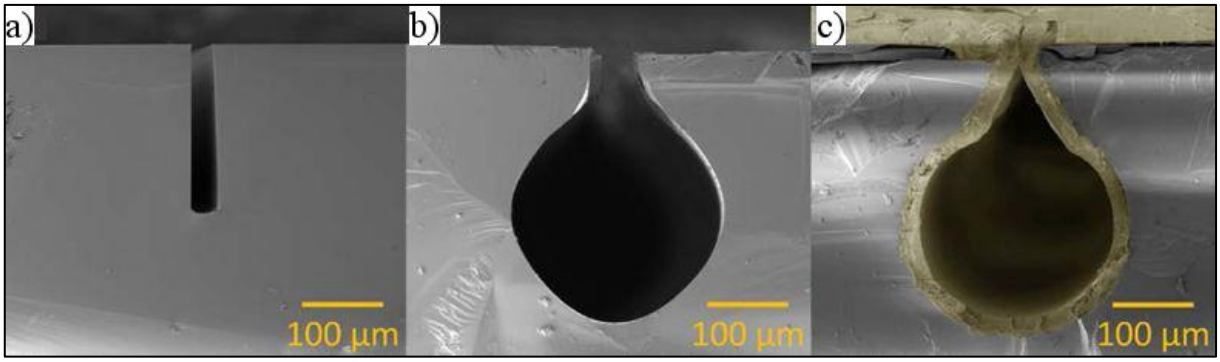

Fig. 2-5 Example of using XeF_2 gas on the (a) bottom of a silicon trench to etch (b) a buried microfluidic channel which could then be (c) closed with a polymer (Parylene C). [16]

The typical etch rates of Si 6" wafer for surface micromachining applications are 2 to 3 µm.min^{-1}. For small chips up to 10 µm.min^{-1} and fully exposed 6" wafer etches at 0.2 µm.min^{-1} rate.

Completely resistant to XeF_2 etch are some metals (Al, Ni, Cr, Pt, Ga), compounds (PZT, MgO, ZnO, AlN, GaAs), polymers and organics (PR, PDMS, C_4F_8, silica glass, PVC, PP, …etc.). [17]

Etching can occur during two types of processes:

1. pulsed flow – higher efficiency and accurate mixing of XeF_2 with other gases,
2. continuous flow – easier to achieve high uniformity, more distinct control of the etch depth and easier end point detection (reaching the desired etch magnitude). [17]

Table 2-1: Etch selectivity of some materials to silicon in XeF_2 vapor-etching. [17]

Material	Mo	Ge	SiGe	SiO_2	Si_3N_4	Au	Cu
Selectivity to Si	2:1	(*)	(*)	1000:1	>1000:1	(+)	(+)
Material	**SiC**	**Ti**	**TiN**	**Ta**	**TaN**	**W**	**TiW**
Selectivity to Si	(+)	(*X*)	(*X*)	(*X*)	(*X*)	(*X*)	(*X*)

(*) - same or greater than Si; (+) – low amount of attack under certain conditions;
(*X*) – etch rate (0 to 300 Å.min^{-1}) depends on temperature

2.3 Parylene vapor deposition polymerization

Parylene is the trade name for compounds known as poly-para-xylylenes. Their resulting polymer species are formed in a process of pyrolysis in vacuum, which is best imagined as direct condensation from gaseous phase onto the substrate. During the deposition cycle, the gas vapours don't pass through intermediate liquid phase, so the thickness is very uniform over all deposited surfaces. There are three primary variations of Parylene: C, N and D. [18]

- **Parylene N** is the basic compound of poly-P-xylylene, it is completely linear and a highly crystalline material. Its molecules are extremely elastic, which causes them to "bounce" over the surface several times before depositing. That renders this species capable of penetrating small openings in the substrate better than other variants. The deposition pressure during heating and deposition time are higher than in Parylene C or D.
- **Parylene C** is commercially more available and it's the same monomeric compound, but with substituted aromatic hydrogens with chlorine atom. This type is most popular due to high dielectric strength, cost and process advantages, such as higher deposition rate and good pressure control.
- **Parylene D** is also commercially available and from original monomeric structure it has two hydrogen atoms substituted by chlorine. It's not very elastic, so the polymer will deposit shortly after entering the deposition chamber. The pressure rise during the deposition process is quite low. [18]

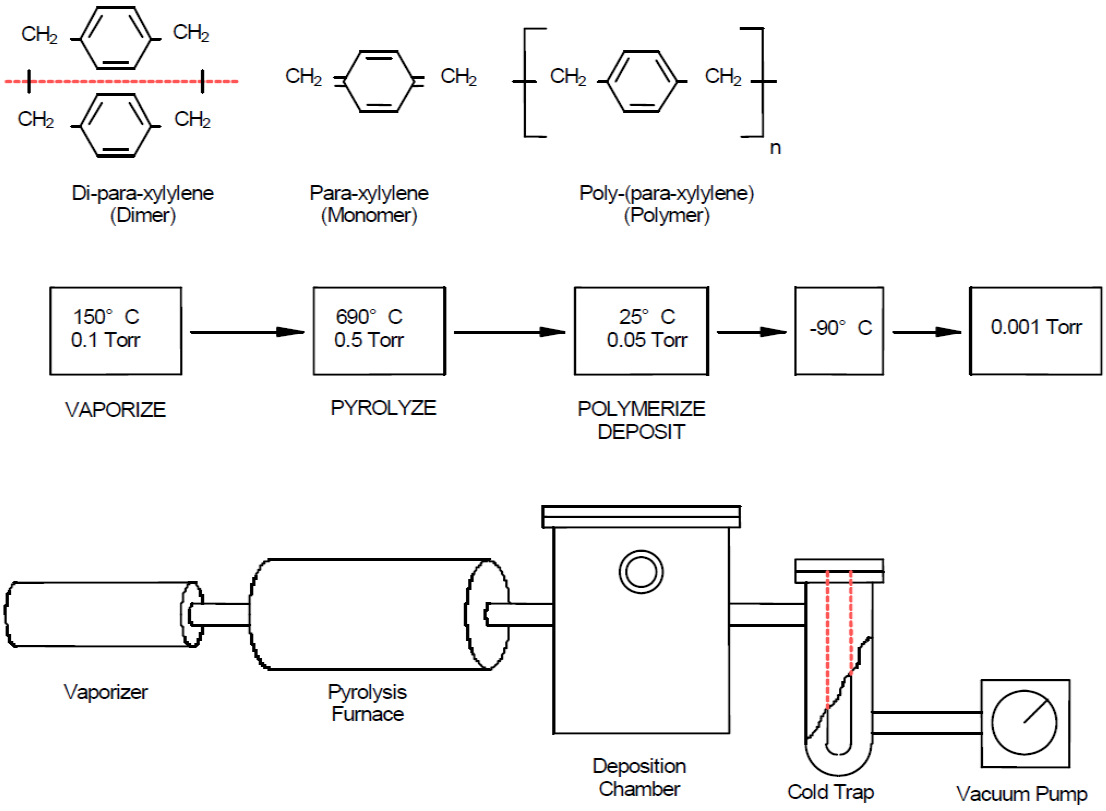

Fig. 2-6 Typical deposition system block diagram of main process components. [18]

The polymerization process occurs at pressures around 1,5 Pa and the polymers are formed at room temperatures. As seen on fig. 2-6, the process starts in a vaporizer tube, where the Parylene is vaporized from its solid dimer form and sublimates into gaseous phase. The gases travel through a furnace where high temperatures pyrolysis happens (breaking of dimer into monomer form). When the deposition chamber is at room temperature, the monomers polymerize uniformly on every surface inside the vacuum chamber. The cold trap stops the gases from entering the vacuum pump.

2.3.1 Bonding with Parylene

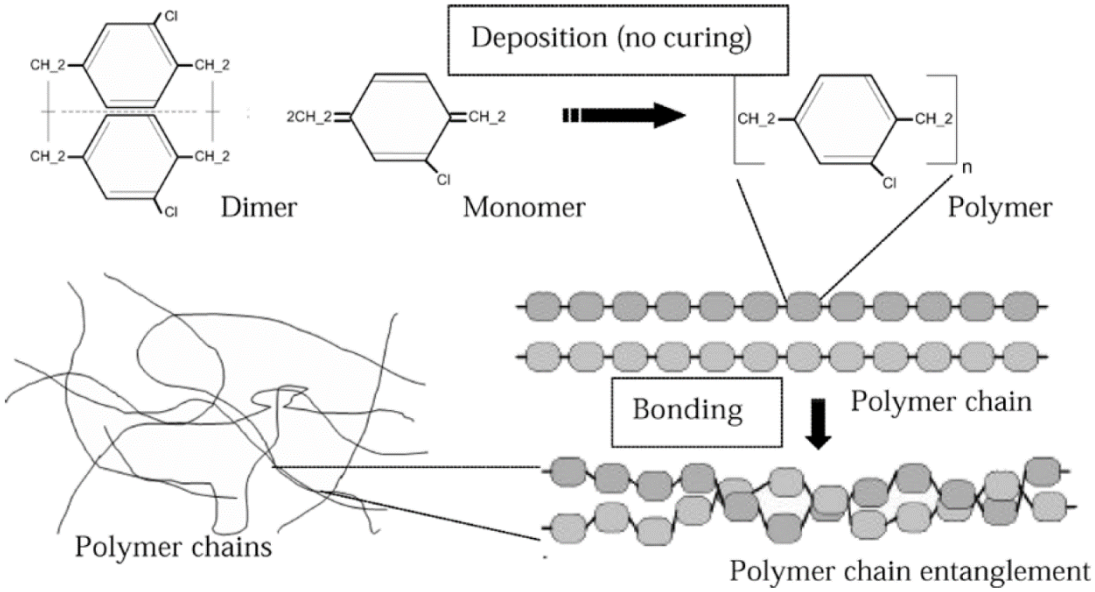

Fig. 2-7 Hypothetical Parylene chain entanglements. [19]

Some applications, mostly three-dimensional MEMS devices, sometimes require stacking wafers and bonding them together. Microfluidic chips, which have utilized Parylene polymers for micro-channel fabrication, also might require fluid-proof sealed cavities. Bonding techniques are generally performed under low or elevated temperatures. For those applications, where polymers are used, the high temperature bonding (eutectic, anodic and fusion bonding techniques) is out of the question, because polymer structures usually melt, soften or burn at or above 300°C. Bonding at low temperatures uses adhesive polymer materials, or solders, which are carried out at temperatures below 300°C. [19]

A Parylene film, when heated, does not undergo any chemical reactions, except for the glass transition temperature at 109 °C and the melting temperature at 303 °C. In this temperature range, a physical entanglement of Parylene film polymeric chains might occur, thus, making Parylene bondable to itself. [19]

2.4 Adhesion promotion of polymeric and silicon surfaces

In many fields, there is a need for connecting two materials of same, but often very different properties. In metals, and other amorphous materials, welding and soldering, or generally using high temperatures, can give a desired result. In plastics, low temperatures are more suitable, but even better are creating connections at temperatures below 50 °C, which does not cause so much degradation, that is very common in many polymeric materials. That may involve options, such as ultrasound soldering or using a excited gas – plasma. Plasma treatment can create chemically functional groups and radicals, which activates the surface. [20] This may allow connecting two same or different materials, like metals and plastics using chemical bonds. Another option is silanization of incompatible material surfaces for covalent binding. [21]

2.4.1 Surface activation by O_2 plasma

One method of plasma surface activation is with a noble gas, for example argon (Ar). When the Ar is ionized in an electric field, it stops being electrically neutral and tries to return to the neutral state by catching an electron. If it hits the surface of the treated material, it reacts with high energy, that is strong enough to remove an electron and leave an open bond on the surface or crack the bond of a polymer (see fig. 2-8a). The downside of using Ar is, that the naked bonds recombine too quickly. [20]

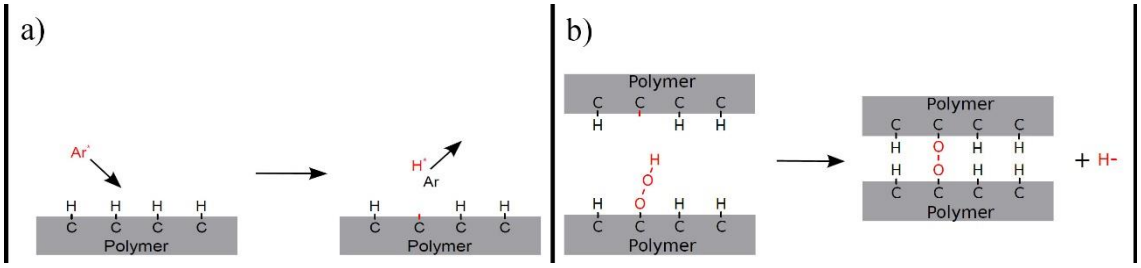

Fig. 2-8 (a) Effects of argon ion on polymer; (b) Theoretical reaction of two oxygen activated polymer surfaces. [20]

Using a reactive gas, such as oxygen (O_2), the surface can be activated by creating functional hydroxyl groups (OH groups). These groups are able to react with another chemical groups of the second material and create covalent bonds. But the resulting O-O (peroxide) bond shown in fig. 2-8b is not permanent, and an adhesion promoter is therefore needed as an intermediate layer. Such molecule can create a permanent connection between these two materials. The adhesion promoter can be applied directly by plasma and then the elastomers are melded together or, as shown on fig. 2-9, the surface activated by plasma is applied with the promoter and melded with the other polymer with an amino group, that can react with hydroxyl group of the adhesion promoter. This example shows, that the chemistry of both materials has to be known. [20]

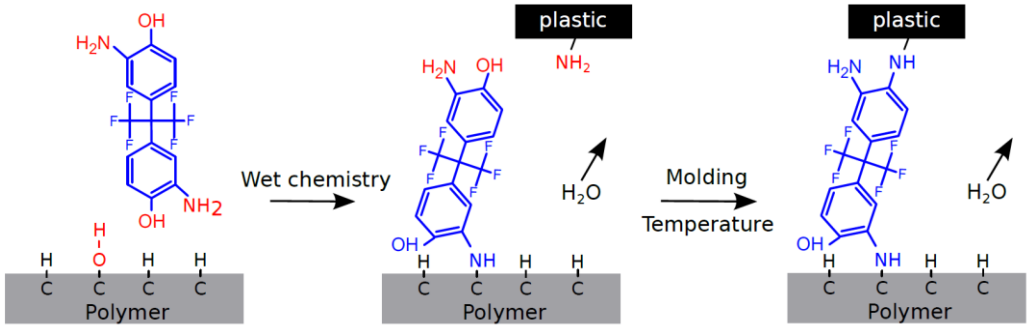

Fig. 2-9 Example of an adhesion promoter creating a connection between two polymers (one surface is plasma-activated). [20]

2.4.2 Silane adhesion promoters

As stated in previous chapter, two dissimilar materials can adhere to each other with an adhesion promoter, or a coupling agent, that is put between them. It will act at the organic-inorganic interface to chemically and physically connect them with a strong cohesive bond. In some cases, plasma enhancement is required before applying the coupling agent.

These promoters are chemical materials that contain dual functionality in their molecular structure. Its inorganic reactivity is given to by a metallic central atom (e.g. Si, Zr, Ti, Al…), especially if methoxy, ethoxy or hydroxyl groups are attached to the metal atom. As for organic reactivity of the adhesion promoter, an organofunctional group can be attached to the metal through an alkylene, arylene, or other type of organic bridge. [22]

A silicon-based chemical, that acts as a coupling agent, has a general structure of four substituents attached to a single silicon atom. The most common structure has three inorganic – reactive alkoxy groups, methoxy or ethoxy, and one organic group (sometimes it may have one of the alkoxy groups replaced by a methyl group). These coupling agents will act in the area between an inorganic and an organic substrate and create a bond or a bridge to improve adhesion between the two dissimilar materials (see fig. 2-10). [22]

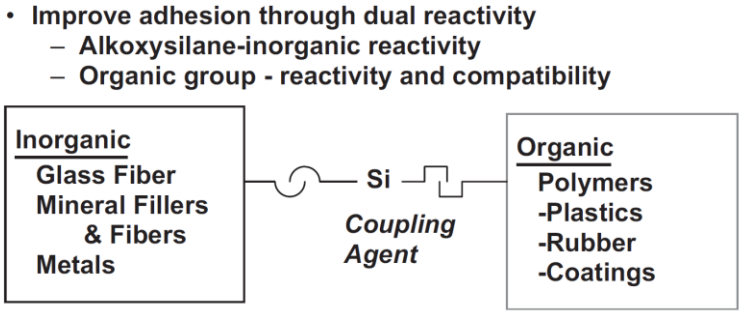

Fig. 2-10 Dual reactivity of a silane-coupling agents. [22]

2.5 Atomic layer deposition ALD

ALD is a vapor phase technique capable of producing thin films of variety of materials. It had demonstrated potential advantages over alternative deposition methods, such as chemical vapor deposition (CVD) and various physical vapor depositions (PVD) techniques, due to its conformality and control over materials thickness and composition.

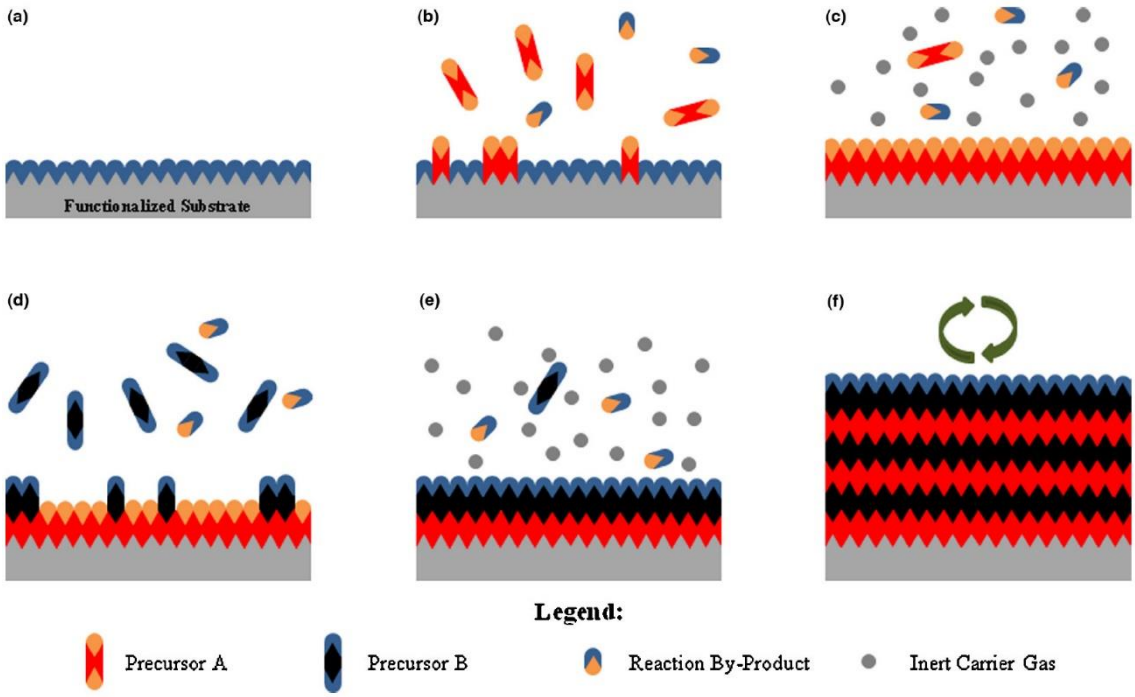

Fig. 2-11 Schematic of ALD process: (a) Substrate with natural or treated functionalization. (b) Pulse of precursor A and his reaction. (c) Purge of excess products by inert carrier gas. (d) Precursor B is pulsed and reacts. (e) Another purge by inert gas. (f) Previous steps are repeated until desired thickness is achieved. [23]

The process itself consists of sequentially alternating pulses of chemical precursors, which react with the surface (see fig. 2-11). One pulse of reactive precursor, called half-reaction, leaves no more than one monolayer at the surface. The half-reaction leaves some unreacted precursors and by-products which are purged with an inert carrier gas (typically it's N_2 or Ar). This is then followed by a counter-reactant precursor pulse and purge. That leaves a layer of the desired material and the surface is prepared for another cycles of precursor pulses and purges until the appropriate film thickness is achieved. Since those created monolayers are basically molecules, the growth of the film is usually less than 1 Å per cycle, depending on the individual process. Usually, the Ald processes are conducted at modest temperatures (<350 °C) and there is a temperature range called "ALD temperature window" which varies between processes. Temperatures outside this window will result in poor growth rates and quality. One of the desired qualities of ALD is its high conformality and aspect ratio. That is achieved by its self-limiting characteristic of growing only one layer at a time. Another quality derived from this is high thickness control. With this technique, one is able to grow very thin and conformal coatings of a wide variety of materials. [23]

2.6 Surface and structural characterization

The Gecko setae and their spatulas, due to their size, fall into the category of nanostructures (size <1 μm). For that reason, more advanced methods and equipment are required for characterising physical or surface properties of Gecko nanostructures. In this work, two methods are discussed, SEM (Scanning Electron Microscopy) and AFM.

2.6.1 Scanning Electron Microscopy (SEM)

This technique is one of the most widely used in characterization of nanomaterials and nanostructures. The resolution of such microscope is in a few nanometres and can operate at magnifications from ~10x to over 300 000x. [10] The construction of a scanning electron microscope is shown on fig. 2-12a.

The source of electrons could be represented by a thermal cathode (usually tungsten filament) and the electrons are emitted thermionically. For field emission guns (FEG), which are of a cold-cathode type (using tungsten single crystal) or thermally assisted Schottky type.

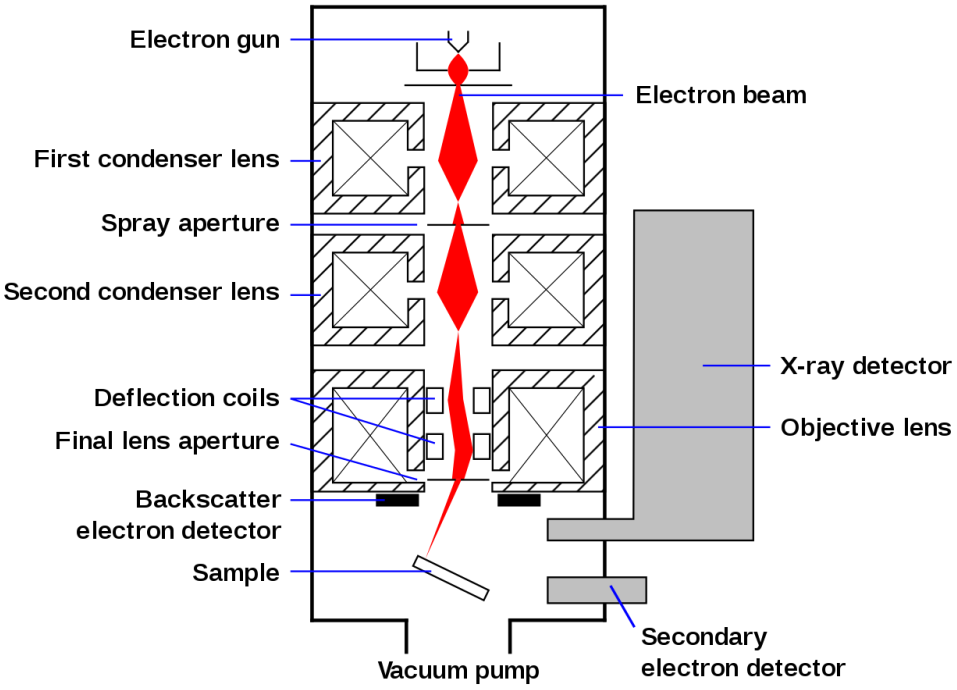

Fig. 2-12 Schematic of an SEM. [24]

This source of electrons is focused into a beam, with a spot size of ~5 nm (or less in modern SEMs) and has energy ranging from 100 eV to 50 KeV. Through the column, it is rastered with deflection coils over the sample surface and as the electrons hit the surface and penetrate it, a number of electron-sample interactions occur (fig. 2-12b). Three types of products of these interactions are typically utilised and detected in SEM imaging: secondary electrons (SE), backscattered electrons (BSE), and characteristic X-rays. An SE is formed, when a beam electron undergoes inelastic collision with an atomic electron to which the primary electron transfers part of its energy. The secondary electron

is then emitted from the sample. BSE were elastically scattered and essentially possess the same energy as the primary electrons. The probability of BSE increases with the atomic number of the sample material, so while they can hardly be used for topology imaging, they can develop a useful contrast between two materials of different atomic number. The primary electron can excite a core electron from the surface atoms, and the excited electron can emit a characteristic X-ray photon (Auger electron) while returning to its ground energy state, which can be used for chemical characterization. [10]

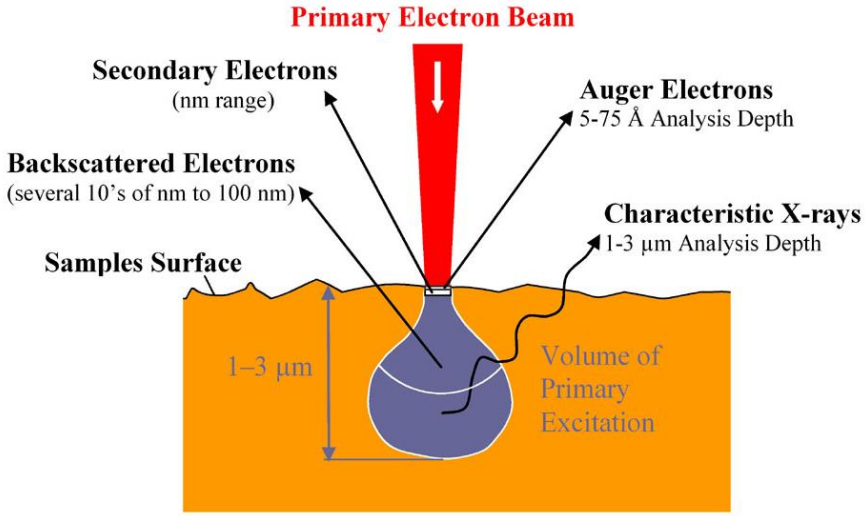

Fig. 2-13 Electron-sample interactions at the surface of the scanned sample and areas of their product's formations.[25]

The resolve power or resolution R of SEM instruments is determined by the wavelengths of the electron beam λ and the numerical aperture NA of the system:

$$R = \frac{\lambda}{2 \cdot NA} \tag{5}$$

where the numerical aperture NA is represented by each objective and condenser lens system.[10]

2.6.2 Atomic force microscopy (AFM)

On contrary of the SEM imaging, the scanning probe microscopy (SPM) offers the possibility to manipulate molecules or nanostructures on the sample surface and measure probe-to-sample interactions. Although there is some level of hybridization in SEM equipment, where a simple probe can be controlled above the sample for nanomanipulation (piezo mounted tips). SPM consists of many different techniques of sample-probe interaction but is represented by two major members scanning tunnelling microscopy (STM) and atomic force microscopy (AFM). [26]

By modifying the STM, Binning, Quate, and Gerber developed the AFM in 1986 as a collaboration between IBM and Stanford university. Unlike STM, the AFM can be used to study insulators, as well as semiconductors and conductors. The probe used is a sharp tip less than 5 µm tall and 10 µm in diameter at the base. This tip is located at the end of a cantilever beam that is usually 100-500 µm long. Some examples of tips can be found in fig. 2-14. [26]

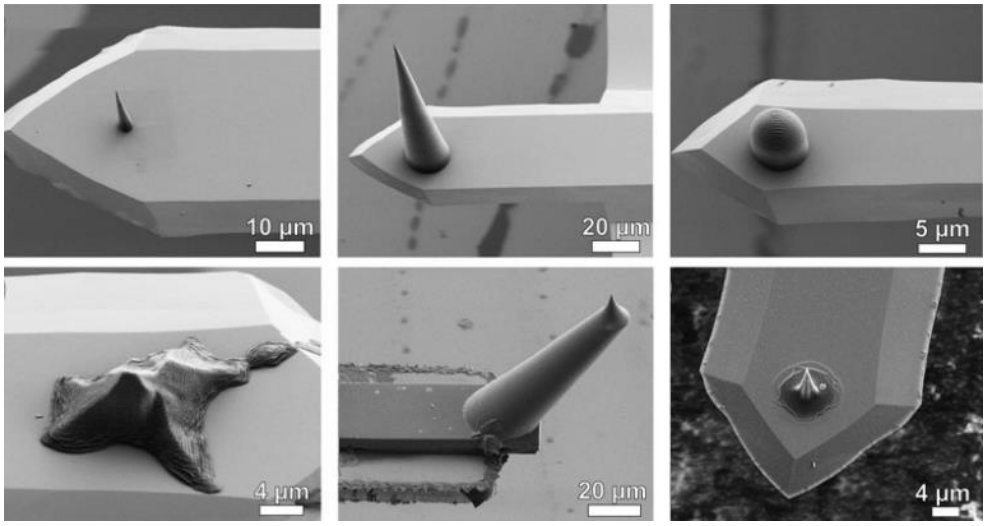

Fig. 2-14 Examples of tips of different shapes and sizes mounted at the end of a cantilever. [27]

The AFM obviously measures the tip-sample interactions and of various types. At short distances, the van der Waals interactions are predominant. They were discussed in chapter 1.3.1. In addition to van der Waals forces, some long-range forces may act and become significant at longer distances, where the weak van der Waals forces don't work. Such forces include electrostatic attraction/repulsion, current induced or static-magnetic interactions, and capillary forces (caused by water condensation on the tip and sample). [10, 26]

During measurement, the cantilever beam bends according to the interactions of the surface and the force, that causes that motion can be as small as 10^{-18} N. [28] The detection of this beam deflection is measured by a laser diode (fig. 2-16), which light is reflected from the surface at the cantilever end and an adjustable mirror onto a photodiode, that senses the small laser beam deviations (distances of 10^{-4} Å).

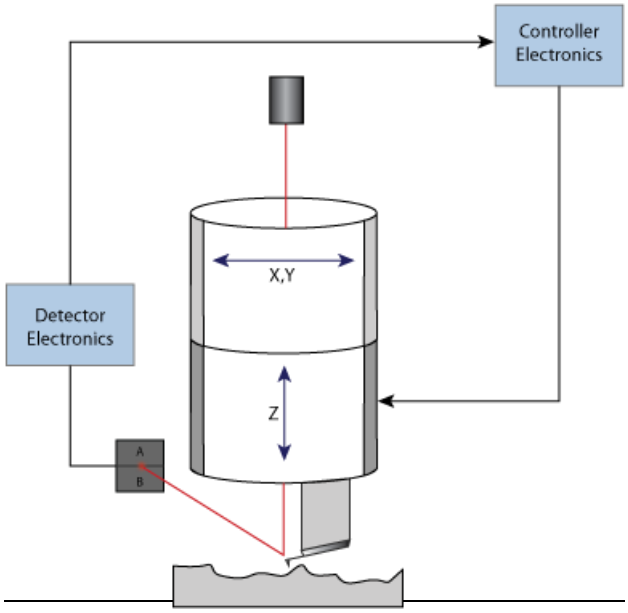

Fig. 2-15 Feedback loop control with a piezoelectric in an AFM system for maintaining constant cantilever deflection or oscillation amplitude. [28]

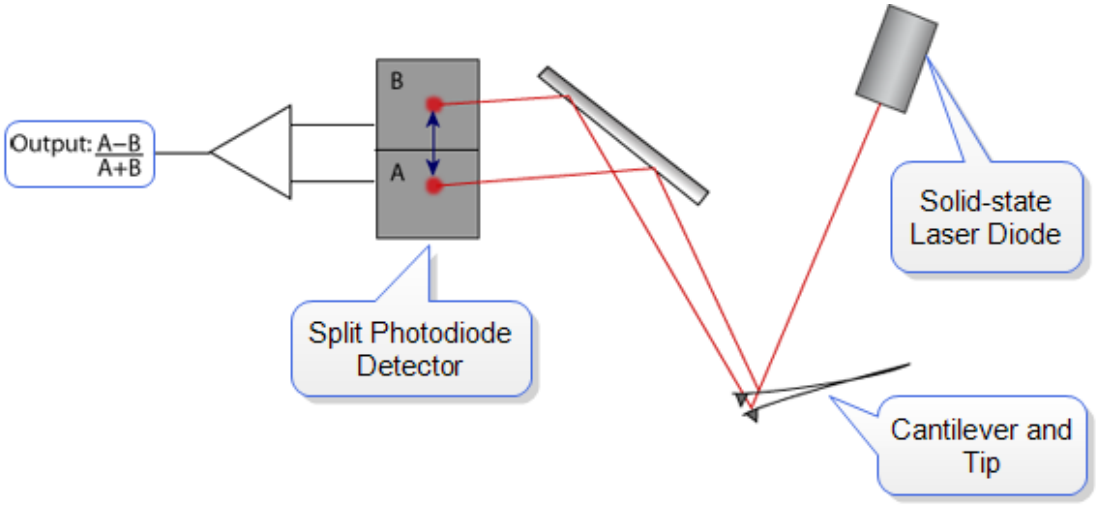

Fig. 2-16 The schematic of a cantilever beam deflection detection by a photodiode. [28]

There are 3 primary modes of AFM:

1) **Contact mode** where the tip is in perpetual contact with the sample. The probe gently scans the topology of the surface and the feedback loop maintains a constant cantilever deflection so the force between the tip and the sample remains constant. To maintain a "setpoint" deflection, the piezo scanner moves vertically to compensate for the tip deflection caused by surface roughness.

   This force is calculated from Hooke's Law [26, 28]:

$$F = -k \cdot x, \tag{6}$$

   where F is the deflection force, k is the spring constant (in contact mode, the spring constant is lower than the effective spring constant of the force holding atoms of a solid together) and x is the cantilever defection.
   Data collected by the computer are the vertical distances of the scanner, for each (x, y) data point. [28]

   Advantages: high scan speeds; "Atomic resolution" images; "Rough samples with extreme changes in vertical topography can be scanned more easily. [28]

   Disadvantages: lateral (shear) forces can distort features in the image; Forces normal to the tip-sample interaction can be high in air due to capillary forces from the adsorbed fluid layer on the sample surface; Combination of lateral forces and high normal forces can result in reduced spatial resolution and may damage soft samples (i.e., biological samples, polymers, silicon) due to scraping between the tip and sample. [28]

2) **Non-contact mode** is one of several vibrating cantilever techniques in which an AFM cantilever is vibrated near the surface of a sample. The spacing is generally on the order of tens to hundreds of Angstroms. The inter-atomic force between the cantilever and sample in this regime is attractive (largely a result of van der Waals interactions). [28]

   Advantage: no force exerted on the sample surface. [28]

Disadvantages: lower lateral resolution; Slower scan speed than Tapping Mode and Contact Mode to avoid contacting the adsorbed fluid layer; Usually only works on extremely hydrophobic samples, where the adsorbed fluid layer is at a minimum. [28]

3) **Tapping Mode**™, the most commonly used of all AFM modes, is a patented technique (Bruker) that maps topography by lightly tapping the surface with an oscillating probe tip. The cantilever's oscillation amplitude changes with sample surface topography. [28]

   In general, Tapping Mode is much more effective than non-contact AFM, but especially for imaging larger areas on the sample that may include greater variation in topography. [28]

   Advantages: higher lateral resolution on most samples (1 nm to 5 nm); Lower forces and less damage to soft samples imaged in air; Lateral forces are virtually eliminated, so there is no scraping. [28]

   Disadvantage: Slightly slower scan speed than Contact Mode AFM. [28]

2.6.3 Force-Distance Curves

A good way to measure the force between a cantilever tip and a surface are Force-distance curves, that measures the cantilever deflection while it is approaching the sample surface. The deflection is directly proportional to the tip-sample force. The force distance curves contain the following useful information:

- The sensitivity of the detection method can be determined;
- Properties like the sample elasticity or the maximum tip-sample adhesion force can be accessed;
- The working point (setpoint for the cantilever deflection signal) for subsequent AFM imaging can be characterized and chosen properly. For instance, when imaging is performed in the attractive force regime it can be determined how far the working point is located from the point of snap-to-contact.
- A force-distance curve can be used to determine the tip-sample force-distance dependence, at least partly.[26]

The aim is to obtain the tip-sample force $F_{ts}(d)$ as a function of the tip-sample distance d, as indicated in fig. 2-17. What is actually measured when acquiring a force-distance curve is the deflection of the cantilever z_{tip} (which is proportional to the tip-sample force) as function of the z-position of the sample z_{sample}.

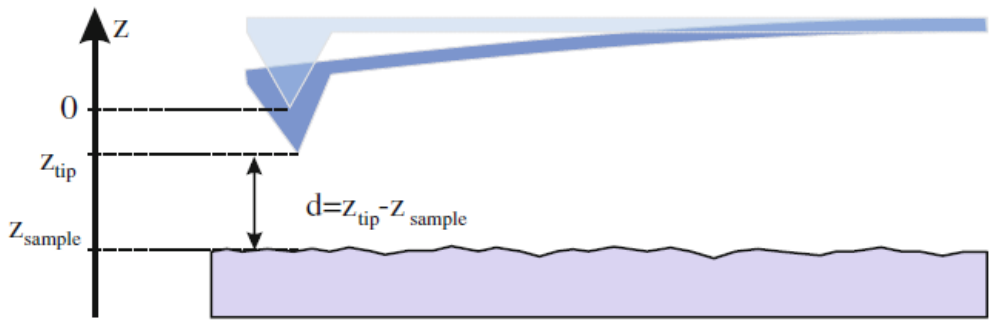

Fig. 2-17 Denotation for the coordinates used in force-distance plots. [26]

An example of a force-distance measuring plot is shown on fig. 2-18 where the *blue curve* corresponds to an approach (extension) of the tip toward the sample, while the *red curve* corresponds to a retraction of the tip. At points *c* and *f* the force gradient becomes equal to the spring constant of the cantilever and when the force value further increases, the plot jumps to point *d* (snap-to-contact). The maximal cantilever deflection at point *c* multiplied by the spring constant gives the maximum attractive force before snap-to-contact (usually quite small). [26]

At $z_{tip} = 0$ the cantilever is unbent, because the tip-sample interactions compensate each other. When the tip pushes further into the surface, the tip moves with the surface and the slope of the repulsive force rises very sharply upwards. Specifically for a stiff sample with a high elastic modulus, the $z_{tip}(z_{sample})$ curve is a straight line with a slope of one. If the sample is soft, the slope can be (initially) smaller than one (due to an indentation of the tip into the sample), resulting in information about the elastic/plastic deformation of the sample. [26]

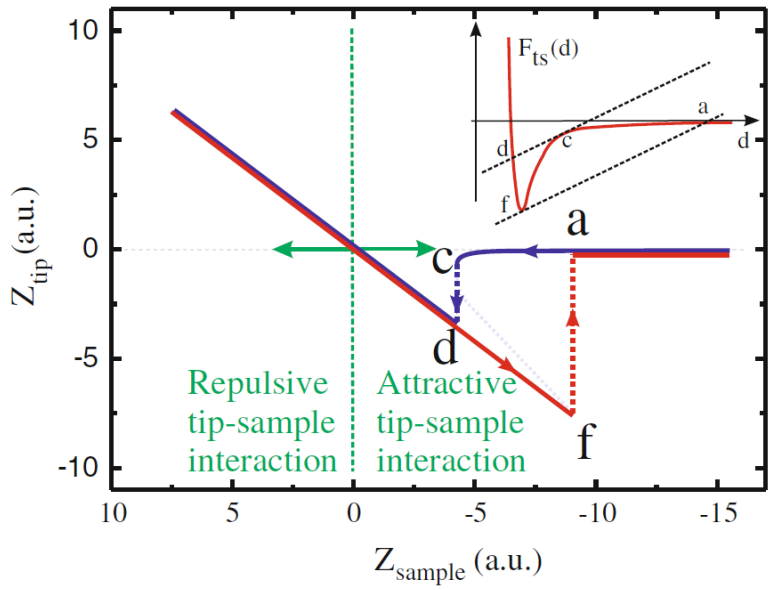

Fig. 2-18 A force measuring plot where the horizontal axis describes movement of the tip towards the sample and the vertical axis is the deflection of the tip caused by attractive and repulsive forces. [26]

If the direction of the sample motion is reversed, the tip motion follows the same straight line in the reverse direction (red line) for stiff samples. The repulsive tip-sample force decreases continuously and finally the attractive regime is entered again, where tip and sample adhere to each other as long as the tip-sample force gradient is smaller than the cantilever spring constant. If the force gradient becomes larger than the cantilever spring constant, the cantilever snaps out of contact (point *f*). The tip snaps back to a position where the deflection of the cantilever is close to zero (point *a*). Point *f* corresponds to the position at which the maximum attractive force (adhesion force) between tip and sample acts. [26]

2.6.4 Wetting properties of materials and their measurement

The wettability of a surface material is influenced by its surface chemistry. That means, that the interactions with water molecules depends on how well the material surface corresponds to the polar nature of a specific liquid. Based on the interactions of water droplets on a solid surface, the surface can be categorized as hydrophilic, hydrophobic or superhydrophobic. A hydrophilic surface shows strong affinity towards water and the water contact angle is < 90°, whereas a hydrophobic surface strongly repels the water at a contact angle > 90° and water tends to "bead" on the surface. Fig. 2-19 doesn't show a superhydrophobic contact, when the contact angle is > 150° [29, 30]

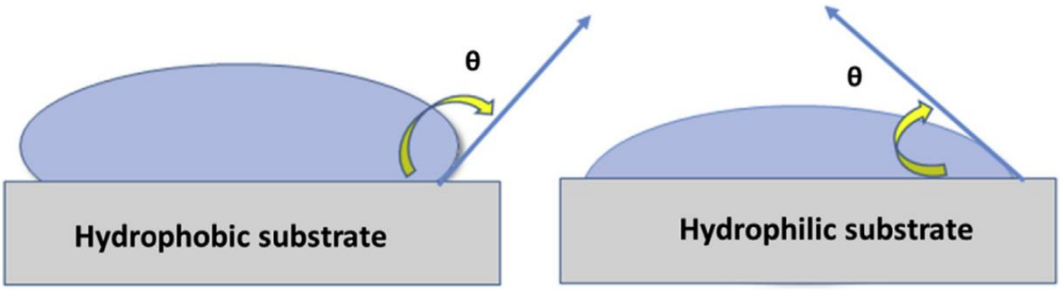

Fig. 2-19 Schematic look of interaction of water molecules with different substrate. [29]

The contact angle is an effective method to understand surface interaction with three phase system (solid/liquid/air). When a drop of water is added onto a surface, the intersection of these three phases appears in one point (fig. 2-20). The contact angle depends mainly on the steady forces at this boundary. It is the significant measure of surface wetting behaviour; it is expected to be the characteristic property of given surface in the particular environment and was first discussed by Thomas Young. The contact angle on an ideal flat surface is described by the Young's equation [29, 31]:

$$\cos\theta_{\mathrm{Y}} = \frac{\gamma_{\mathrm{SG}} - \gamma_{\mathrm{SL}}}{\gamma_{\mathrm{LG}}} \tag{7}$$

where θ_{Y} represents Young's contact angle, γ_{LG}, γ_{SG} and γ_{SL} symbolize the liquid-vapor, solid-vapor and solid-liquid interfacial tensions, respectively. Young's equation is derived from the hypothesis that the surface is an ideal surface – rigid, flat, nonreactive, inert, homogenous, insoluble, smooth, and nonporous. [29]

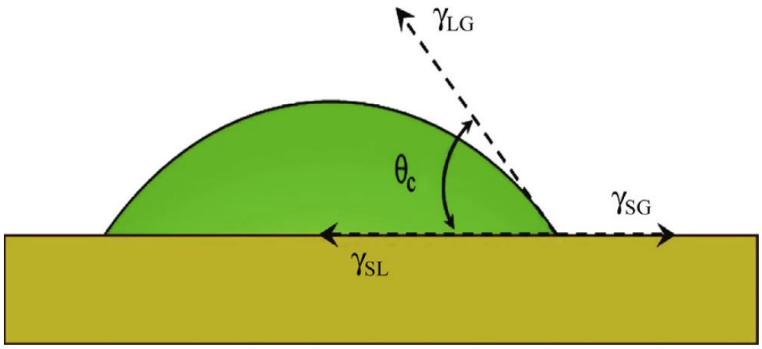

Fig. 2-20 Contact angle formed when the liquid spreads over the surface. [29]

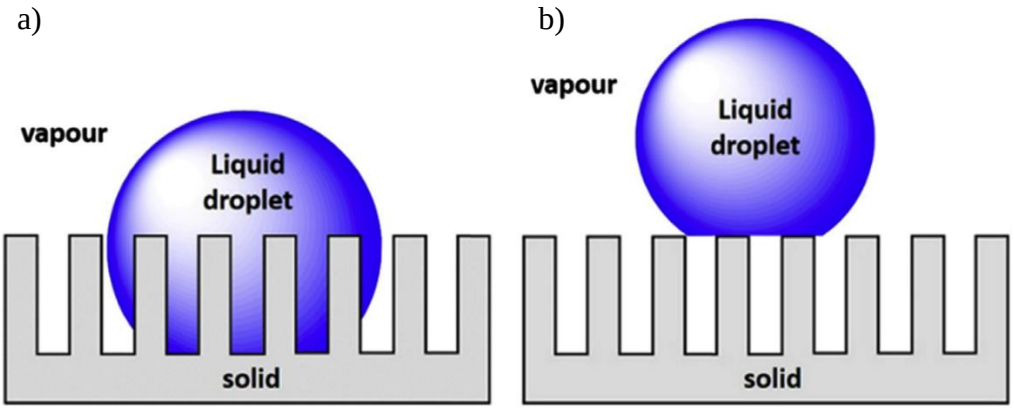

Fig. 2-21 A schematic showing the behaviour of a water droplet on a rough surface in (a) Wenzel's and(b) Cassie's state. [29]

For a rough surface, the contact angle can be described by Wenzel's model or Cassie-Baxter's model (see fig. 2-21). In the Wenzel model, the droplet was assumed to permeate into the rough surface and to contact the rough surface thoroughly. The contact angle on the rough surface (θ_W) can be estimated by Wenzel equation [29, 31]:

$$\cos\theta_W = R_f \cos\theta_Y \tag{8}$$

where the roughness factor (R_f) is defined as the ratio of the actual to the apparent surface area and, hence, is larger than unity. The topological features of the surfaces are presumed to be insignificant related to the drop dimensions. Also, their geometry is irrelevant as long as it does not affect the surface area. [29]

On the other hand, the Cassie-Baxter model assumes the droplet in contact with solid with air trapped in the interface. The Cassie equation was depicting derived contact angle changes for two components [29]:

$$\cos\theta_C = f_1 \cos\theta_1 + f_2 \cos\theta_2 \tag{9}$$

where θ_C is the Cassie contact angle, f_1 is the fractional surface area with contact angle θ_1,

and f_2 is the fractional surface area with contact angle θ_2. The Cassie-Baxter equation is a simplified equation (9) for a porous surface ($\theta_2 = 180°$) and it was given as[29]:

$$\cos\theta_C = f_1 \cos\theta_1 - f_2 \tag{10}$$

Primarily, the Cassie-Baxter equation was derived to determine the wetting characteristic of porous substrate and it is applicable to a hydrophobic rough surface when liquid molecules do not penetrate into the surface structure. One of the advantages of Cassie-Baxter approach over Wenzel's model is that it pronounces the real systems analysis more precisely [32], but it fails to accurately determine the parameters f_1 and f_2 for randomly rough surfaces.

Contact angle measurement – Sessile drop technique

This method is one of the most extensively employed for directly analysing the tangent angle at the three-phase equilibrium interfacial point. Contact angle for flat surfaces is determined by direct measurement of contact angle by viewing the drop profile. On fig. 2-22 it is shown, that an image of an adhering liquid drop can be projected onto a screen and the outlines traced, there after the angle is measured. [29]

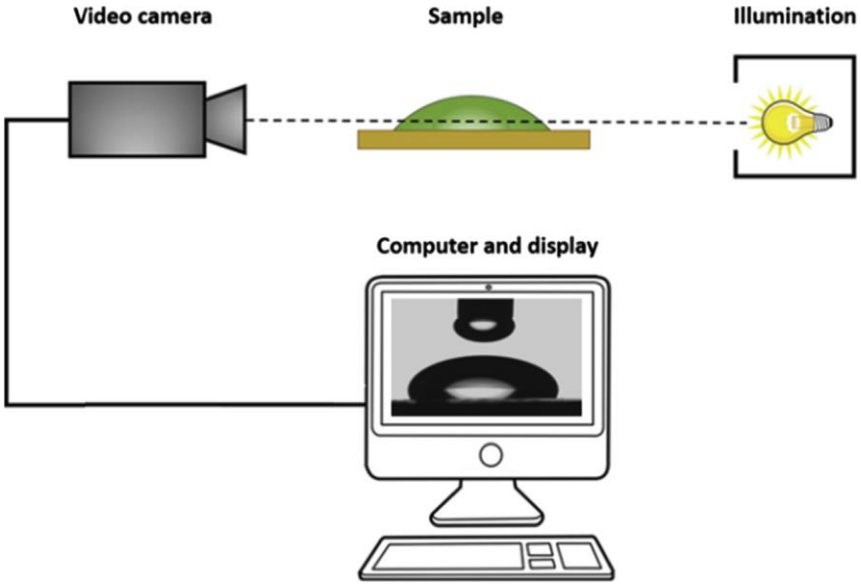

Fig. 2-22 A schematic of an analyser for the sessile drop technique. [29]

This method has the advantage of simplicity in operation and only small surface area of substrates and small amounts of liquid are required. On the other hand, there is a comparatively higher influence of impurities due to the small size of the substrate and liquid. The reproducibility and accuracy of contact angle measurement mainly depend on the assignment of the tangent line and consistency of the operator. [29]

Some guidelines for practical application of this technique:

- the telescope/camera should be tilted down slightly (1-2 degrees) off the horizon so that the surface-liquid phase is not out of the line of sight and a part of the reflection of the formed drop is observed;
- starting the growth of drop, it should have a diameter of about 5 mm and the needle should have the smallest diameter possible, to not distort the drop profile shape;
- measuring both sides of the liquid drop and using averaged angles is advisable. [29]

Drawbacks of this method are an environmental effect on the measuring surface (e.g. humidity) and lower contact angles (below 20°) add an uncertainty value to accuracy of measurement, because the droplet profile is almost flat. Also, the surface roughness and dust may cause deviations in the contact point along the three-phase contact line. Furthermore, the dependency of the contact angle on the drop profile also causes a systematic problem. Despite all these constraints, the sessile drop technique is deliberated to be the most effective method. [29]

3 DESIGN AND FABRICATION OF GECKO BIOMIMETICS

The term “biomimetics” (from Greek word *biomimesis)* refers to artificial designs or derivations inspired by objects found in nature. From understanding the basic principles of how these natural “tools” work at the nanoscale, at least, one can try to recreate nanostructures, nanomaterials and processes with desired functionality, in other words, mimicking biology of creatures or plants in nature. [2, 33]

Considering this in creating a gecko inspired design, it’s important to state what is the desired functionality of final structures. The aim of this work is to create a surface on which mechanical forces will be measured and analysed and additionally modified to enhance its capabilities.

3.1 Topology

It is technologically not feasible (practically impossible), with available tools, to recreate the same fine fibrillar structures as on the gecko setae. But for the purposes of this work a simple array of small polymeric pillars, with distances comparable to their size, are sufficient. The adhesive forces can be then measured on a larger set or on an individual pillar. The topology of such array has been created in CNST Nanolithography Toolbox, which is shown in fig. 3-1 and fig. 3-2 below.

The design created is made of 4x4 mm square array of dots with a diameter of 1 μm and with a 4 μm pitch (spacing) drawn in a hexagonal pattern (see fig. 3-1 and fig. 3-2d). The topology is sized for a 10 cm (4 inch) wafer piece. Therefore, the squares are distributed orthogonally with a spacing of 1 mm, so that most of the effective surface of the wafer is covered (fig. 3-2a). The total amount of dots per square is around 1 150 000.

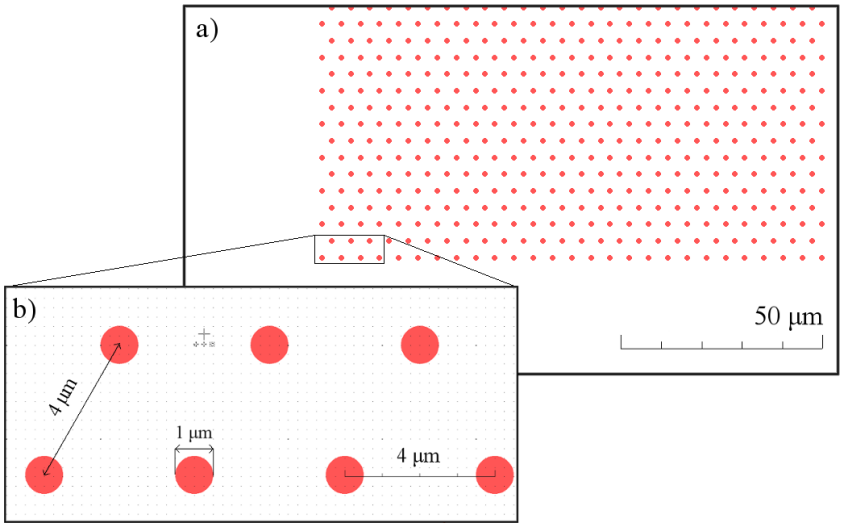

Fig. 3-1 (a) Design dots representing top-view of individual Gecko pillars and (b) details of arrangement and dimensions of the dots

Around the squares are additional comb-shaped and L-shaped check markings of different sizes (e.g. 1 µm check mark in fig. 3-2e) to inspect deviations of dimensions from different fabrication steps. For similar reasons, four 4x4 mm windows were added to the design instead of dots, so they can also be used for reference purposes later in the fabrication process (red squares in fig. 3-2).

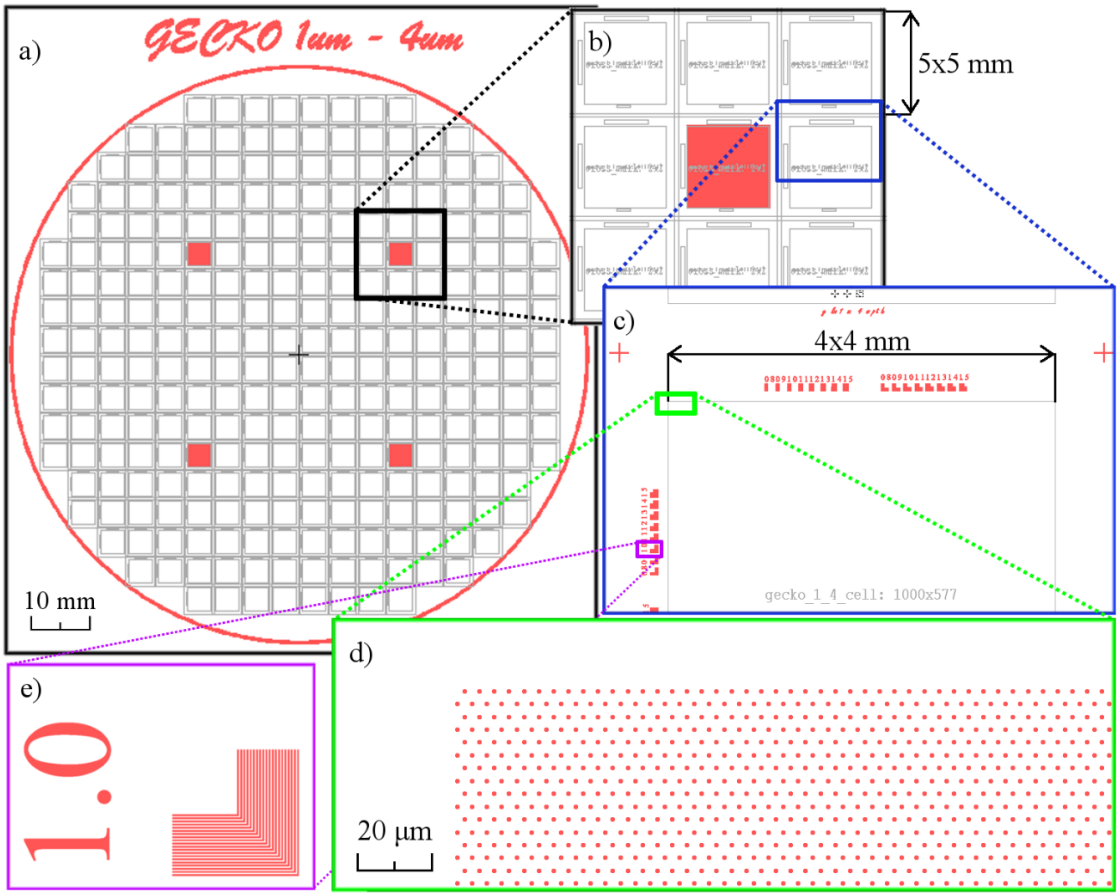

Fig. 3-2 (a) Levels of topology fitted for a 4 inch wafer; (b) detail on the copies of squares with one of the reference windows (red square); (c) dimensions of a single square with (d) the array of dots; purple rectangle shows (e) an example of an L-shaped 11 µm sized check mark.

The layout presented is only one version of many variations, including larger (up to 2 µm) and smaller dots (0,5 µm) and different pitch. The level of spacing will probably have effect on the adhesive behaviour of the final Parylene C structures. Mostly, the finer layout will be used, that is 0,5 µm dots with 1 µm pitch for the creation of the pillars, and 0,5 µm dots with a pitch of 2 µm and higher for adding “bubbles” on top of the pillars. The preparation of structures with “bubbles”, and their function, will be discussed in the following chapters.

3.2 Photolithography of Gecko wafers

A 380 μm thick, one-side polished, silicon (Si) P-type wafer and with a 200 nm layer of PECVD grown silicon dioxide (SiO_2) was chosen as the substrate for next fabrication steps. The requirement of SiO_2 layer will be explained in following chapters. The photolithography and development were carried using Resist coating and development system SÜSS MicroTec RCD8 and the Mask Aligner, Nanoimprint Lithography SÜSS MicroTec MA8/BA8 Gen3.

The RCD8 coat and develop platform provides an option to semi-automatically coat resists with a GYRSET® enhanced coater and after reconfiguration it works as a puddle & spray developer tool. It can handle small pieces as well as standard wafers up to 200 mm and serves therefore ideally for daily R&D work up to small scale production.

MA8/BA8 Mask aligner is great for resist film preparation for fabrication of nano- and microstructures. It houses a mercury arc lamp with a light source of a wavelength from the UV spectrum (193 – 405 nm) to expose thick and thin photoresist films.

Fig. 3-3 Finished negative glass mask carrier after DWL lithography with 1 μm sized dots with 4 μm pitch.

For Gecko lithography a glass mask was chosen, with one side coated with a thin layer of chromium covered with a photo-resistive polymeric film. Using UV Direct Write Laser (Heidelberg Instruments DWL 66-fs) lithography system the PR film was exposed, and the uncovered metal further etched. The photo of this mask is on fig. 3-3.

Using the previously prepared mask carrier the whole photolithography procedure follows these steps:

1. Cleaning the wafers using oxygen plasma in Resist stripper Diener Plasma cleaner from any surface contamination.
2. HMDS – coating a monolayer adhesion promoter for the PR. The reason is the layer of SiO_2 which is hydrophilic and on surface forms OH^- groups that decrease the wetting properties of the PR. HMDS, formed on the surface from vapor at around 135 °C, replaces them with alkyl groups.
3. Coating AZ 5214E on RCD8 – the spin-coater applies this PR uniformly by spinning it at fast speeds. In this case, the rotating speed of 6000 rpm spreads the PR layer to form a thin film. Due to capillary forces, the layer at the edge of wafer is slightly elevated, which could result in an unwanted gap between the mask and the PR during exposure in contact mode. So, while spinning, the edge bead is removed by a small stream of solvent.
4. Softbake the PR – the 110 °C temperature the evaporation of the solvent agent causes PR hardening and additional thinning to final thickness of ~1,1 µm. Cooling of the wafer is needed before next step.
5. Exposure in contact mode – exposing the PR with a dose of 90 mJ/cm^2 (around 60 sec) using MA8 while the glass mask carrier is in contact with the surface of the PR coated substrate.
6. Developing with AZ 726 MIF (solution of TMAH and deionized water with surfactants) – RCD 8 is configured for development. The developer forms a "puddle" on the wafer dissolving exposed areas of PR. Then it is rinsed off and the wafer is spun for final drying with blowing nitrogen gas nozzle.

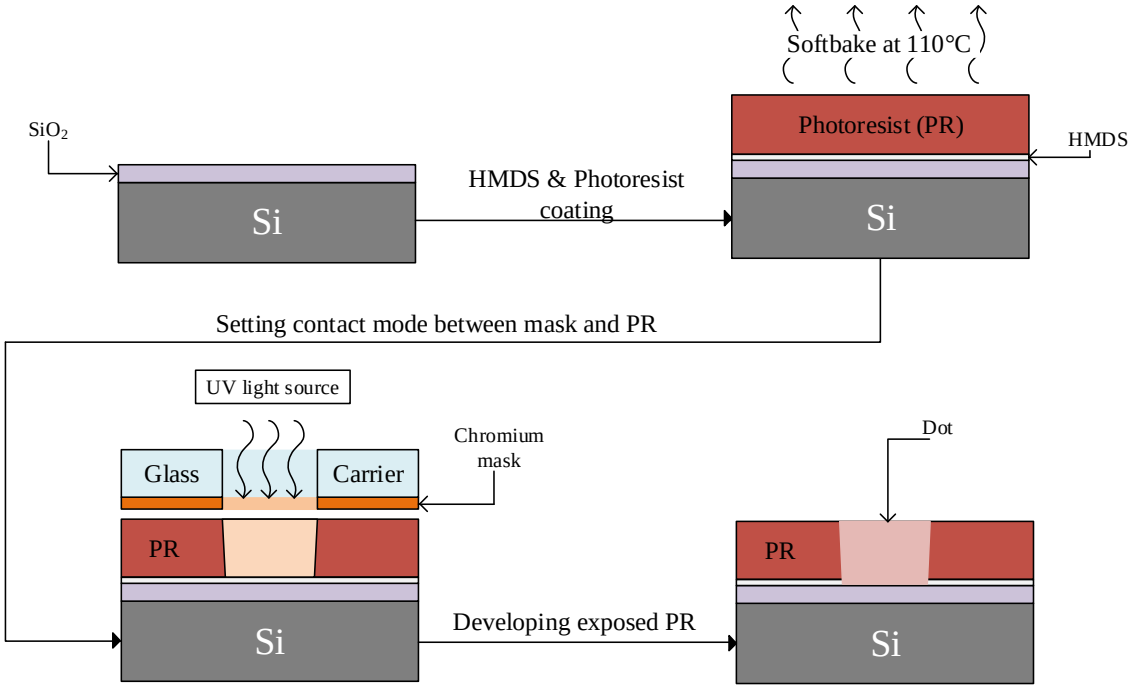

Fig. 3-4 Process chart of the lithography fabrication phase (not to scale).

After these process steps (see fig. 3-4) the result is an oxidised Si wafer coated with ~1,1 μm thick positive PR film with the desired pattern developed forming a negative polymeric mask (photo in fig. 3-5a). The PR profile achieved in the area of dots is expected to have a positive slope slightly less than 90° (>85°).

As stated in previous chapter, a smaller scale version of the layout has been prepared. Additional samples (whole 4" wafers) were provided with dots scaled to 0,5 μm in diameter and with a 1 μm/2 μm/5 μm pitch. To create such fine image with available lithography tools is proven difficult, therefore, they have been prepared in a foreign facility NIST (National Institute of Standards and Technology – USA) and are included in next fabrication and analysis steps. One example is shown in fig. 3-5b as a photo-image of the wafer after finished photolithography. It's important to note, that the thickness of these wafers is 525 μm with 100 up to 560 nm of thermal SiO_2.

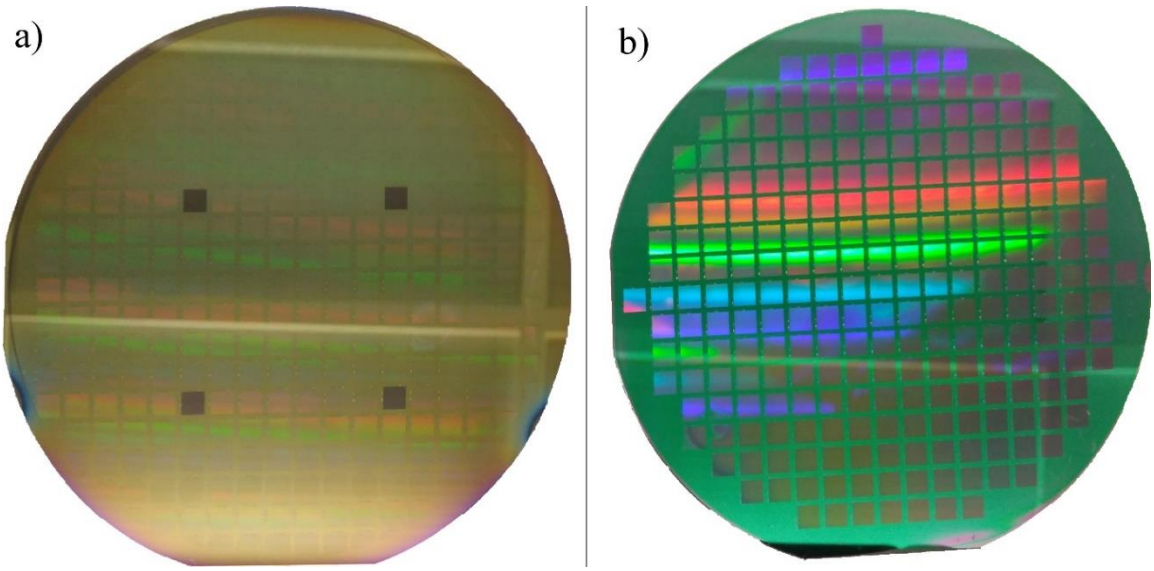

Fig. 3-5 Photos of wafers after photolithography: (a) 1 μm holes/ 4 μm pitch; (b) 0,5 μm holes/ 1 μm pitch.

3.3 Creating holes by plasma etching the SiO_2 and Si

In this stage of fabricating gecko pillars, the topology image has been developed on the PR and the SiO_2 layer is uncovered. In the next step, the SiO_2 is dry-etched in C_4F_8 plasma, while the PR is used as a masking layer. For etching, and later for Si etching, PlasmaPro 100 (Oxford Instruments Plasma Technology) DRIE of Si-based materials is used.

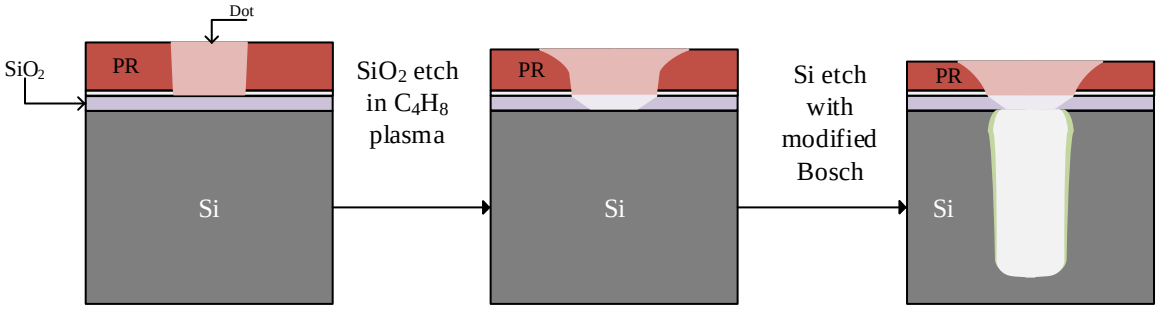

Fig. 3-6 Process chart for etching holes in silicon using modified Bosch process. (in the last step, green layers on the Si walls represent the

After the SiO_2 layer is gone (the parameters of plasma for SiO_2 etch are in table 3-1), the process parameters are set for Bosch etching process. This process step is very critical, because changing the process parameters has fundamental effect on the shape and desired quality of etched holes. Ideally, the profile would have smooth straight walls without under-etching of the mask (SiO_2), and the aspect ratio of >10:1. Two processes have been tried and optimized: modified basic Bosch process and smooth Bosch process.

Standard (basic) Bosch processes used in MEMS fabrication usually aim for high etch rates and vertical profile. [34] Setting the etching and passivation steps to shorter times than is usual in Bosch processes ensures, that the etch rate is slow enough to create small sized scallops. On fig. 3-6 a process chart of the two etching steps is shown, with emphasis on resist erosion. Due to highly accelerated anisotropic ions in the plasma, the PR edges erode, which might uncover the edges of the SiO_2 layers below, that might begin to erode too.

Table 3-1: Process parameters for etching of SiO_2 with table temperature at 5 °C.

Constant process parameters	Various times for different oxide thicknesses	
	Thickness [nm]	Time [s]
• pressure control setpoint at 4 Pa, • ICP power of 2500 W, • forward DC bias of ~120 V, • gas flow: $Q(C_4H_8)$ = 100 $cm^3.min^{-1}$, $Q(O_2)$ = 15 $cm^3.min^{-1}$,	100	30
	360	70
	560	105

3.3.1 Basic Bosch

First process was tried on the wafers with a layout of 1 µm and 4 µm pitch. After photolithography, the SiO_2 layer was etched and immediately after, the substrate table was cooled to – 10 °C and holes were etched for a total duration of 10 minutes (100 cycles). The process parameters (taken from [35]) used can be seen in table **3-2**.

Table 3-2 Process parameters for basic Bosch at -10 °C.

Process tree:	Parameter:	DEP[1]	ETCH
100 cycles ⌊ DEP ⌊ ETCH	ICP power [W]	600	600
	HF power [W] (DC Bias [V])	10 (~70)	30 (~135)
	Pressure [Pa]	1,5	1,5
	$Q(SF_6)$ [$cm^3.min^{-1}$]	10	50
	$Q(C_4H_8)$ [$cm^3.min^{-1}$]	110	10
	Time [s]	2	4

[1] - deposition of passivation layer

On fig. 3-7 below, the SEM images show the resulting structures using the basic Bosch process. The images were taken by Scanning Electron Microscope TESCAN LYRA3. From the images it is clear, that the scalloping is too small to be visible with current magnification. But measuring the width of the holes shows, that it has widened by ~320 nm from the originally designed diameter of 1 µm. Measured depth of ~8,5 µm indicates etching rate of 0,85 $\mu m.min^{-1}$. It's important to note, that the etch rate is not constant with increasing depth, due to process aspect ratio.

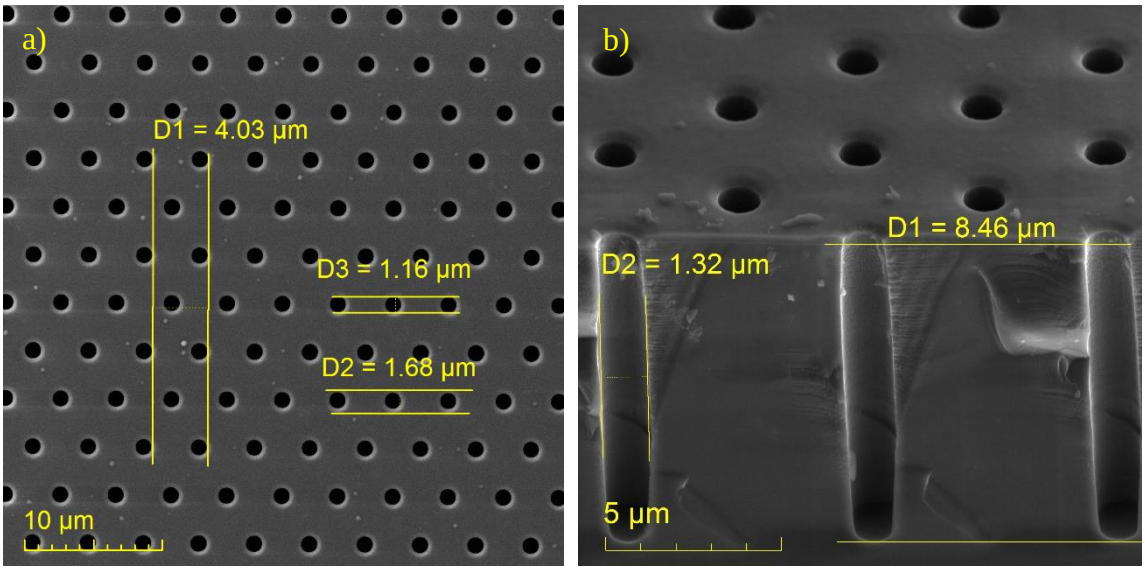

Fig. 3-7 SEM images of 1 µm holes with 4 µm pitch. (a) Top view of the etched holes and measuring the diameter of holes in SiO_2 layer and the erosion of this layer's edge. (b) Tilted cross section of holes and their dimensions.

3.3.2 Smooth Bosch modified process

The process in the previous chapter had eliminated a problem with large scalloping of the walls. The hole widening of ~30% is not a big problem with a 4 μm space between holes, but if the holes are half the diameter and spaced 1 μm from each other, there is a risk of the walls intersecting and, at best, the pillars in final phase might be too close to each other and start attracting themselves.

Therefore, the basic Bosch process needed to be slightly modified to acquire a good profile. A complete overhaul of basic Bosch process is needed -> smooth Bosch has a middle step between passivation and etching step, set to break through the passivation layer on the bottom before an actual Si etch occurs. The duration of this step needed to be optimized, so that the deposited C4F8 polymer is removed but the silicon is not yet etched. After this step, the actual etching of Si occurs. The process uses parameters from table 3-3 (optimised according to [15]).

Table 3-3 Process parameters for smooth Bosch - deep etching of holes into Si at 5 °C.

Process tree[1]:	Parameter:	DEP	BREAK[2]	ETCH #1	ETCH #2	ETCH #3
15 cycles DEP BREAK ETCH #1 15 cycles DEP BREAK ETCH #2 25 cycles DEP BREAK ETCH #3	ICP power [W]	1750	2000	2000	2000	2000
	HF power [W] (DC Bias [V])	-	40 (~120)	-	-	-
	Pressure [Pa]	6.7	4	4	4	4
	$Q(SF_6)$ [$cm^3.min^{-1}$]	10	200	120	170	200
	$Q(C_4F_8)$ [$cm^3.min^{-1}$]	200	10	10	10	10
	Time [s]	0,9	1,1	0,3	0,4	0,5

[1] - etch rates separated into 3 phases with increasing etch time for better profile control.
[2] - break through passivation layer

From the process tree in the table, it is obvious, that the process has more phases. It was important, that the wall profile would be as smooth and vertical as possible. That was done with dividing the process into 3 phases of different number of cycles, where the time and SF_6 flow during etching was set lower at the beginning for minimum scalloping at start. That time had to be increased after a few cycles, because the horizontal etching is decreasing with depth, which would result in narrower holes at the bottom, thus, the profile stops being vertical.

Small initial scalloping can be seen first few cycles on fig. 3-8 but further deep it disappears. The distance D1 marks the depth of ~4,3 μm, which, considering etch time of 2 min and 13 seconds (55 loops) translates to ~1.9 $\mu m.min^{-1}$. This time, the issue of hole widening has improved. Distance D2 indicates, that the hole diameter increased by no more than 16 % of the original diameter of 500 nm. The thickness of SiO_2 layer is not measured in the image, but different measurements showed a thickness of ~90 nm.

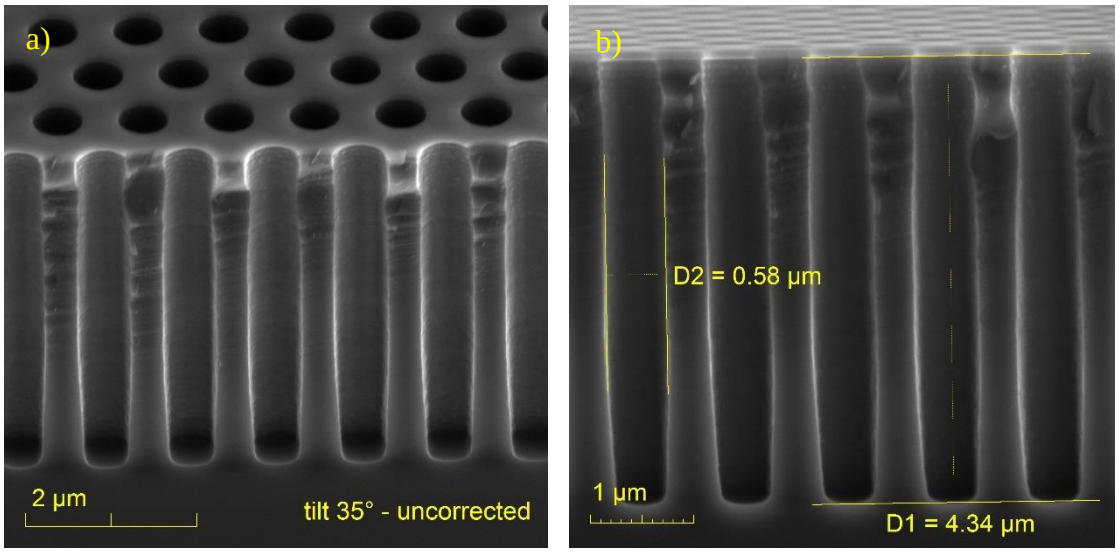

Fig. 3-8 SEM images of (a) tilted cross cross-section showing etched 500 nm holes with 1 µm pitch; (b) dimensions of deep silicon etching of these holes.

This variation of the Bosch process showed more than 2x increase of etch rate. Most likely, during passivation and etching cycles of the first process, basic Bosch suffers from over-passivation. The polymer layer deposition step inhibits the isotropic effectivity of the etching step downwards and also causes higher etching in the horizontal direction. This simple problem is eliminated in smooth Bosch by inserting a break-through step in between passivation and etching step to break the polymer.

3.4 Forming Parylene pillars

After the holes are etched with desired quality, they can now be used as a sort of form for making pillars out of Parylene C polymer. Before the deposition, the PR from the wafers is stripped and they are cleaned in O_2 plasma for removal of any residual organics, including the thin layer of passivation polymer. The backside of the wafers is covered with some adhesive tape to prevent Parylene C from forming there (for later backside Si removal). Fig. 3-9 shows the final fabrication steps of forming the Parylene pillars.

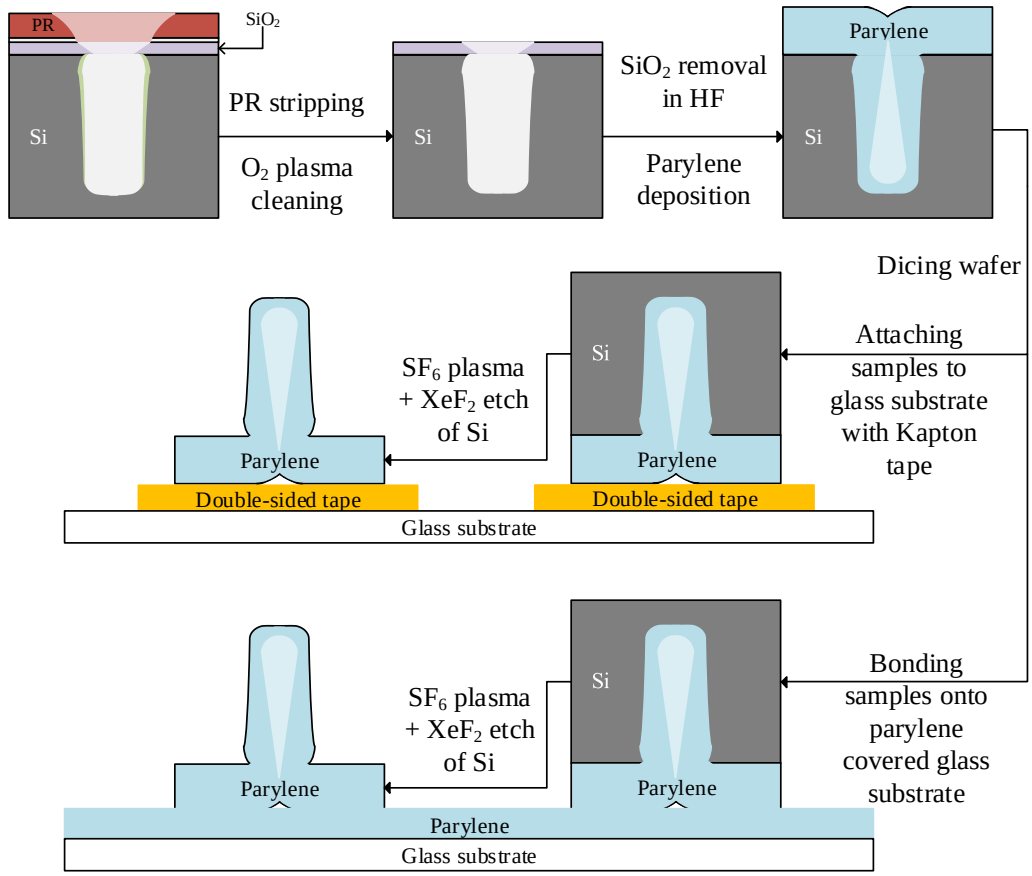

Fig. 3-9 Process chart showing formation of Parylene pillars (light blue shows a cavity inside the pillars), and their preparation for surface modification and adhesion force measurements. (not to scale)

Deposition is carried out in PDS 2010 Labcoter^{TM} 2 with the setup parameters from table 3-4. After polymer deposition, the wafers containing individual sets of pillars are diced into 5×5 mm^2 large pieces. Some of them are selected and mounted top-down onto a thin glass substrate with double sided Kapton tape. Chapter 2.3.1 was exploring a possibility of bonding two Parylene covered substrates together. Some samples were therefore mounted on a Parylene C covered glass substrate and put in an annealing furnace. The result was a moderately strong coherent bond, that is required to hold the polymer structures after XeF_2. At this point, the silicon substrate is fully exposed and its whole volume needs to be etched away to reveal Parylene C pillars.

Table 3-4 : Process parameters for Parylene C deposition using 4 g of Parylene C dimer (resulting in ~4 μm thick polymer layer).

Furnace temperature [°C]	Vaporizer temperature [°C]	Chamber (pressure) gauge temp. [°C]	Pressure setpoint [Pa]
690	175	135*	1,6

* – this temperature prevents polymer deposition on the pressure gauge.

Table 3-5 Setting of the annealing furnace for Parylene C bonding (taken and modified from[19]).

Chamber and table temperature [°C]	Process vacuum [Pa]	Press force applied [N]	Annealing time [min]
240	$< 8{,}22.10^{-5}$	10	60*

* – with a rising ramp of 5 °C. min^{-1}

Low process pressure is important for increasing the mean free path of gas molecules. The greater the mean free path, the easier it is for Parylene C monomers to fit through very small openings, such as the holes of gecko structures. However, a uniform growth of Parylene C is still limited by aspect ratio and is slowed down as the diameter of holes reduces with growing layer of polymer. That results in forming of a cavity inside the buried pillars. During annealing process, high vacuum may help removing most of the gas molecules from between the bondable surfaces and increasing the bonding strength.

The prepared samples, with a silicon thickness of 540 μm, are first etched in DRIE set to isotropic etching process. The SF_6 plasma has shown high isotropic etch rates under right conditions. But the Parylene structures cannot be uncovered in plasma, since they may be damaged by it and by elevated heat generated by high energy ion bombardment. For the same reason, the substrate had to be actively cooled with liquid nitrogen. Therefore, the samples were only thinned using SF_6 plasma isotropic etching down to around 180 μm thickness or less. After that, they were placed inside the vacuum chamber of an XeF_2 isotropic silicon etching system. The XeF_2 gas is non-reactive in any way with Parylene C, so the remaining silicon is etched away. The etching parameters of both processes are in table 3-6.

Table 3-6 Comparison of two different dry isotropic methods for 540 μm Si etching.

Etching method	ICP power [W]	Pressure [Pa]	$Q(SF_6)$ [$cm^3.min^{-1}$]	Cycles [-]	One cycle duration [s]	Etch rate[1] [$\mu m.min^{-1}$]
DRIE isotropic pre-etch	2500	10	300	13	120 (+30)[2]	~ 21
Etching in XeF_2 gas	-	267	-	200	30	~ 5,4

[1] - etch rates measured for 1 cm^2 of uncovered Si surface area;
[2] – each etching cycle followed by 30 seconds of inactivity for cooling purposes.

The table shows, that on 1 cm^2 of etched Si surface area, the DRIE is 4 times faster. Using only XeF_2 gas alone to etch those 0,5 mm thick samples would take around 2 hours. To save a little time and preserve fluoro-xenon gas supply, it's more effective to pre-etch it in SF_6 plasma.

After there is no trace of silicon on the samples, they are ready for surface modification or measurements. On fig. 3-10 the pillars of different dimensions are shown. Parylene C is non-conductive, so prior to SEM imaging, the samples hat to be sputtered on with a few nanometres of gold layer (~20 nm) to prevent charging.

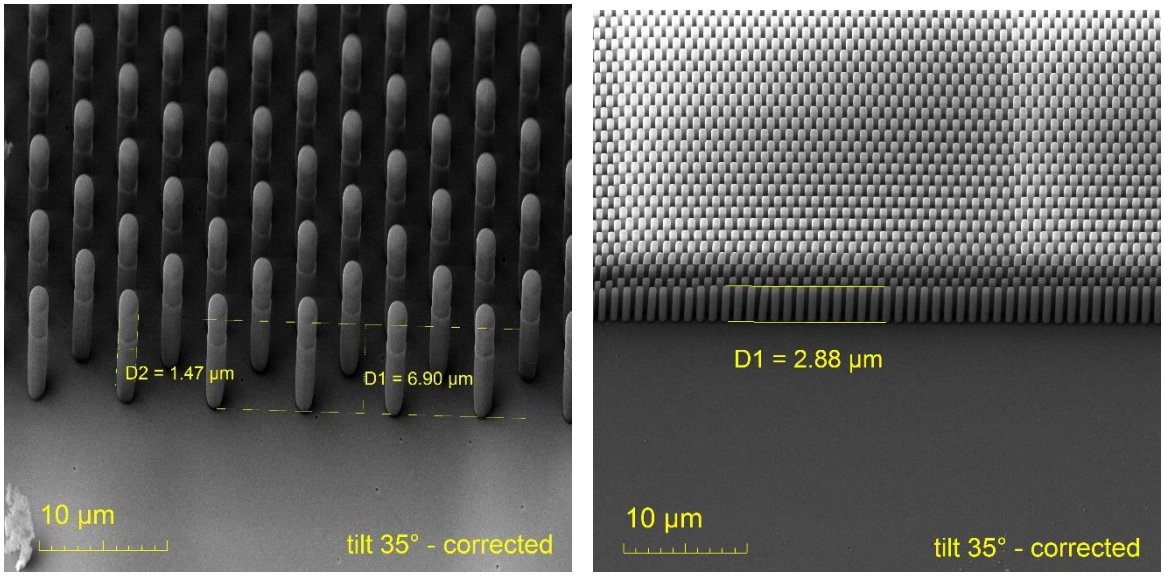

Fig. 3-10 SEM image of (a) ~7 µm tall pillars with ~1 µm diameter and 4 µm pitch; (b) ~2,9 µm tall pillars with ~500 nm diameter and 1 µm pitch

Few details have been noticed during SEM imaging. A flexing of some 500 nm pillars was visible, caused by repulsion of individual pillars after they were charged by a higher density of electron beam current for a few minutes (see fig. 3-11a,b). It means that the stiffness of these pillars might be comparable to the stiffness of gecko spatulas. Another observation confirmed the presumption, that the pillars are hollow (a cavity formed during Parylene C deposition), when some of the pillars broke by some external influence (see fig. 3-13c). This fact could mean a limitation for further miniaturisation of the pillars, since the cavity has been sealed shut under process vacuum. And because Parylene is the atmospheric pressure is several orders of magnitude higher, and the gas permeability of Parylene C is low [36] relative to the sudden pressure shock caused by venting the chamber to atmospheric pressure, thinner pillars might be prone to flattening, or imploding. This phenomenon was also observed in SEM and it is shown on fig. 3-11c.

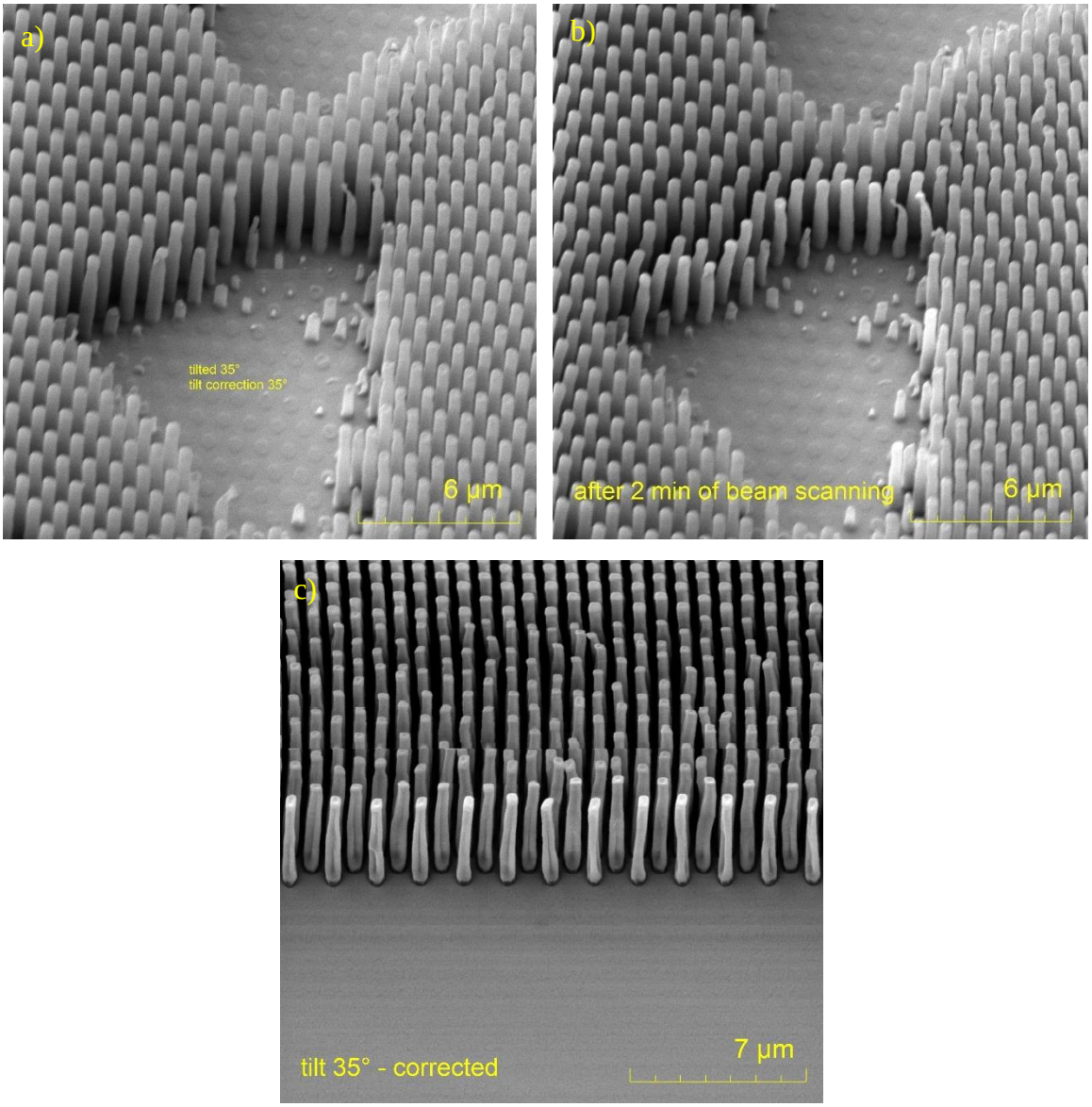

Fig. 3-11 (a) SEM image of 500nm/1 µm pillars on a 35° tilted surface (tilt corrected); (b) a comparison picture, showing bending of pillars after 2 minutes of scanning; (c) thinner pillars being flattened due to atmospheric pressure.

3.5 Forming bubbles on top of pillars

To possibly enhance adhesion of artificial gecko structures, one way is to further increase the surface area. And using knowledge of the fact, that filling holes with Parylene results in hollow structures, one can implement this idea into forming enlarged tips of pillars. The tips would be hollow as well and would resemble a "bubble". The cavity inside would make the bubble extra conformal to the roughness of the surface, which in theory might increase considerably surface-to-surface adhesion.

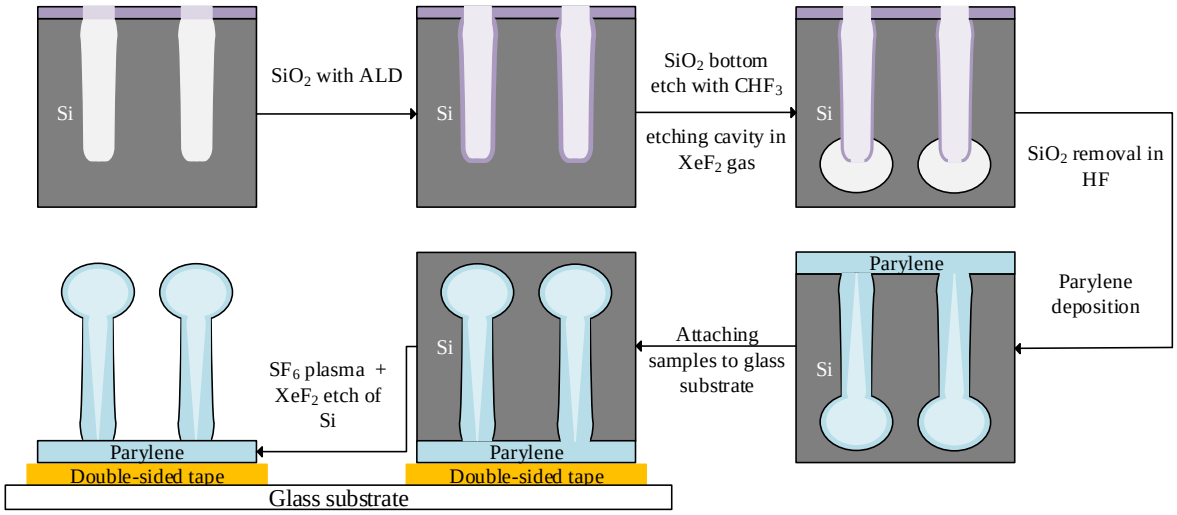

Fig. 3-12 Process chart for creating bubbles from Si substrate with holes etched after DRIE.

Fig. 3-12 shows manufacturing steps to form such structures. Using the technology of ALD and its ability to deposit conformal coating even on deep vertical surfaces, one can grow a thin (~ 5nm) layer of SiO_2 on the inside of the holes etched after Bosch process, while the original substrate oxide layer remains and cover the top surface.

Table 3-7 Process steps for plasma enhanced ALD of 5 nm SiO_2 using TDMAS as a precursor.

Step	Parameter	Value	Comments
1	Deposition chamber temp. [°C]	150	Set the chamber stabilisation and waiting for stabilization.
2	$Q(Ar)_1$ [$cm^3.min^{-1}$]	30	Set process argon flow rates.
3	$Q(Ar)_2$ [$cm^3.min^{-1}$]	100	
4	TDMAS pulse time [s]	0,4	Precursor pulse at room temp., followed by 5 sec. purge.
5	$Q(O_2)$ [$cm^3.min^{-1}$]	50	Oxygen flow for plasma step
6	Plasma ICP [W]	300	Plasma turned on for 20 sec.
7	Cycles [-]	80	Number of repetitions from step **4** for 5 nm thin SiO_2 layer.

The process of atomic layer deposition, that was used (table 3-7), runs under medium vacuum below 0,1 Pa. The prefixed "plasma enhanced" points to the fact, that the process uses O_2 plasma as a surface precursor activation that sets a base for TDMAS precursor. One pulse of 0,4 seconds equals around 4,1 mg of the silane precursor being consumed. One cycle creates an oxide layer of 0.63 Å, so for a required 5 nm of SiO_2, 80 cycles are needed.

The thin ALD SiO_2 layer on the bottom of the holes is etched through with a CHF_3 plasma in RIE (see table 3-8). After the Si on the bottom is revealed, a cavity is etched into it with an XeF_2 gas diluted in N_2 for a short period of time (depending on the desired bubble diameter). The parameters of the etching are in table 3-8.

Table 3-8 Parameters of processes used in forming bubble cavities in silicon.

Etching method	CCP power [W]	Pressure [Pa]	$Q(CHF_3)$ [$cm^3.min^{-1}$]	Q(Ar) [$cm^3.min^{-1}$]	Etch time [s]
RIE SiO_2 etch in CHF_3	200	4	12	38	40
	XeF_2 pressure [Pa]	N_2 pressure [Pa]	Cycles [-]		One cycle duration [s]
Etching in XeF_2 gas	200	400	1-2*		5-10*

* - etching of such small cavities is very dependent on the etched surface area and temperature.

To optimize the time needed for etching of ALD oxide at the bottom of a hole with a certain depth had to be optimizes, which was not a difficult task. Controlling the etching of XeF_2 was, on the other hand, very difficult because the amount of material etched is considerably little, and there is a risk of over-etching the bubbles.

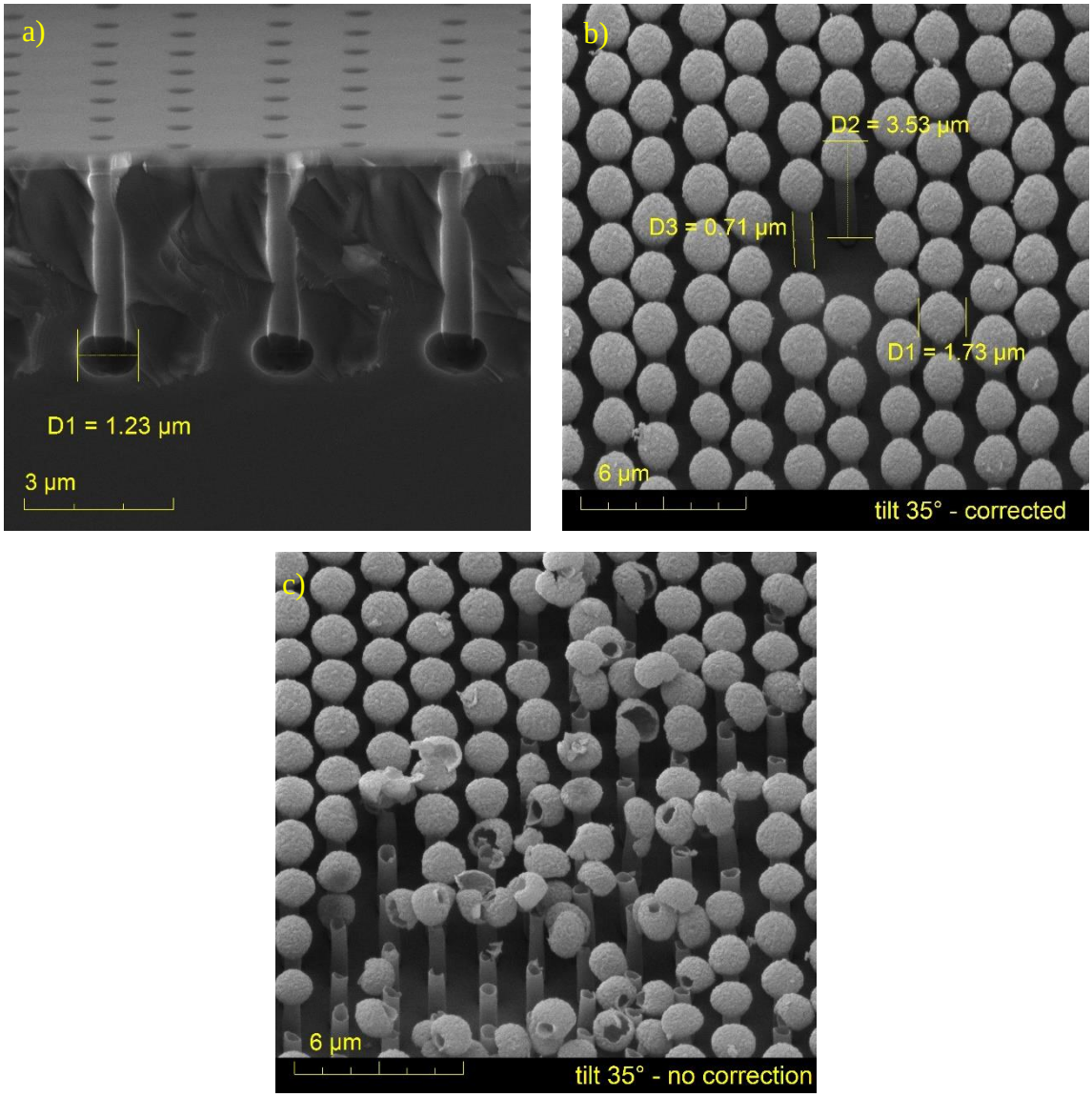

Fig. 3-13 SEM images (a) cross-section of holes with etched cavities for bubble formation; (b) view on Parylene bubble structures with 35° tilted surface (tilt corrected) and their dimensions; (c) proof, that pillars and bubbles are hollow.

3.6 Surface modifications procedures

Surface cure with oxygen plasma:

- The chamber was depressurized below 50 Pa; the flow of oxygen was set to $Q(O_2) = 25\ cm^3.min^{-1}$, and the plasma was fired with 300 W power;
- Duration of the oxygen plasma activation was from 1-1,5 minute and tests were taken on a Parylene C deposited surface, which shown, that the activation has degraded over time, but slowly;
- It is a necessary step before SiO_2 ALD or any silane cross-linking, because it creates OH^- groups.

ALD modification of Parylene surfaces with thin layer (5 nm) of SiO_2:

- An important step before crosslinking β-keratin on gecko biomimetic structures. Unfortunately, the only ALD process chart available for this cause (discussed in previous chapter) is incompatible with Parylene C structures. Possibly, too much strain from plasma radicals with combination of high temperature during ALD on the structures results in their complete destruction.
- The samples, however, survived intact under the temperature alone, therefore the possibility of ALD cover of structures remains open, if a different process parameters are implemented.

Keratin binding on SiO_2

1.) Oxygen plasma activation;
2.) Linking APTES:
    a. Using vacuum oven or Self-Assembly Monolayer chamber– applying 20 ul of APTES near samples -running the process at 120°C/30min;
    b. With toluene:
        - rapidly immersing samples in a solution of 2% V/V APTES in dry toluene;
        - rinse in toluene, then methanol and finally water (each time 5 min and with agitation for the last 2);
        - annealing of the samples at 120C for 2h;
3.) Prepared samples need to be stored dry (in N_2) if possible or be use the same day;
4.) Incubation in 10% glutaraldehyde in potassium-phosphate buffer solution (PBS) (10 mM, pH 7) for 1 hour;
5.) Rinse in PBS and then water twice (each time 5 min under agitation)
6.) Next step is adding keratin of 0.1mg/ml in PBS or other preferred buffer (it's important to mind the Ph of the solution so that the protein stays nicely folded) and leave it for 2h (or overnight);
7.) Rinse in PBS (twice with agitation) and storing wet (in PBS).

4 WETTABILITY AND ADHESION MEASUREMENT

First method used in this chapter is contact angle analysis of various surfaces using water droplets, thus, determining the hydrophobicity or hydrophilicity of the samples. Secondly, the adhesive force direct measurements of these samples are carried out using AFM equipment to measure force curves on the surface.

4.1 Contact angle measurement

Measuring the wettability of different surface variations is a simple, but important step to determine adhesion properties on the surface. It has been done using a SEO Phoenix 300 contact angle analyser consisting of an adjustable table for samples, a water syringe holder with a PC controlled stepping motor (with manual screw override) for dispensing water droplets. The imaging is done with an optically adjustable camera against white LED illuminated background and image processing using Surfaceware 8 software. The software features a surface energy calculator, curved surface sample measuring function

A series of comparative measurements of various surfaces has been carried out. Two variations: unstructured (flat) and structured (pillars/bubbles) surfaces of Parylene C have been observed, either untreated or treated/modified with O_2 plasma, SiO_2 (ALD), silanes and β-keratin.

On fig. 4-1a, the surface of untreated Parylene C shows a contact angle >90°, which makes the sample slightly hydrophobic. On the contrary, fig. 4-1b shows, that treating the unstructured Parylene surface with oxygen plasma significantly increases the adhesion.

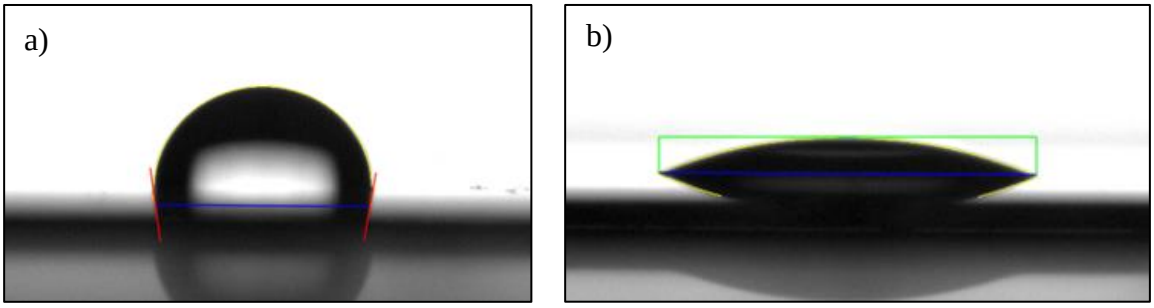

Fig. 4-1 Contact angle of a water drop on: (a) untreated Parylene C flat surface (99°) and (b) flat Parylene C surface treated with O_2 plasma (23°)

Parylene pillars of 0,5 μm diameter and 1 μm pitch (fig. 4-2) showed a different result when treated with plasma. The roughness caused by the structures present made the surface more hydrophobic than is the case of an untreated flat Parylene surface. Therefore, it has been concluded, that the plasma treatment might not have an effect on surface hydrophobicity and the and that there is an apparent correlation with the behaviour of a water droplet on a rough surface explained by Wenzel and Cassie and discussed in chapter 2.6.4.

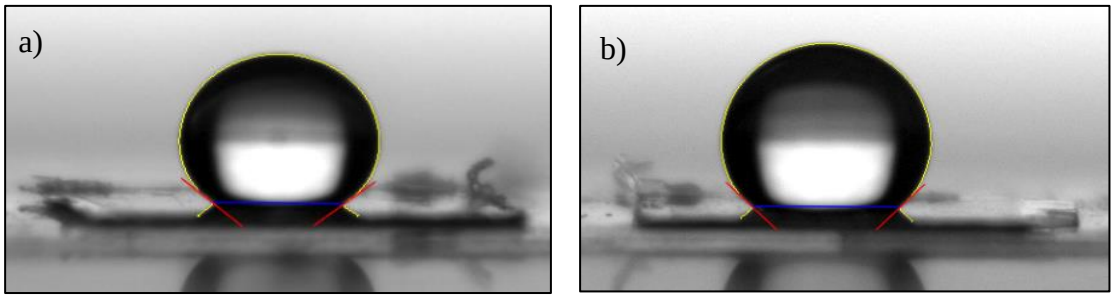

Fig. 4-2 Contact angle of a water drop on Parylene C 500 nm/1 μm pillar structures with: (a) untreated surface (140°) and (b) plasma treated surface (134°).

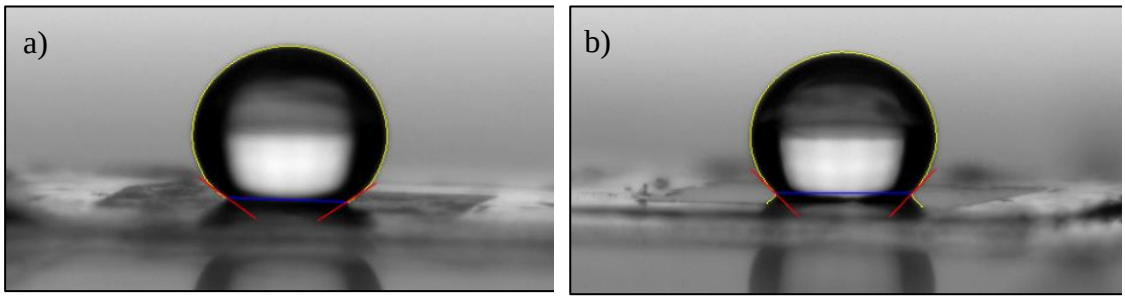

Fig. 4-3 Contact angle of a water drop on Parylene C 500 nm/2 μm bubble tip (1,4 μm diameter) structures with: (a) untreated surface (144°) and (b) plasma treated surface (133°).

The results of contact angle measurements on the bubble structure surface (fig. 4-3) are surprisingly similar to the results on the pillars. In both cases, however, oxygen plasma treated structures showed minor decrease in contact angle, but it is negligible. Worth mentioning might also be contact angle measurements of different surface modifications of flat Parylene C (deposited on silicon). APTES showed an angle of 63° on the Parylene and SiO_2 phase (fig. 4-4a) which was expected. A higher angle on fig. 4-4b probably means, that no silane link occurred. A very hydrophilic surface of ALD silicon oxide is not surprising, but the angle is very close to oxygen plasma treated Parylene surface (fig. 4-4c). An attempt to link animal keratin onto the Parylene surface with no SiO_2 layer was made, but following the image on fig. 4-4d, its possible, it was unsuccessful.

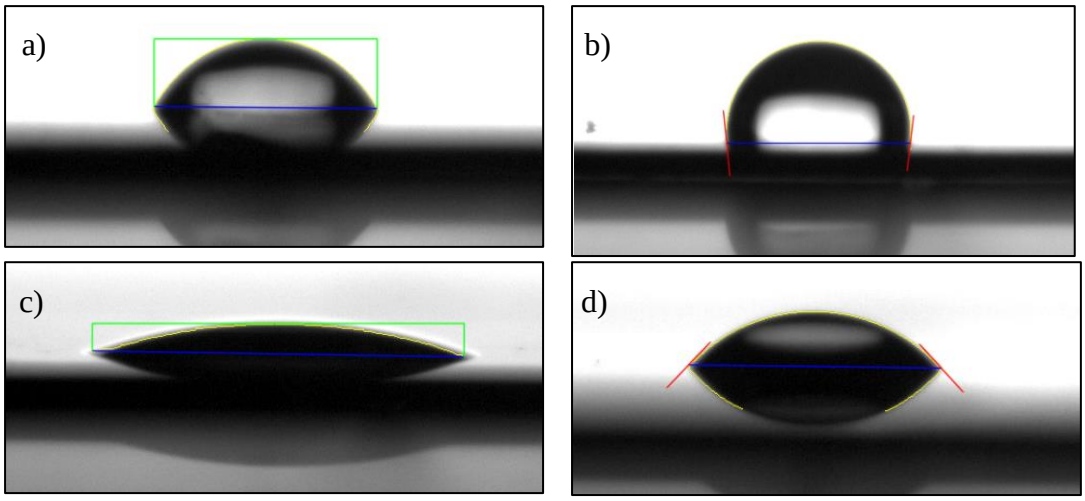

Fig. 4-4 (a)APTES on Parylene C + ALD SiO_2 (63°); (b) APTES on Parylene C (96°); (c) ALD SiO_2 on Parylene C (18°); (d) Parylene C with ALD SiO_2 + APTES and Glutaraldehyde crosslinkers for β-keratin (47°)

4.2 AFM measurements

AFM measurements were carried out with an ICON-SPM Bruker in AFM – contact mode and also two different cantilevers were used: a tip-less cantilever from ScanSens GmbH model: CSG01/TL/15 with a spring constant of k = 0.1 - 0.6 $N.m^{-1}$ and a custom modified ScanSens tip-less cantilever of same model.

4.2.1 Creating custom made spherical tip cantilever

A CSG01 cantilever had a glass sphere of ~100 μm glued as a tip with the help of an epoxy adhesive while the cantilever was mounted onto the probe station. The procedure is shown on Fig. 4-5.

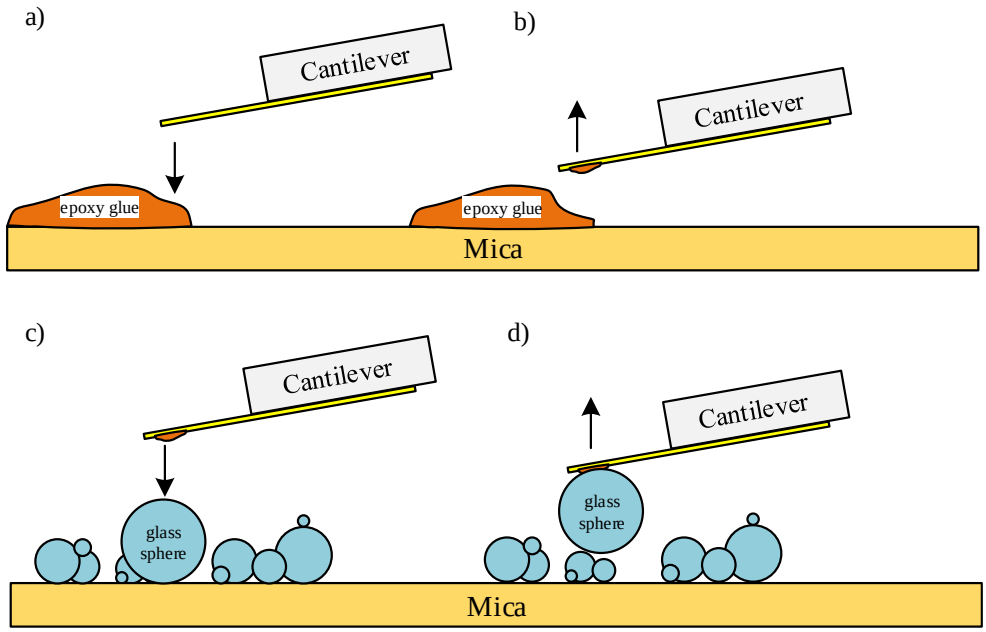

Fig. 4-5 Mounting of glass sphere onto the tip-less cantilever: (a) steadily approaching the surface with epoxy adhesive; (b) as the adhesive is applied, the cantilever moves above a spill of glass spheres; (c) approaching a fitting sphere and waiting for a few seconds; (d) the glass sphere is glued onto the cantilever and it waits to dry.

This glass-sphere mounted cantilever was specifically made for measuring adhesive forces on Parylene C structures (pillars and bubbles). At the sample-tip connection it would comply to the flexible structures better than a tip-less cantilever and might measure a local adhesion force of a group of pillars/bubbles.

The original cantilever's properties are listed in Table 4-1 and will all change after glass sphere has been mounted (except the spring constant *k*). Custom created glass sphere cantilever is on Fig. 4-6.

Table 4-1 Physical properties of CSG01/TL/15 cantilevers (according to manufacturer).

Length [μm]	Width [μm]	Thickness [μm]	Resonant frequency [kHz]	Spring constant *k* [$N.m_{-1}$]
450 ± 5	49	2,5	11 - 19	0,1 – 0,6

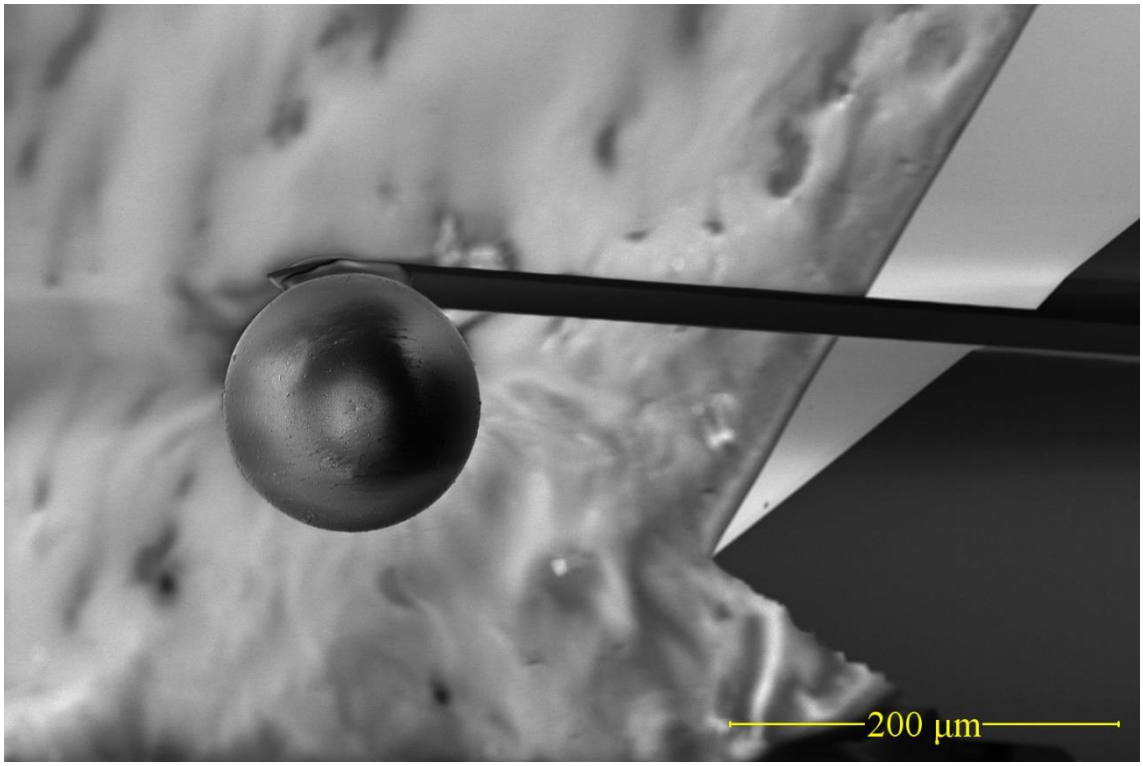

Fig. 4-6 An SEM image of the glass sphere mounted on ScanSens cantilever.

4.2.2 Force-distance Curves

The force curves were measured on three Parylene surfaces: a flat, unstructured surface and structured surfaces (pillars and bubbles). Tested were also variations, where another same three surfaces were cured with oxygen plasma (using parameters from chapter 3.6). The measurements and AFM control has been done with a Bruker software tool Nanoscope 9.6.

Before measurement (and after each cantilever exchange) the parameter calibration of both cantilevers, which were used, had taken place. Especially the deflection sensitivity has been updated and the spring constant *k* was determined from Thermal Tune tool. Both cantilevers had the same *k* value of 0,2 $N.m^{-1}$, which is important for adhesion force calculations from cantilever deflection. Another influential factor is relative air humidity, which varied from 40 – 50% and had often taken negative effect on the measurements, when surface humidity caused high tip-to-surface capillary adhesion. That also had to be taken into consideration.

Figures from 4-9 to 4-14 show all six adhesion force plots of studied samples. The resulting adhesion force difference between untreated and oxygen plasma treated flat Parylene C surface correlates with findings in chapter 4.1, where the contact angle difference was expected. Measurements on the structures, once again, have shown that there is no great difference between structured surface properties which have been treated with oxygen plasma, and those that haven't. The adhesion force was measured as a difference between points marked *a* and *f* in the plots.

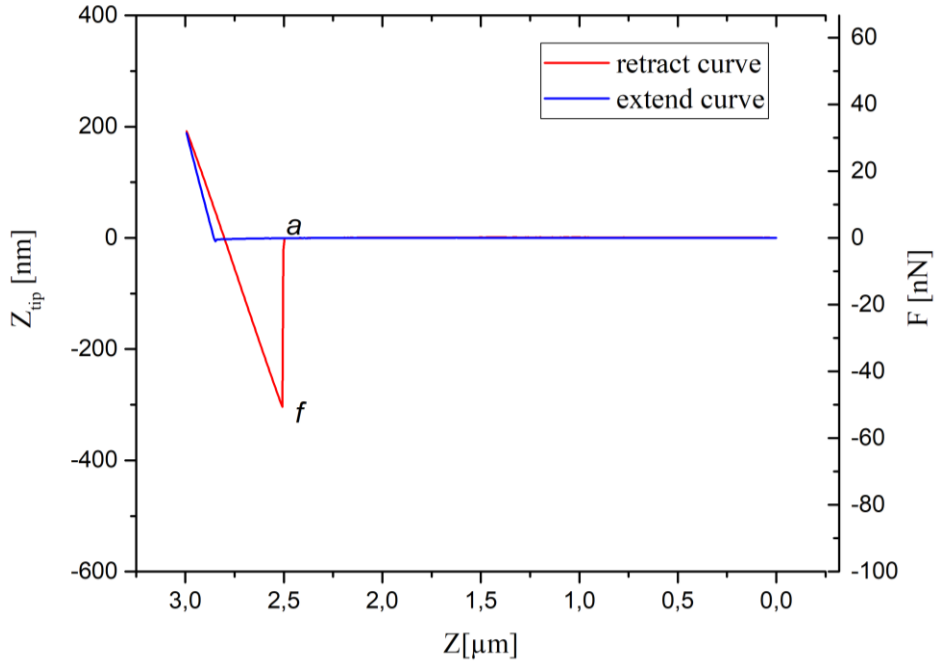

Fig. 4-7 Tip-less ScanSens probe – on flat Parylene C cured with O_2 (force ~ 69 nN). Graph zero is fit to extend curve.

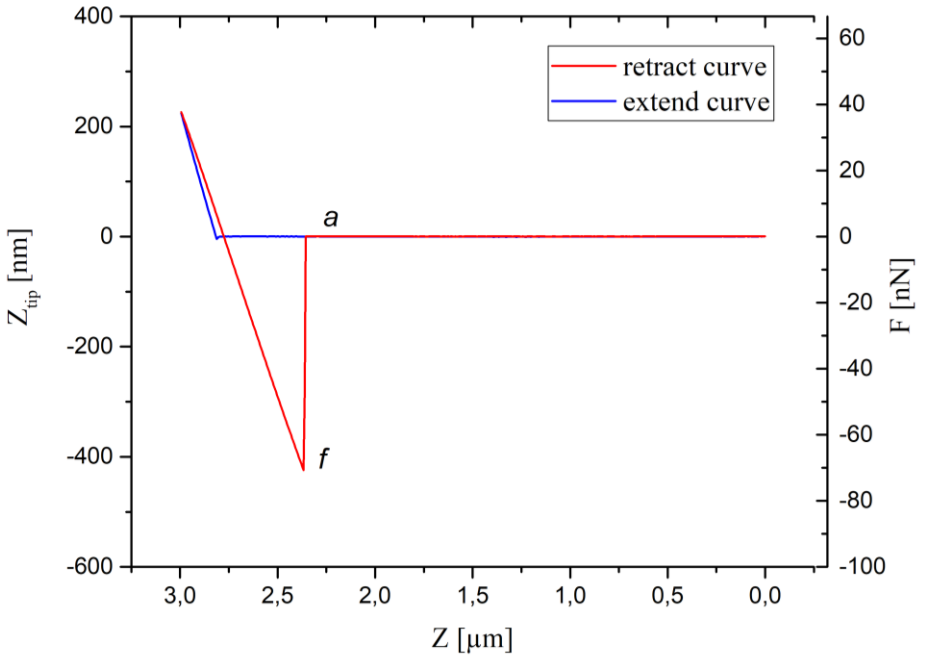

Fig. 4-8 Tip-less ScanSens – flat Par. C (force ~ 49 nN).

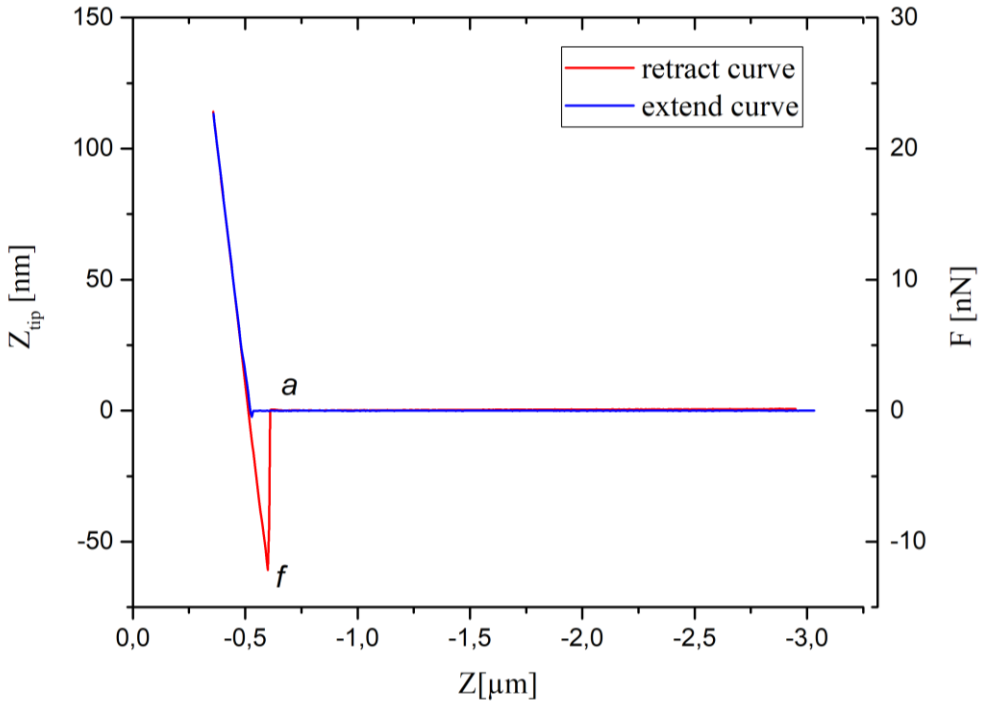

Fig. 4-9 Glass sphere mounted ScanSens probe – on pillar structured sample (0,5/1 µm), untreated (force ~ 13 nN).

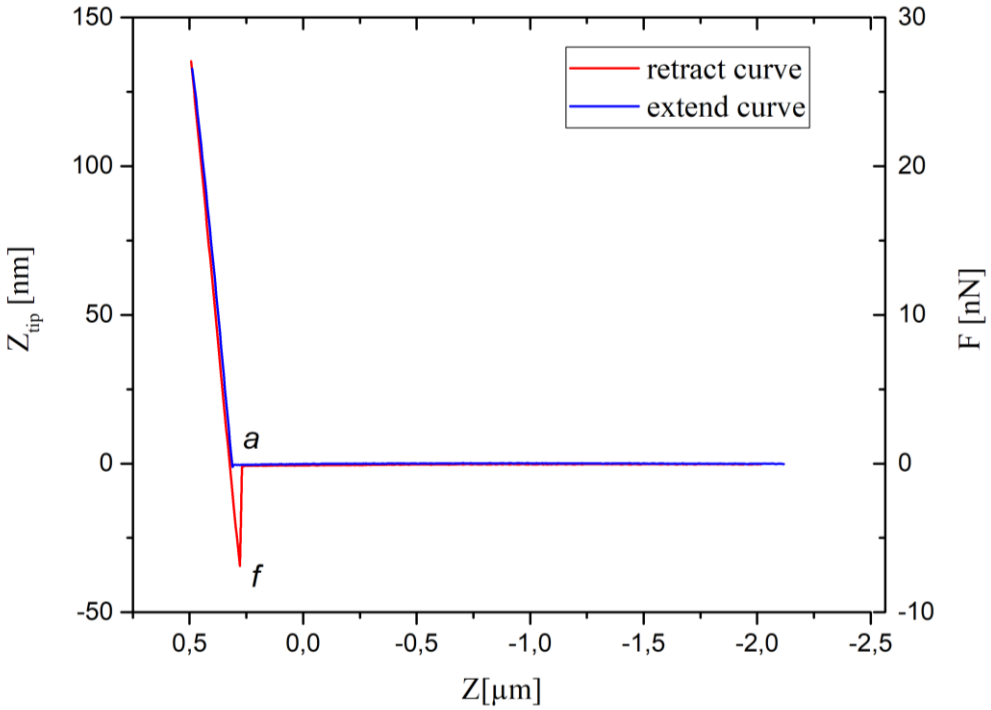

Fig. 4-10 Glass sphere mounted ScanSens probe – on pillar structured sample (0,5/1 µm), treated with O_2 plasma (force ~ 7 nN).

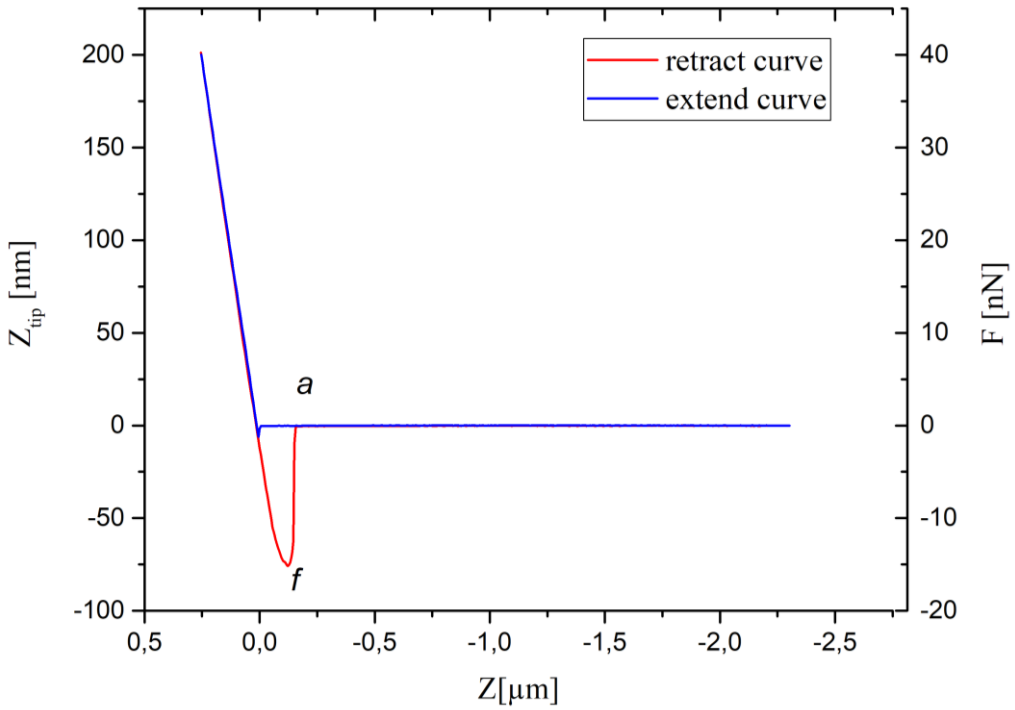

Fig. 4-11 Glass sphere mounted ScanSens probe – measurement on bubbles sample (0,5/2 µm), not treated (force ~ 16 nN).

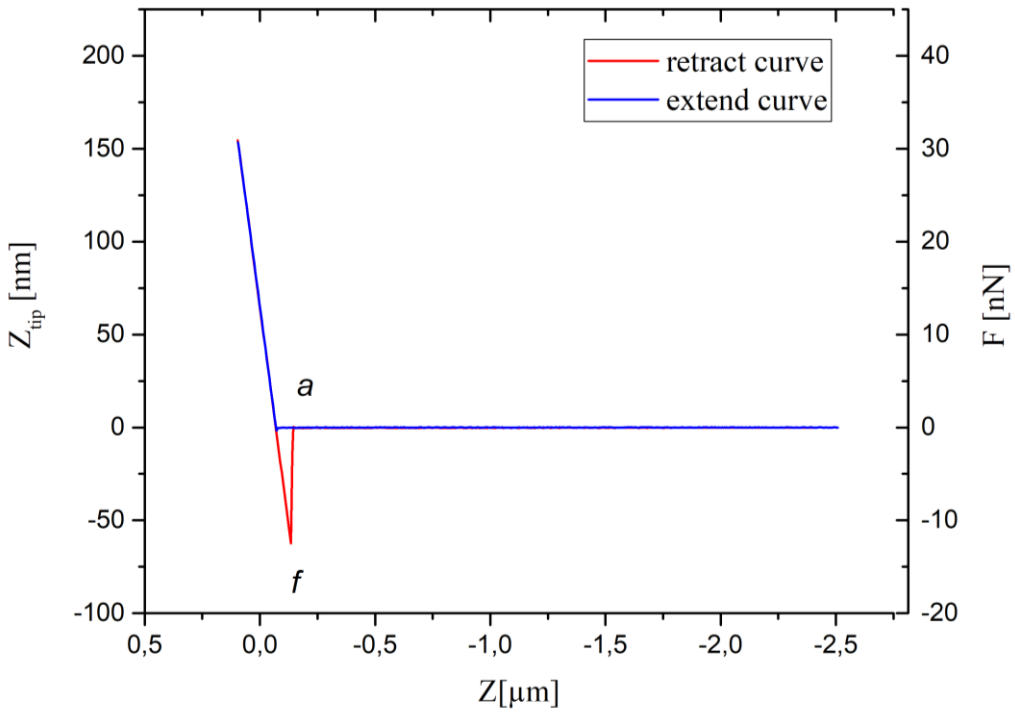

Fig. 4-12 Glass sphere mounted ScanSens probe – measurement on bubbles sample (0,5/2 µm) treated with O_2 plasma (force ~ 13 nN).

5 CONCLUSIONS

Researching this work's topic, *Gecko mimicking surfaces*, showed, that there have been numerous attempts to create structures simulating adhesion properties of a gecko (especially the Tokay Gecko) and some ideas to create functional biomimetics have been successful. Some interest has also arisen in the commercial sphere with the prospect of utilizing aforementioned qualities for production of dry adhesives, that would be able to stick to almost any surfaces.

A consensus has not yet been stated among scientists conducting research regarding adhesion of gecko setae. There are three main factors, which play a role: weak van der Waals forces, capillary forces, and electrostatic forces, that require further research to establish which one is dominant.

Prior to that, some structures have been created for measurements. Prepared were micropillars made of polymer Parylene C, which might have some comparable mechanical properties with biological setae of a gecko (such as stiffness, etc.). Improving the tips of the micropillars with bubbles was also accomplished and their conformality (due to being hollow) mechanically resembles a set of gecko lamellae. Next aim was modifying the surfaces of these micropillars and bubbles with materials harbouring better adhesion when bind to other materials, such as silicon dioxide SiO_2 and a crosslinker (SiO_2-APTES/GTA), to promote bonding of β-keratin.

As was discussed in chapter 3.6, some of the surface modifications implementations failed in being applied on Parylene C structures. One of the important ones, plasma enhanced ALD growth of SiO_2 is too destructible. However, there are methods of oxide growth in ALD, which do not require plasma activation pulses. Thermal processes, that use water or ozone [37] [38] exist, but would need to be accommodated for available equipment, which was used for progression purposes of this work. There are also different techniques of SiO_2 deposition, including magnetron sputtering and PECVD (it's also plasma enhanced, but grow rates are much higher [39]).

These reasons ruined the intentions of applying crosslinkers to created structures, but an attempt to bind the crosslinkers directly onto Parylene C was made, without the intermediate oxide layer. The contact angle measurements haven't concluded, if the binding of silanes, or even crosslinking keratin took place. A rather advanced methods of chemical characterisation are required.

The results of this work demonstrate, that it is very much possible to create desired structures and even the simplest modifications can change their surface properties considerably.

6 REFERENCES

[1] K. Autumn and J. Puthoff, "Properties, Principles, and Parameters of the Gecko Adhesive System," in *Biological Adhesives*, A. M. Smith, Ed., ed Cham: Springer International Publishing, 2016, pp. 245-280.

[2] B. Bhushan, "Bioinspired structured surfaces," *Langmuir,* vol. 28, pp. 1698-714, Jan 24 2012.

[3] M. Carlo and S. Metin, "A Biomimetic Climbing Robot Based on the Gecko," *Journal of Bionic Engineering,* vol. 3, pp. 115-125, 2006/09/01/ 2006.

[4] A. K. Geim, S. V. Dubonos, I. V. Grigorieva, K. S. Novoselov, A. A. Zhukov, and S. Y. Shapoval, "Microfabricated adhesive mimicking gecko foot-hair," *Nat Mater,* vol. 2, pp. 461-3, Jul 2003.

[5] H. Lee, B. P. Lee, and P. B. Messersmith, "A reversible wet/dry adhesive inspired by mussels and geckos," *Nature,* vol. 448, pp. 338-41, Jul 19 2007.

[6] M. T. Northen and K. L. Turner, "A batch fabricated biomimetic dry adhesive," *Nanotechnology,* vol. 16, pp. 1159-1166, 2005.

[7] H. Izadi, K. M. Stewart, and A. Penlidis, "Role of contact electrification and electrostatic interactions in gecko adhesion," *J R Soc Interface,* vol. 11, p. 20140371, Sep 6 2014.

[8] W. Federle, "Why are so many adhesive pads hairy?," *J Exp Biol,* vol. 209, pp. 2611-21, Jul 2006.

[9] R. G. Beutel and S. N. Gorb, "Ultrastructure of attachment specializations of hexapods, (Arthropoda): evolutionary patterns inferred from a revised ordinal phylogeny," *Journal of Zoological Systematics and Evolutionary Research,* vol. 39, pp. 177-207, Dec 2001.

[10] G. Cao, *Nanostructures & Nanomaterials: Synthesis, Properties & Applications*: Imperial College Press, 2004.

[11] H. L. Liu and G. X. Cao, "Effectiveness of the Young-Laplace equation at nanoscale," *Scientific Reports,* vol. 6, Apr 1 2016.

[12] R. G. Horn and D. T. Smith, "Contact Electrification and Adhesion between Dissimilar Materials," *Science,* vol. 256, pp. 362-364, Apr 17 1992.

[13] K. Nojiri, *Dry Etching Technology for Semiconductors*: Springer International Publishing, 2014.

[14] S. Franssila and L. Sainiemi, "Reactive Ion Etching (RIE)," ed, 2015, pp. 2911-2921.

[15] H. V. Jansen, M. J. de Boer, S. Unnikrishnan, M. C. Louwerse, and M. C. Elwenspoek, "Black silicon method X: a review on high speed and selective plasma etching of silicon with profile control: an in-depth comparison between Bosch and cryostat DRIE processes as a roadmap to next generation equipment," *Journal of Micromechanics and Microengineering,* vol. 19, Mar 2009.

[16] I. Gablech, J. Somer, Z. Fohlerova, V. Svatos, J. Pekarek, S. Kurdik, *et al.*, "Fabrication of buried microfluidic channels with observation windows using femtosecond laser photoablation and parylene-C coating," *Microfluidics and Nanofluidics,* vol. 22, Sep 2018.

[17] D. H. Xu, B. Xiong, G. Q. Wu, Y. C. Wang, X. Sun, and Y. L. Wang, "Isotropic Silicon Etching With XeF2 Gas for Wafer-Level Micromachining Applications," *Journal of Microelectromechanical Systems,* vol. 21, pp. 1436-1444, Dec 2012.

[18] "PDS 2010 LABCOTER™ 2 Parylene Deposition System: Operator's Manual," Rev 37 ed: Specialty Coating Systems, 2004.

[19] H. Kim and K. Najafi, "Characterization of low-temperature wafer bonding using thin-film parylene," *Journal of Microelectromechanical Systems,* vol. 14, pp. 1347-1355, 2005.

[20] P. D. Uwe Stöhr, "Surface activation of plastics by plasma for adhesion promotion," P. E. GmbH, Ed., ed: WOTech Technical Media, 2016, p. 9.

[21] M. Lessel, O. Baumchen, M. Klos, H. Hahl, R. Fetzer, M. Paulus, *et al.*, "Self-assembled silane monolayers: an efficient step-by-step recipe for high-quality, low energy surfaces," *Surface and Interface Analysis,* vol. 47, pp. 557-564, May 2015.

[22] P. G. Pape, "15 - Adhesion Promoters," in *Handbook of Adhesives and Surface Preparation*, S. Ebnesajjad, Ed., ed Oxford: William Andrew Publishing, 2011, pp. 369-386.

[23] R. W. Johnson, A. Hultqvist, and S. F. Bent, "A brief review of atomic layer deposition: from fundamentals to applications," *Materials Today,* vol. 17, pp. 236-246, 2014/06/01/ 2014.

[24] S. Thapa, "DEFECTS AND FERROMAGNETISM IN TRANSITION METAL DOPED ZINC OXIDE," 2016.

[25] P. Bouckenooge, H. Terryn, and I. Vandendael, "Ultimate Lateral Resolution in Electron Microscopy by FE-Auger."

[26] B. Voigtländer, *Scanning probe microscopy : atomic force microscopy and scanning tunneling microscopy*. Heidelberg: Springer Heideberg New York Dordrecht London, 2015.

[27] G. Goring, P. I. Dietrich, M. Blaicher, S. Sharma, J. G. Korvink, T. Schimmel, *et al.*, "Tailored probes for atomic force microscopy fabricated by two-photon polymerization," *Applied Physics Letters,* vol. 109, Aug 8 2016.

[28] Bruker. (2010). *SPM Training Guide*. Available: http://www.nanophys.kth.se/nanophys/facilities/nfl/afm/icon/bruker-help/Content/SPM%20Training%20Guide/SPM%20Training%20Guide.htm

[29] R. S. Hebbar, A. M. Isloor, and A. F. Ismail, "Chapter 12 - Contact Angle Measurements," in *Membrane Characterization*, N. Hilal, A. F. Ismail, T. Matsuura, and D. Oatley-Radcliffe, Eds., ed: Elsevier, 2017, pp. 219-255.

[30] S. S. Latthe, C. Terashima, K. Nakata, and A. Fujishima, "Superhydrophobic Surfaces Developed by Mimicking Hierarchical Surface Morphology of Lotus Leaf," *Molecules,* vol. 19, 2014.

[31] Y.-C. Tsai and W.-P. Shih, "Artificial Petal Effect on Nanofibrillar Parylene™ Surface," *The Journal of Adhesion,* vol. 88, pp. 32-54, 2012/01/01 2012.

[32] A. Marmur, "Equilibrium contact angles: Theory and measurement," *Colloids and Surfaces a-Physicochemical and Engineering Aspects,* vol. 116, pp. 55-61, Sep 16 1996.

[33] S. D. Strauss, *The Big Idea: How Business Innovators Get Great Ideas to Market*: Dearborn Trade Pub., 2002.

[34] O. I. P. Technology. (2019, 19 May 2019). The Bosch Process for Etching Micro-Mechanical Systems (MEMS) - Principles, Advances and Applications. Available: https://www.azonano.com/article.aspx?ArticleID=2738

[35] K. Miller, M. X. Li, K. M. Walsh, and X. A. Fu, "The effects of DRIE operational parameters on vertically aligned micropillar arrays," *Journal of Micromechanics and Microengineering,* vol. 23, Mar 2013.

[36] A. Tanioka, N. Fukushima, K. Hasegawa, K. Miyasaka, and N. Takahashi, "Permeation of gases across the poly(chloro-p-xylylene) membrane," *Journal of Applied Polymer Science,* vol. 54, pp. 219-229, 1994/10/10 1994.

[37] D. Hiller, R. Zierold, J. Bachmann, M. Alexe, Y. Yang, J. W. Gerlach, *et al.*, "Low temperature silicon dioxide by thermal atomic layer deposition: Investigation of material properties," *Journal of Applied Physics,* vol. 107, p. 064314, 2010/03/15 2010.

[38] L. Han and Z. David Chen, *Ultrathin SiO2 Films Grown by Atomic Layer Deposition Using Tris(dimethylamino)silane (TDMAS) and Ozone* vol. 58, 2013.

[39] S. Ping, L. Jie, G. Shang, L. Ping, W. Xiao, S. L. Wu, *et al.*, "PECVD Grown SiO2 Film Process Optimization," *Silicon Photonics Vi,* vol. 7943, 2011.

LIST OF SYMBOLS AND ABREVIATIONS

Abbreviation	Full name
AFM	…Atomic force microscopy
ALD	…Atomic layer deposition
APTES	…3-(aminopropyl)triethoxysilane
BSE	…Backscattered electrons
CCP	…Capacitively coupled plasma
CE	…Contact electrification
DRIE	…Deep reactive ion etching
DWL	…Direct write laser
EUV	…Extreme ultraviolet
FEG	…Field emission gun
GTA	…Glutaraldehyde
HMDS	…Hexamethyldisilane
ICP	…Inductively coupled plasma
M(N)EMS	…Micro-(Nano-)electromechanical systems
PBS	…Potassium-phosphate buffer solution
(PE)CVD	…(Plasma enhanced) Chemical vapor deposition
PDMS	…Polydimethylsiloxane
PP	…Polypropylene
PR	…Photoresist
PVC	…Polyvinylchloride
PVD	…Physical vapor deposition
RF	…Radio frequency
RIE	…Reactive ion etching
SE	…Secondary electrons
SEM	…Scanning electron microscopy
SPM	…Scanning probe microscopy
STM	…Scanning tunnelling microscopy
TDMAS	…Tris(dimetylamino)silane
TMAH	…Tetramethylammonium hydroxide

Symbol	Meaning	Units
ϵ_o	…Permittivity in vacuum	[$F.m^{-1}$]
γ	…Liquid surface tension	[$N.m^{-1}$]
σ_s	…Magnitude of charge per unit area	[$C.m^{-2}$]
Φ_A	…Van der Waals attraction	[J]
A_i	…Hamaker constant	[J]
F_A	…Force per unit area	[$N.m^{-2}$]
NA	…Numerical aperture	[-]
Δp	…Pressure difference (liquid surface)	[Pa]
Q	…Gas flow	[$cm^3.min^{-1}$]
R	…Resolving power (resolution)	[m]
K	…Spring constant	[$N.m^{-1}$]
θ	…Contact angle	[°]
R_f	…Roughness factor	[-]

LIST OF FIGURES

LIST OF TABLES

VYSOKÉ UČENÍ TECHNICKÉ V BRNĚ
FAKULTA ELEKTROTECHNIKY A KOMUNIKAČNÍCH TECHNOLOGIÍ

Diplomová práce

magisterský navazující studijní obor **Mikroelektronika**
Ústav mikroelektroniky

Student: Bc. Peter Fecko ***ID:*** 173643
Ročník: 2 ***Akademický rok:*** 2018/19

NÁZEV TÉMATU:

Mikrostruktury mimikující povrch tlapky gekona

POKYNY PRO VYPRACOVÁNÍ:

Navrhněte a pomocí dostupných technologií vytvořte mikrostruktury mimikující povrch tlapky gekona. Tyto mikrostruktury modifikujte pomocí vhodného crosslinkeru (SiO2-APTES/GTA) tak, aby na ně bylo možné navázat keratin. Na závěr změřte a vyhodnoťte mechanické vlastnosti vytvořených a modifikovaných mikrostruktur např. pomocí mikroskopie atomárních sil (AFM).

DOPORUČENÁ LITERATURA:

According to recommendations of supervisor

Termín zadání: 4.2.2019 ***Termín odevzdání:*** 21.5.2019

Vedoucí práce: Ing. Jan Pekárek, Ph.D.
Konzultant:

doc. Ing. Lukáš Fujcik, Ph.D.
předseda oborové rady

BRNO UNIVERSITY OF TECHNOLOGY
VYSOKÉ UČENÍ TECHNICKÉ V BRNĚ

FACULTY OF ELECTRICAL ENGINEERING AND COMMUNICATION
FAKULTA ELEKTROTECHNIKY
A KOMUNIKAČNÍCH TECHNOLOGIÍ

DEPARTMENT OF MICROELECTRONICS
ÚSTAV MIKROELEKTRONIKY

GECKO MIMICKING SURFACES
MIKROSTRUKTURY MIMIKUJÍCÍ POVRCH TLAPKY GEKONA

MASTER'S THESIS
DIPLOMOVÁ PRÁCE

AUTHOR — **Bc. Peter Fecko**
AUTOR PRÁCE

SUPERVISOR — **Ing. Jan Pekárek, Ph.D.**
VEDOUCÍ PRÁCE

BRNO 2019

VYSOKÉ UČENÍ TECHNICKÉ V BRNĚ
FAKULTA ELEKTROTECHNIKY A KOMUNIKAČNÍCH TECHNOLOGIÍ

Diplomová práce

magisterský navazující studijní obor **Mikroelektronika**
Ústav mikroelektroniky

Student: Bc. Peter Fecko ***ID:*** 173643
Ročník: 2 ***Akademický rok:*** 2018/19

NÁZEV TÉMATU:

Mikrostruktury mimikující povrch tlapky gekona

POKYNY PRO VYPRACOVÁNÍ:

Navrhněte a pomocí dostupných technologií vytvořte mikrostruktury mimikující povrch tlapky gekona. Tyto mikrostruktury modifikujte pomocí vhodného crosslinkeru (SiO2-APTES/GTA) tak, aby na ně bylo možné navázat keratin. Na závěr změřte a vyhodnoťte mechanické vlastnosti vytvořených a modifikovaných mikrostruktur např. pomocí mikroskopie atomárních sil (AFM).

DOPORUČENÁ LITERATURA:

According to recommendations of supervisor

Termín zadání: 4.2.2019 ***Termín odevzdání:*** 21.5.2019

Vedoucí práce: Ing. Jan Pekárek, Ph.D.
Konzultant:

doc. Ing. Lukáš Fujcik, Ph.D.
předseda oborové rady

ABSTRACT

Adhesive capabilities of a gecko lizard have been the subject of many studies and an inspiration for many artificial imitations and inventions. This work proposes a design version of synthetic gecko structures in a form of micro-pillars, that would have similar adhesion capabilities as gecko setae. Structures made of Parylene C polymer have been created using photolithography and silicon etching techniques. Following focus was on various methods of surface modifications and characterisation of these structures to determine the adhesion forces on their surface, before and after modifications.

ABSTRAKT

Adhezní schopnosti gekona byly předmětem mnoha studií a inspirací pro vytvoření mnoha napodobenin. Tato práce navrhuje vlastní verzi umělých gekoních struktur ve tvaru mikroskopických pilířů, které by vykazovaly adhezní vlastnosti srovnatelné s tlapkou gekona. Vyrobeny byli struktury z polymeru Parylen C pomocí fotolitografie a technik na leptání křemíku. Dalším cílem bylo různými metodami pro modifikaci povrchu a charakterizaci vytvořených struktur, které určí adhezní síly těchto povrchů, před a po modifikacích.

KEYWORDS

gecko adhesion, adhesive setae, biomimetics, van der Waals force, reactive ion etching, XeF_2 etching, Parylene C, atomic layer deposition (ALD), adhesion promotors, scanning electron microscopy (SEM), contact angle measurement, atomic force microscopy (AFM)

KLÍČOVÁ SLOVA

adheze gekona, adhezní struktury, biomimetika, van der Waalsovy síly, leptání reaktivní plasmou, leptání v XeF_2, Parylen C, depozice atomárních vrstev (ALD), adhezní promotéry, rastrovací elektronová mikroskopie (SEM), měření kontaktního uhlu, mikroskopie atomárních sil (AFM)

BIBLIOGRAPHIC CITATION

FECKO, P. Gecko mimicking surfaces. Brno: Vysoké učení technické v Brně, Fakulta elektrotechniky a komunikačních technologií, 2019. 52 s. Vedoucí diplomové práce Ing. Jan Pekárek, Ph.D..

Prohlášení autora o původnosti díla

„Prohlašuji, že svou diplomovou práci na téma Mikrostruktury mimikující povrch tlapky gekona jsem vypracoval samostatně pod vedením vedoucího diplomové práce a s použitím odborné literatury a dalších informačních zdrojů, které jsou všechny citovány v práci a uvedeny v seznamu literatury na konci práce.
Jako autor uvedené diplomové práce dále prohlašuji, že v souvislosti s vytvořením této diplomové práce jsem neporušil autorská práva třetích osob, zejména jsem nezasáhl nedovoleným způsobem do cizích autorských práv osobnostních a jsem si plně vědom následků porušení ustanovení § 11 a následujících autorského zákona č. 121/2000 Sb., včetně možných trestněprávních důsledků vyplývajících z ustanovení části druhé, hlavy VI. díl 4 Trestního zákoníku č. 40/2009 Sb.

.

V Brně dne: 21. května 2019 ……

Peter Fecko, podpis

ACKNOWLEDGEMENT

I would like to thank my supervisor Ing. Jan Pekárek, Ph.D for an effective methodological, pedagogical and technical support during my work at this master's thesis. I would also like to thank doc. Ing. Pavel Neužil Dr., DSc. for an opportunity to work on his project.

My thanks goes to my parents, and friends, who encouraged me during my studies and writing of this thesis.

Brno ....

(author's signature)

SIX research centre
sensor, information and communication systems

Faculty of Electrical Engineering
and Communication

Brno University of Technology
Technicka 12, CZ-61600 Brno, Czechia

http://www.six.feec.vutbr.cz

Experimentální část této diplomové práce byla realizována na výzkumné infrastruktuře vybudované v rámci projektu CZ.1.05/2.1.00/03.0072
Centrum senzorických, informačních a komunikačních systémů (SIX)
operačního programu Výzkum a vývoj pro inovace.

MINISTERSTVO ŠKOLSTVÍ, MLÁDEŽE A TĚLOVÝCHOVY

EVROPSKÁ UNIE
EVROPSKÝ FOND PRO REGIONÁLNÍ ROZVOJ
INVESTICE DO VAŠÍ BUDOUCNOSTI

2007–13
OP Výzkum a vývoj pro inovace

CEITEC
Středoevropský technologický institut
BRNO | ČESKÁ REPUBLIKA

VYSOKÉ UČENÍ TECHNICKÉ V BRNĚ

„Část práce byla provedena za podpory výzkumné infrastruktury CEITEC Nano (ID LM2015041, MŠMT, 2016–2019), CEITEC Vysoké učení technické v Brně.“

MINISTERSTVO ŠKOLSTVÍ, MLÁDEŽE A TĚLOVÝCHOVY

EVROPSKÁ UNIE
EVROPSKÝ FOND PRO REGIONÁLNÍ ROZVOJ
INVESTICE DO VAŠÍ BUDOUCNOSTI

2007–13
OP Výzkum a vývoj pro inovace

TABLE OF CONTENTS

INTRODUCTION

Many centuries ago, philosophers during their studies of nature noticed how geckos are capable of climbing almost any surface. In modern studies, scientists try to understand the principals behind gecko adhesion and how does the smart adhesive, that are the toe pads of gecko, work in a micro scale. Geckos are also capable of detaching their pads in milliseconds while running on vertical and inverted surfaces.[1] Last decade there have been numerous successful attempts (at some degree) of creating surfaces inspired by this animal [2, 3], or making use of such structures as a form of dry adhesives [4-6], that in the future could effectively replace traditional (wet) adhesives, which are used today.

Past studies propose, that the adhesion forces, which play a role in clinging ability of the Tokay Gecko (*Gekko Gecko)* animal, are due to capillary forces or van der Waals forces. These are conventionally considered as main sources of adhesion. But a recent study suggests, that fine fibrillar features of gecko toes exchange significant numbers of electric charges with the contacted substrate via the contact electrification (CE) phenomenon. They demonstrate, that the contribution of CE effectively dictates the strength of gecko adhesion [7]. However, this work does not argue, which forces of adhesion (van der Waals, capillary or those caused by CE) are prevalent, but only deals with creating gecko mimicking structures and their characterization using available analytical tools. Regardless, all three types of forces will be discussed in the following chapter.

The main aim of the first chapter is also to clarify forms of surface adhesion of some animals and insects, and the microscopic texture of gecko feet specifically. Secondly, three main ideas of factors, which play some role in adhesion forces of the surface contact are explored.

The second chapter discusses technological and analytical options that are utilized in fabrication of the design inspired by gecko features. The whole process is very similar to the micro-electro-mechanical systems (MEMS) fabrication processes, therefore materials, such as silicon (wafers) are used, lithography techniques are studied, ways of etching the substrates and deposition of other useful materials and surface adhesion modification methods are described. The chapter is concluded by which imaging and measurement techniques were used for sample characterisation.

Third chapter explains specific steps of fabrication using tools described in previous chapter. It starts with the proposed topology of gecko mimetics and a step-by-step production of samples with measurable structures. Also, the results are shown on form of magnified images of the microscopic structures.

The last chapter deals with measuring adhesion properties of the created structures using contact angle method and atomic force microscopy (AFM). The results are discussed in the ending chapter.

1 ADHESION PROPERTIES OF GECKO SETAE

Besides the tokay gecko, many other species of animals evolved forms of adhesive organs on their foot in order to effectively adhere to surfaces present in their environment, like trees or other plants. These organs usually form small pads and based on their functionality, they come in two designs as 1) pads with relatively smooth surface and 2) pads covered with micron or sub-micron sized setae (hairs) of high density per pad. [8]

1.1 Advantages of "hairy" pad design

1) Rough surface compatibility

There is no practical difference of hairy adhesive surfaces and those made of solids on a smooth surface. But when the roughness of the surface starts increasing, the effective contact area between the adherents decreases and a smooth solid pad has trouble adhering to the topology of the surface if it is not made of soft material (which has low elastic modulus – material's resistance to elastic deformation). But these soft materials are more susceptible to creep, degradation (wear) and contamination. By bending and stretching of setae, the hairy pads behave as these soft solids (their apparent elastic modulus is low) even though they are made of relatively hard materials. The advantage of the micro- or nanoscale sized tips is also, that they easily adapt to the topography of rough surface of a hard material on a microscale and form an intimate surface contact, which increases adhesion and frictional forces (see fig. 1-1). [8]

2) Self-cleaning properties

Geckos keep their feet clean without any active grooming. The morphology of a hairy pad may be less contaminated with small particles, because of greater adhesion of these particles to the surface, than to the very fine tips of gecko spatula. So, the gecko setae are cleaned with every step the animal takes. [8]

3) Effortless and controllable detachment

Gecko setae were observed to generate large detachment forces by only being slightly pulled in proximal direction with a small preload by the animal. The adhesion forces decreased after the angle between setae and the surface exceeded the critical value of 30° and could be easily detached. This can help animals to quickly switch between attachment and detachment by making gross limb movements. [8]

4) Maximised adhesion

It has been confirmed, that even on a smooth substrate, a hairy pad morphology may maximise adhesion, despite the smaller contact area. [8]

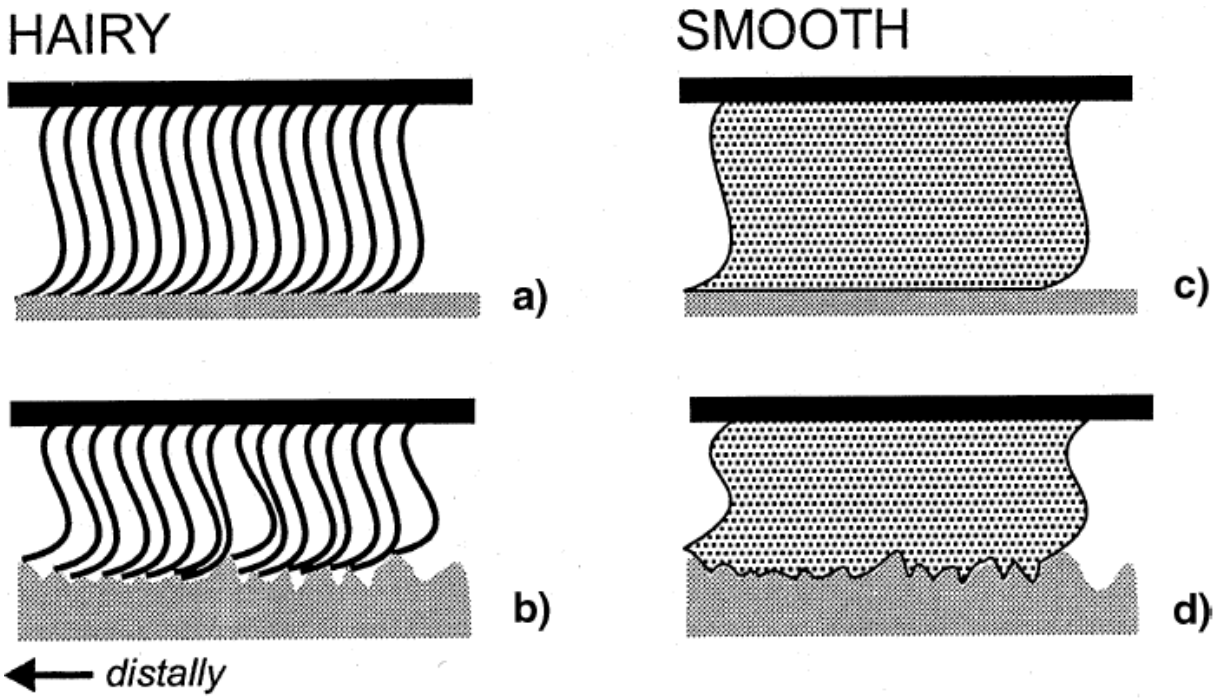

Fig. 1-1. Functionality difference between (a, b) "hairy" and (c, d) "smooth" pad designs on (a, c) smooth and (b, d) rough surface profile. [9]

1.2 Gecko toe pads

Gecko's extraordinary ability to stick to most of the surfaces is thanks to uniform microarrays of hair like setae formed from β-keratin of which his toes are covered in series of lamellae. Each seta branches to form a nanoarray of hundreds of spatula structures, that can essentially make ultimate contact with the surface. [1]

The gecko setae: (1) are directional, (2) attach strongly with minimal preload (pushing force), (3) detach quickly and with minimal effort, (4) stick to nearly every material, (5) exhibit rate-dependent adhesion, (6) do not stay dirty or (7) self-adhere, and by default (8) are non-sticky. [1]

A single seta of the tokay gecko is approximately 110 μm in length and 4,2 μm in diameter, they are also uniformly distributed on lamellae. Setae branch a number of times at the tips into 100-1000 terminal structures known as spatulae. These are approximately 0,2 μm long with a similar width at the tip. All is shown on fig. 1-2. [1]

It was estimated, that two front feet of Gecko can withstand ~20 N of force parallel to the surface across 227 mm^2 of toe-pad area. Individual setae have proved both less sticky and much more sticky than predicted by whole-animal measurements under varying experimental conditions, implying that attachment and detachment in gecko setae are mechanically controlled. [1]

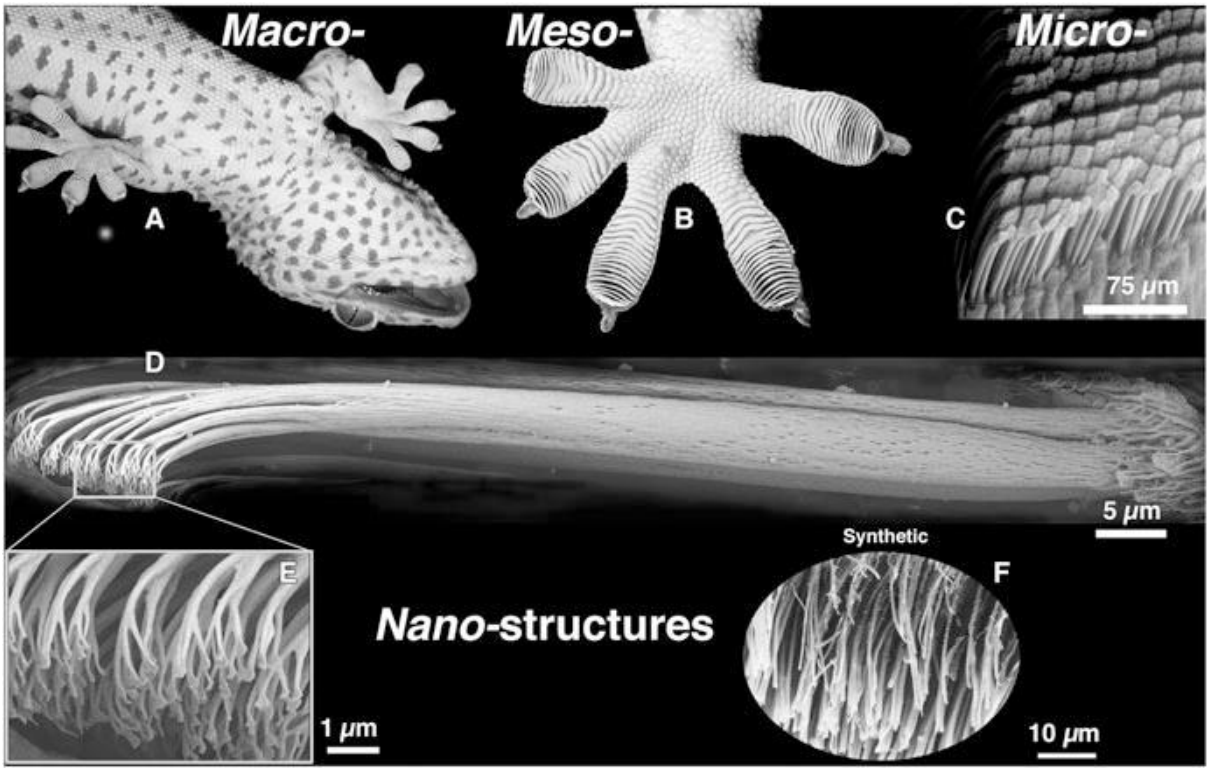

Fig. 1-2 Structural hierarchy of the gecko adhesive system. (a) Gecko climbing a vertical surface; (b) view on the foot of the tokay gecko (adhesive lamellae visible); (c) setae arranged in a grid like pattern; (d) detail on an individual gecko seta; (e) close-up on a nanoscale array of hundreds of spatula tips of a single seta; (f) synthetic spatulae fabricated from polyimide using nanomolding. [1]

1.3 Effective forces

The beliefs about what primarily causes adhesion of gecko setae vary among researchers. There is no clear consensus, but three main forces are believed to have some level of impact on the overall adhesion: (1) van der Waals forces, (2) capillary forces, and (3) electrostatic forces. But the question about which from these factors is dominant is still a subject of today's research.

1.3.1 Van Der Waals force

This force is weak and becomes significant only at a very short distance. If we take very small particles (<1 μm), this attraction force whereas the influence of gravity becomes negligible. Taking two nanoparticles of same radii, that are separated by a distance *S* the simplified expression of van der Waals attraction is:

$$\Phi_{\mathrm{A}} = -\frac{A_{\mathrm{i}} \cdot r}{12 \cdot S}, \tag{1}$$

where the negative sign represents the attraction nature of the interaction, the r is the radius of one sphere, and the A_{i} is a Hamaker constant (magnitude on the order of 10^{-19} to 10^{-20} J). [10]

Table 1-1: Hamaker constants of some common materials. [10]

Materials	Metals	Gold	Oxides	Al_2O_3
A_i [10^{-20} J]	16,2-45,5	45,3	10,5-15,5	15,4
Materials	SiO_2 (fused)	SiO_2 (quartz)	Polymers	Water
A_i [10^{-20} J]	6,5	8,8	6,15-6,6	4,35

Table 1-2: Variations of equation (1) depending on different assumptions about two particles. [10]

Particles	Φ_A	
Two spheres of unequal radii, r_1 and r_2 (r_1, r_2 >> S)	$-\frac{A \cdot r_1 \cdot r_2}{6 \cdot S \cdot (r_1 + r_2)}$,	[J]
Two parallel plates with thickness of δ	$\frac{-A}{12 \cdot \pi} \cdot \left(\frac{1}{S^2} + \frac{1}{(2\delta + S)^2} + \frac{1}{(\delta + S)^2}\right)$,	[J/m²]
Two blocks	$\frac{-A \cdot r}{12 \cdot S}$,	[J/m²]

1.3.2 Capillary forces

At microscale, the Young-Laplace equation is used to define the equilibrium of liquid surface (e.g., capillary surface) [11]:

$$\Delta p = \gamma \left(\frac{1}{R_1} + \frac{1}{R_2}\right) \quad , \tag{2}$$

where γ is the liquid surface tension (liquid-air surface), Δp is the pressure difference across the liquid surface, and R_1, R_2 are the principal radii of surface curvature. In a narrow tube (with radius a), the liquid surface will be a portion of spherical surface (with radius R). The relation between R and a is a cosine function of the liquid-solid contact angle Θ ($\cos \Theta = a.R^{-1}$). Thus, the equation (2) can be modified as [11]:

$$\Delta p = \frac{2\gamma \cdot \cos\theta}{a} \quad . \tag{3}$$

The surface tension represents the potential energy change caused by per unit liquid surface area change, which is typically considered to be a constant, e.g., the γ of water is measured as 72 $mN.m^{-1}$ at room temperature. It is also reported that the surface tension of water decreases with the temperature, and slightly increases with the electrolyte ion concentration. Currently, the Young-Laplace equation is also widely used to describe the capillary pressure when the channel/pore size is down to nanoscale. [11]

1.3.3 Contact electrification

A spontaneous charge transfer between materials in contact can increase adhesion between them. To better describe this situation, two smooth dissimilar insulating materials, e.g. mica and fused silica (both have near atomic smoothness) are brought into contact and separated, while the charge transferred during contact and of the resulting electrostatic force, respectively, are directly measured by two electrometers. To determine the sign and quantity of charge on the front surfaces (those in contact), electrical contacts are coated with silver (see fig. 1-3). [12]

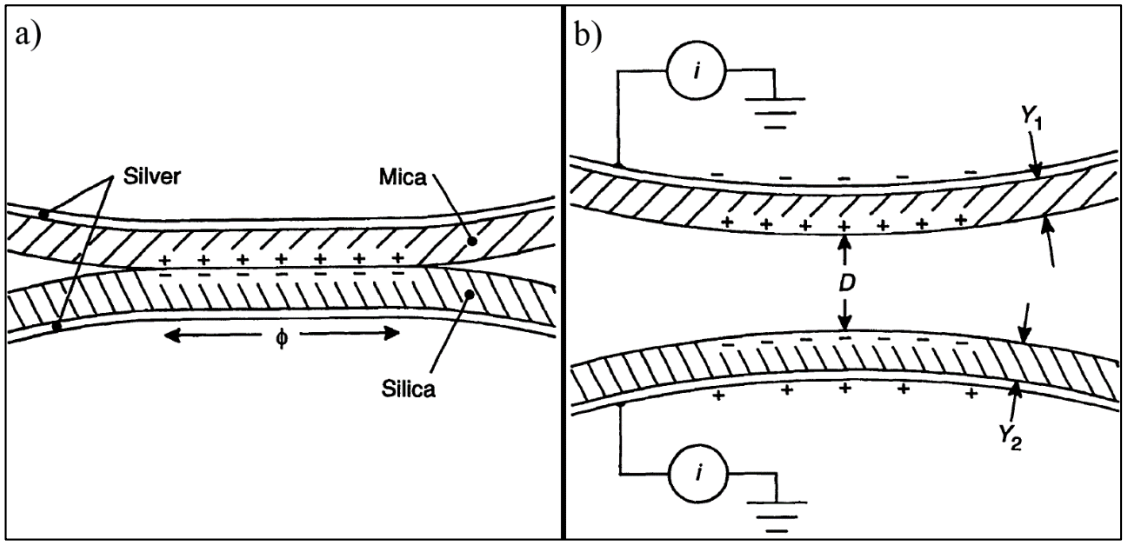

Fig. 1-3 Schematic arrangement of thin solid film (a) in contact (of size ϕ); (b) upon separation. [12]

In calculating the force, one must consider four layers of charge: the two front surfaces plus two grounded silver electrodes a few micrometres behind them. The field across the gap decreases even with constant charge on the front surfaces. the force per unit area at surface separation D is given by

$$F_{\mathrm{A}} = -\frac{\sigma_{\mathrm{s}}^2}{2\epsilon_{\mathrm{o}}}\left(\frac{B}{B+D}\right)^2 \tag{4}$$

where σ_s is the magnitude of charge per unit area, ϵ_o is the permittivity of vacuum and $B = Y_1/K_1 + Y_2/K_2$, with Y_1, Y_2 and K_1, K_2, *a*s the thicknesses and relative dielectric constants of the two substrates.[12]

The analysis of the distance dependence of electrostatic force is possible if certain simplifying assumptions are made: (1) surface deformation is ignored (in reality, the electrostatic attraction is strong enough to deform materials elastically), (2) the two surfaces are modelled as infinite parallel plates ($D << \phi$), and (3) the charge density of the plates is assumed to be uniform and equal to the total charge divided by the maximum contact area. [12]

2 FABRICATION AND ANALYTICAL TECHNIQUES

2.1 Lithography

To implement the fine design proportions from previous chapter onto a silicon wafer substrate a set of very accurate lithography methods are required. This includes making a mask with the design imprint (positive or negative), then transferring the design onto an appropriate substrate, e.g. coated with a photoresist film that will be later developed.

With some lithography techniques it is possible to implement a desired image onto the substrate directly and with precision in nanoscale (nanolithography). But this approach is very time consuming and usually unnecessary. A better approach is to transfer the image with high precision and accuracy onto a glass mask carrying a durable and thin metallic film. This mask carrier can be then used repeatedly on sample substrates using faster lithographic methods while a high level of precision is preserved.

2.1.1 Photolithography

Fig. 2-1 shows basic steps of photolithography process, consisting of using the mask carrier to transfer a desired image onto a photosensitive film (photoresist - PR). The areas exposed to light with a certain level of energy (wavelength and dosage) change their chemical properties. The exposed material can be rendered more soluble in some developing solvent (developer), thereby producing a positive image of the mask (the photosensitive material is then called a positive PR) or in case it is less soluble in the developing solvent, it produces a negative tone image of the mask (negative PR). Conventional photolithography is capable of fabricating features of 200 nm and above. [10]

The minimum size of individual elements, or in other words, the maximum resolution of photolithography is limited by diffraction. The diffraction is a result of light being projected into places of geometrical shadow under the carrier mask. The uniformity of exposure close to the edges is compromised, and the developed line edges of the resulting pattern become blurred or diffused at the resist surface. This effect can be partially reduced by bringing the carrier mask in contact with the PR surface. Proximity can be enhanced by creating vacuum in-between (uniformity and cleanliness of the PR surface is very critical). [10]

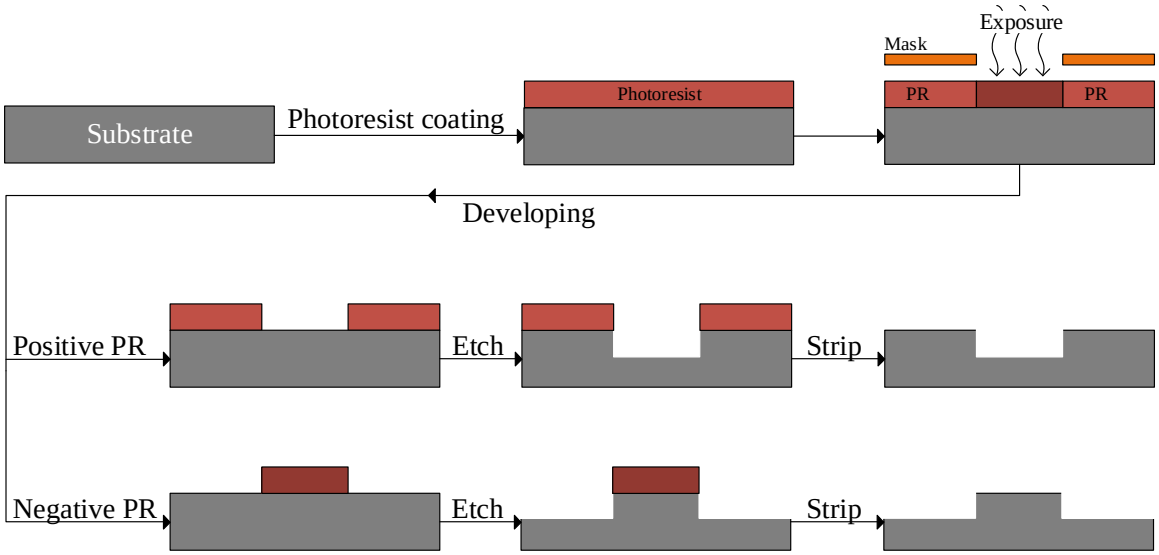

Fig. 2-1 Basic scheme of the photolithographic process steps – transferring images onto a surface using a mask.

Higher resolutions can be obtained using light with shorter wavelengths and lens systems with large numerical apertures, one can obtain. Deep Ultra-Violet lithography (DUV) based on exposure at wavelengths below 300 nm allows one to obtain patterns with a minimal size of ~100 nm. For this, mercury arc lamps and excimer lasers (higher resolutions) are used. Excimer lasers are gas-based light systems filled with inert and halide gases (Kr, Ar, Xe, F and Cl). Examples of excimer lasers are: KrCl and KrF (wavelengths 222 and 249 nm), ArF (193 nm) and F_2 (157 nm). Extreme UV (EUV) lithography with wavelengths of 11-13 nm has also been explored for fabricating features with even smaller dimensions of 70 nm and below. [10]

2.2 Etching of silicon and silicon dioxide

Creating structures in micro and nanoscale (e.g. MEMS, NEMS) might require a high level of etching process controllability and material versatility. Generally, we have two basic options to etch a wide range of materials: wet and dry etching. Wet etching usually requires chemical solutions and buffered etchants in liquid forms. Dry etching is done with energized plasma – gas ionized using radio frequency (RF) power sources.

Some advantages of dry etching over wet etching:

- The biggest difference is directional (anisotropic) nature of plasma technology, while wet etching is very isotropic (etching in all directions).
- Another desirable trait of plasma process is, that they are easily controllable through RF power, pressure, time, and gas selection.
- Less sensitive to atmospheric changes such as temperature, humidity, and pressure.
- Plasma etching leaves no residues and consumes less raw materials than wet etching.
- Waste product are mostly gaseous and are liberated directly into atmosphere. Most of the gases are nontoxic, but some might be very hazardous (e.g. SF_6 is a greenhouse gas). The processes don't require extensive safety trainings and are easily programmable.
- A photoresist can be used as a mask for etching patterns into hard materials. [13]

For the purposes of this work, the dry etching techniques are most suitable. The idea is to etch deep into silicon substrate using the SiO_2 and PR as masks patterned with dots. The result would be deep holes with smooth walls serving as a form for long nano-pillars mimicking Gecko spatula. Therefore, a high aspect ratio and high anisotropy is needed, those are the requirements, which wet etching doesn't meet.

2.2.1 Reactive ion etching – RIE

Reactive ion etching (RIE) is a plasma process where using RF discharge creates excited species (ions and radicals) in low vacuum. RIE etching utilizes etching of chemically active species and also physical ion bombardment of the surface. Ion bombardment is directional thanks to electrical field present, so the etching is highly anisotropic, with reduced lateral etch rate and vertical (or nearly vertical) sidewalls. It is used where narrow lines or channels or structures with high aspect ratio need to be fabricated. RIE of silicon is independent of crystal planes, and therefore any shape can be fabricated, unlike anisotropic wet etching. Deep reactive ion etching (DRIE) is an extension of RIE that enables high-rate etching of deep structures. [14]

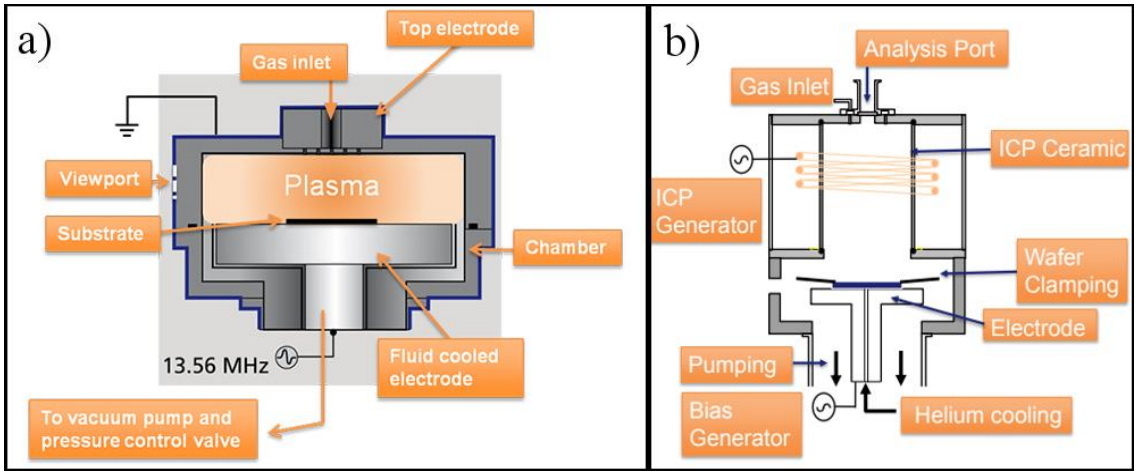

Fig. 2-2 Description of (a) capacitively coupled plasma (CCP) and (b) Inductively coupled plasma (ICP) sources. [14]

Reactive Ion Etching equipment can be made of two different power source types: capacitively coupled plasma (CCP) (fig. 2-2a) or inductively coupled plasma (ICP) (fig. 2-2b). RIE processes are usually carried out using CCP power source, where a discharge of plasma occurs between two capacitive electrodes. The bottom electrode is also a substrate chuck, so the substrates are directly exposed to plasma particles, which can be a disadvantage (decreased anisotropy). Also, the chamber needs to be pumped into high vacuum after every process and that takes time. [14]

ICP power source is found in DRIE processes. Inductively coupled plasma is ignited high above the substrate table. Because of that, this plasma equipment also requires CCP electrodes to create voltage bias for extracting and accelerating ions from ICP onto the surface of the wafer. [14] The wafer is held with a clamp against the bottom electrode, which also provides cooling for the wafer, using helium gas as a mediator. These machines usually come with a load-lock, which is pumped independently from the plasma chamber, so that it can be under high vacuum constantly. [15]

Typical highlights of (D)RIE processes:

- **Etch rate** of silicon varies from 0,1-1 μm for RIE and in DRIE it can reach rates of 10-50 μm, but it depends on actual process parameters and the HW configuration.
- **Selectivity** (etch rates of mask:etched material) – during Si etching, polymeric, metallic or silicon oxide/nitride masks can be utilised. The selectivity varies with used masks but can be from 1:1 to 10:1 for RIE and 10:1 up to 100:1.
- **Anisotropy –** determined from direction of the accelerated ions and radicals, and is better in DRIE
- **Aspect ratio** (depth:width) in RIE are limited to around 2:1 and for DRIE it can rise up to 20:1 (achieved by Bosch technique)

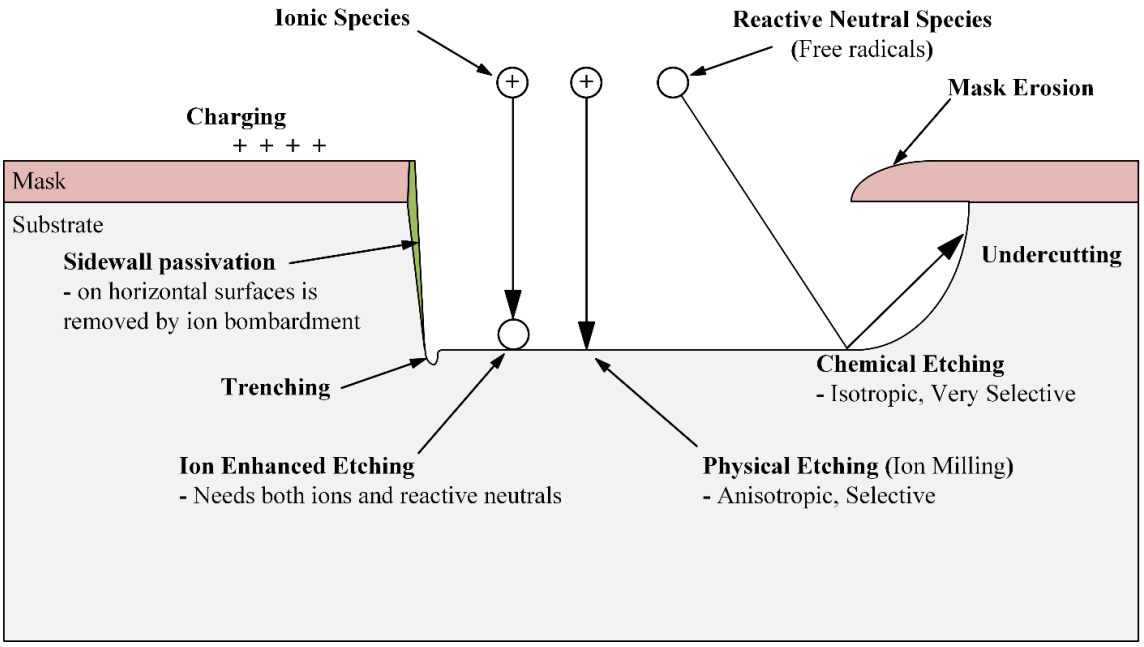

Fig. 2-3 Summary of some of the phenomena occurring during reactive ion etching.

The number of controlled parameters is an advantage, but on the other hand, it makes this process the most critical fabrication step for this work. The complexity of process dependencies during reactive plasma etching are summarized in fig. 2-3.

Materials and etching gases

Among all the materials, that could be etched with RIE, the most frequently etched are silicon, silicon dioxide/nitride, and some refractory metals (aluminium, tungsten, etc.). Silicon and its compounds can be etched in chlorine and fluorine (SF_6) plasmas, but because the chlorine gas is hazardous, it's less popular. Silicon nitride (Si_3N_4) is etched in CF_4- or SF_6- based plasmas. It is not possible to achieve selectivity nitride-silicon in fluorine plasmas, but using plasmas based on CHF_3, C_2F_6, or C_4F_8 it is possible to obtain nitride-silicon selectivities from 5:1 to 50:1. SiO_2 etching can be done using the same plasmas. [14]

As far as masks are concerned, the easiest and fastest way is to use a photoresist mask, since it is broadly used in many technological processes. The downsides of using polymeric PR are little selectivity and thermal sensitivity. In RIE plasmas the temperatures can easily range from -150°C to +450°C. Very low temperatures cause PR to form cracks and high temperatures, caused by ion bombardment, will burn the PR. Other options are "hard masks" like SiO_2 for its relatively high SiO_2-Si selectivity and metallic masks but coating them onto Si can create impurities and tension in the Si crystal. [14]

2.2.2 Deep reactive ion etching (DRIE)

The most useful and most critical process step of Gecko fabrication is etching deep holes relative to the diameter of the dot. That is why high aspect ratio is needed, and good anisotropy for perpendicular "deep drilling". Other important variables are etching rate, how big is the undercut and how smooth are the walls. Two popular DRIE techniques fulfil these requirements to some extent: Bosch process and Cryogenic process.

Bosch process

Bosch process was developed and patented by Franz Lärmer and Andrea Schilp in year 1994. On fig. 2-4 is shown a simple method for "deep drilling" called also the "switched process" and "time domain multiplexed process" It works by alternating etching steps with Si etchant gas (SF_6), that produces fluorine radicals and passivation steps, when fluorocarbon film is deposited, forming polymeric chains (c-C_4F_8). The SF_6 step is not fully anisotropic, but with the passivation layer on the sidewalls, horizontal surfaces are primarily etched due to ion bombardment. When these steps are cycled several times, it results in deep vertical sidewalls. But, as seen on the picture, the microscopic cross section shows scalloping, because of the pulsed nature of the process. [14, 15]

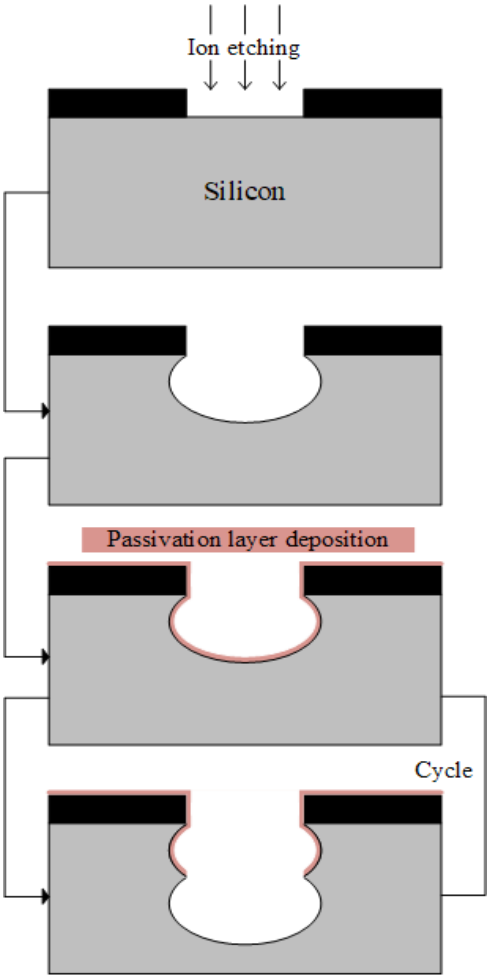

Fig. 2-4 Bosch process etching steps. The last two steps, polymer deposition and etching, are cycled until the desired depth is achieved.

The etch and passivation times are usually from 5-15 s, and changing this step durations and ratio, one can easily control the profile character, like etch rate, selectivity, profile angle and scalloping. [15]

Cryogenic process

Cryogenic RIE etching was first introduced in1988 by Tachi, Kazunori, and Okudaria. By cooling the wafer during RIE the chemical etching is reduced, improving anisotropy and sidewall smoothness. Additionally, selectivity between the mask and the etched material is increased. The reason for little chemical reactions is silicon oxyfluoride (SiO_xF_y), which inhibits lateral etching, so it can proceed downwards with accelerated ions removing the passivation layers on the bottom. Controlling the etch rate is done by changing the high concentrations of fluorine radicals in SF_6/O_2 plasma where O_2 controls the quality of passivating layer. Too much oxygen results in over-passivation and formation of so-called black silicon (silicon micro-grass). [14]

2.2.3 XeF_2 etching of Silicone

Another way of dry etching Si is in XeF_2 gas (plasma-less) – vapor-phase etch. It is completely isotropic and the etch rates are about a few microns per minute divided in several cycles of gas inflow and pumping. It's highly popular in MEMS technologies (releasing AlN/ZnO resonators, micro-mirrors, cantilevers, etc.), microfluidics (fig. 2-5), etc.

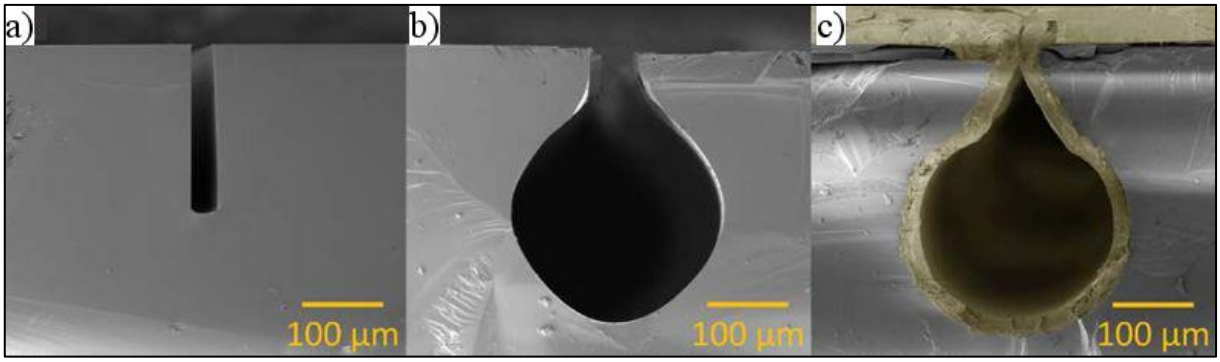

Fig. 2-5 Example of using XeF_2 gas on the (a) bottom of a silicon trench to etch (b) a buried microfluidic channel which could then be (c) closed with a polymer (Parylene C). [16]

The typical etch rates of Si 6" wafer for surface micromachining applications are 2 to 3 µm.min^{-1}. For small chips up to 10 µm.min^{-1} and fully exposed 6" wafer etches at 0.2 µm.min^{-1} rate.

Completely resistant to XeF_2 etch are some metals (Al, Ni, Cr, Pt, Ga), compounds (PZT, MgO, ZnO, AlN, GaAs), polymers and organics (PR, PDMS, C_4F_8, silica glass, PVC, PP, …etc.). [17]

Etching can occur during two types of processes:

1. pulsed flow – higher efficiency and accurate mixing of XeF_2 with other gases,
2. continuous flow – easier to achieve high uniformity, more distinct control of the etch depth and easier end point detection (reaching the desired etch magnitude). [17]

Table 2-1: Etch selectivity of some materials to silicon in XeF_2 vapor-etching. [17]

Material	Mo	Ge	SiGe	SiO_2	Si_3N_4	Au	Cu
Selectivity to Si	2:1	(*)	(*)	1000:1	>1000:1	(+)	(+)
Material	**SiC**	**Ti**	**TiN**	**Ta**	**TaN**	**W**	**TiW**
Selectivity to Si	(+)	(*X*)	(*X*)	(*X*)	(*X*)	(*X*)	(*X*)

(*) - same or greater than Si; (+) – low amount of attack under certain conditions;
(*X*) – etch rate (0 to 300 Å.min^{-1}) depends on temperature

2.3 Parylene vapor deposition polymerization

Parylene is the trade name for compounds known as poly-para-xylylenes. Their resulting polymer species are formed in a process of pyrolysis in vacuum, which is best imagined as direct condensation from gaseous phase onto the substrate. During the deposition cycle, the gas vapours don't pass through intermediate liquid phase, so the thickness is very uniform over all deposited surfaces. There are three primary variations of Parylene: C, N and D. [18]

- **Parylene N** is the basic compound of poly-P-xylylene, it is completely linear and a highly crystalline material. Its molecules are extremely elastic, which causes them to "bounce" over the surface several times before depositing. That renders this species capable of penetrating small openings in the substrate better than other variants. The deposition pressure during heating and deposition time are higher than in Parylene C or D.
- **Parylene C** is commercially more available and it's the same monomeric compound, but with substituted aromatic hydrogens with chlorine atom. This type is most popular due to high dielectric strength, cost and process advantages, such as higher deposition rate and good pressure control.
- **Parylene D** is also commercially available and from original monomeric structure it has two hydrogen atoms substituted by chlorine. It's not very elastic, so the polymer will deposit shortly after entering the deposition chamber. The pressure rise during the deposition process is quite low. [18]

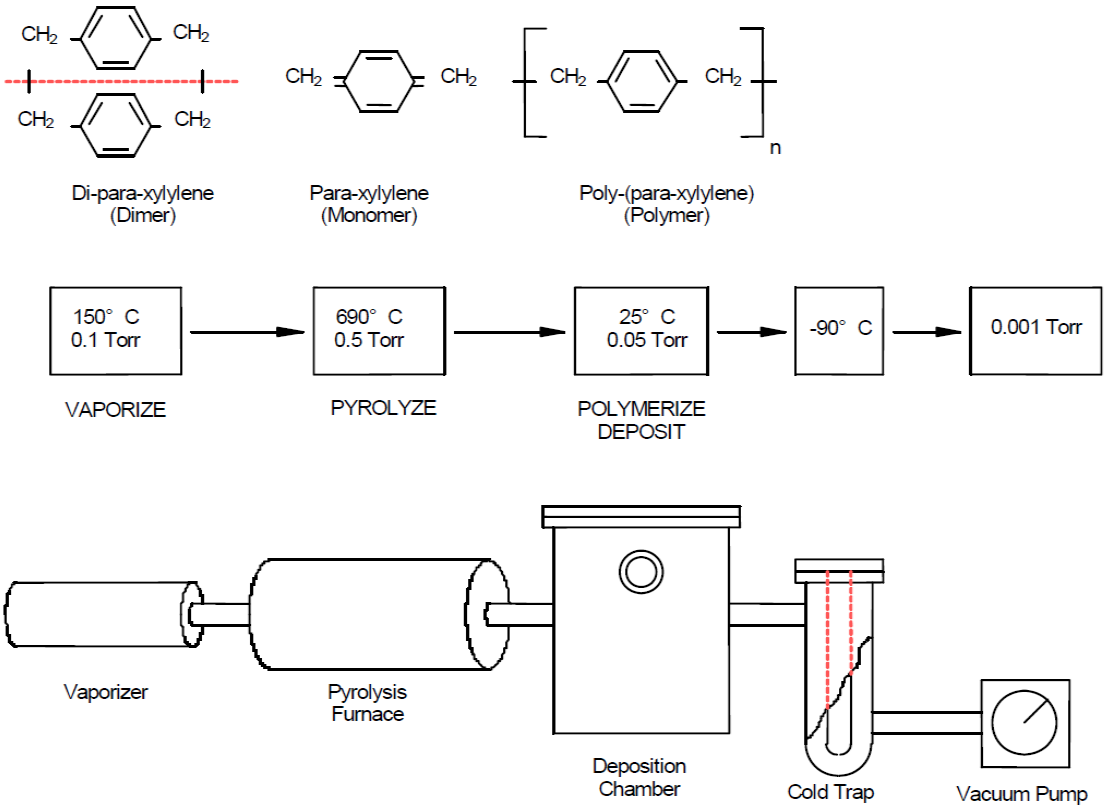

Fig. 2-6 Typical deposition system block diagram of main process components. [18]

The polymerization process occurs at pressures around 1,5 Pa and the polymers are formed at room temperatures. As seen on fig. 2-6, the process starts in a vaporizer tube, where the Parylene is vaporized from its solid dimer form and sublimates into gaseous phase. The gases travel through a furnace where high temperatures pyrolysis happens (breaking of dimer into monomer form). When the deposition chamber is at room temperature, the monomers polymerize uniformly on every surface inside the vacuum chamber. The cold trap stops the gases from entering the vacuum pump.

2.3.1 Bonding with Parylene

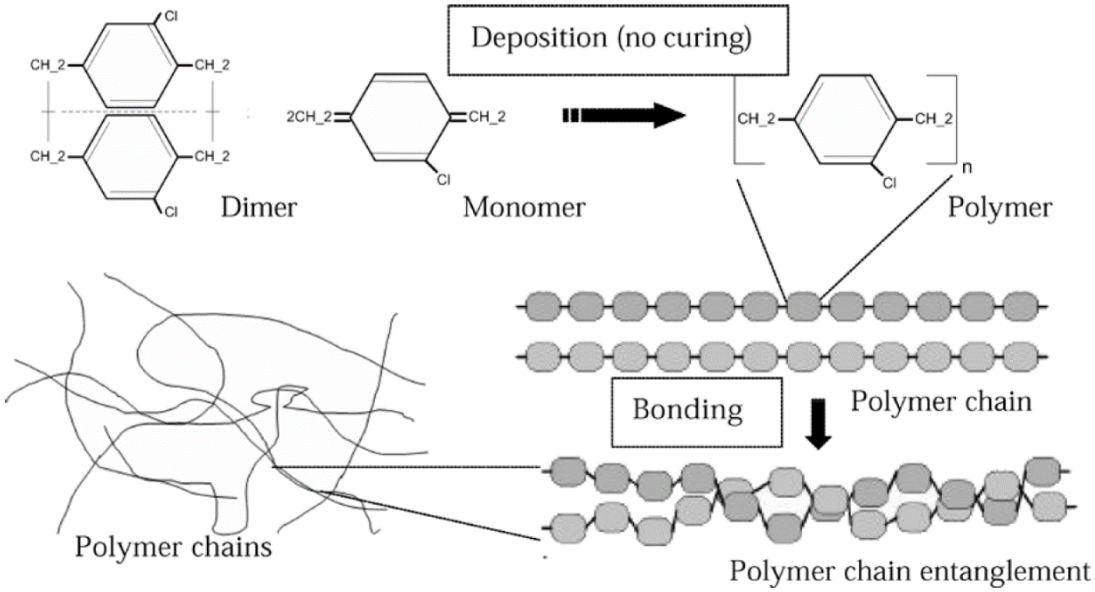

Fig. 2-7 Hypothetical Parylene chain entanglements. [19]

Some applications, mostly three-dimensional MEMS devices, sometimes require stacking wafers and bonding them together. Microfluidic chips, which have utilized Parylene polymers for micro-channel fabrication, also might require fluid-proof sealed cavities. Bonding techniques are generally performed under low or elevated temperatures. For those applications, where polymers are used, the high temperature bonding (eutectic, anodic and fusion bonding techniques) is out of the question, because polymer structures usually melt, soften or burn at or above 300°C. Bonding at low temperatures uses adhesive polymer materials, or solders, which are carried out at temperatures below 300°C. [19]

A Parylene film, when heated, does not undergo any chemical reactions, except for the glass transition temperature at 109 °C and the melting temperature at 303 °C. In this temperature range, a physical entanglement of Parylene film polymeric chains might occur, thus, making Parylene bondable to itself. [19]

2.4 Adhesion promotion of polymeric and silicon surfaces

In many fields, there is a need for connecting two materials of same, but often very different properties. In metals, and other amorphous materials, welding and soldering, or generally using high temperatures, can give a desired result. In plastics, low temperatures are more suitable, but even better are creating connections at temperatures below 50 °C, which does not cause so much degradation, that is very common in many polymeric materials. That may involve options, such as ultrasound soldering or using a excited gas – plasma. Plasma treatment can create chemically functional groups and radicals, which activates the surface. [20] This may allow connecting two same or different materials, like metals and plastics using chemical bonds. Another option is silanization of incompatible material surfaces for covalent binding. [21]

2.4.1 Surface activation by O_2 plasma

One method of plasma surface activation is with a noble gas, for example argon (Ar). When the Ar is ionized in an electric field, it stops being electrically neutral and tries to return to the neutral state by catching an electron. If it hits the surface of the treated material, it reacts with high energy, that is strong enough to remove an electron and leave an open bond on the surface or crack the bond of a polymer (see fig. 2-8a). The downside of using Ar is, that the naked bonds recombine too quickly. [20]

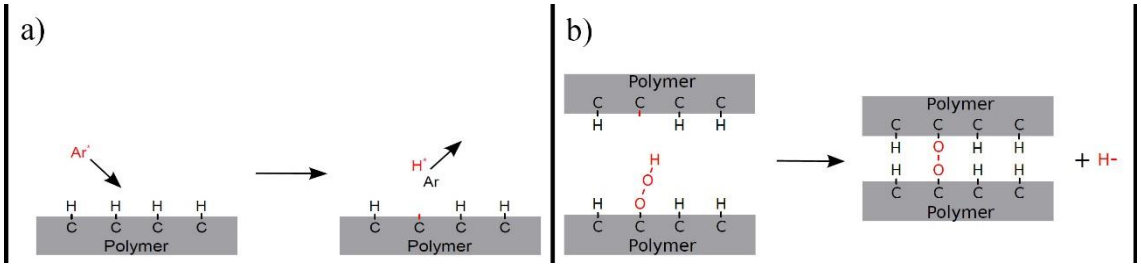

Fig. 2-8 (a) Effects of argon ion on polymer; (b) Theoretical reaction of two oxygen activated polymer surfaces. [20]

Using a reactive gas, such as oxygen (O_2), the surface can be activated by creating functional hydroxyl groups (OH groups). These groups are able to react with another chemical groups of the second material and create covalent bonds. But the resulting O-O (peroxide) bond shown in fig. 2-8b is not permanent, and an adhesion promoter is therefore needed as an intermediate layer. Such molecule can create a permanent connection between these two materials. The adhesion promoter can be applied directly by plasma and then the elastomers are melded together or, as shown on fig. 2-9, the surface activated by plasma is applied with the promoter and melded with the other polymer with an amino group, that can react with hydroxyl group of the adhesion promoter. This example shows, that the chemistry of both materials has to be known. [20]

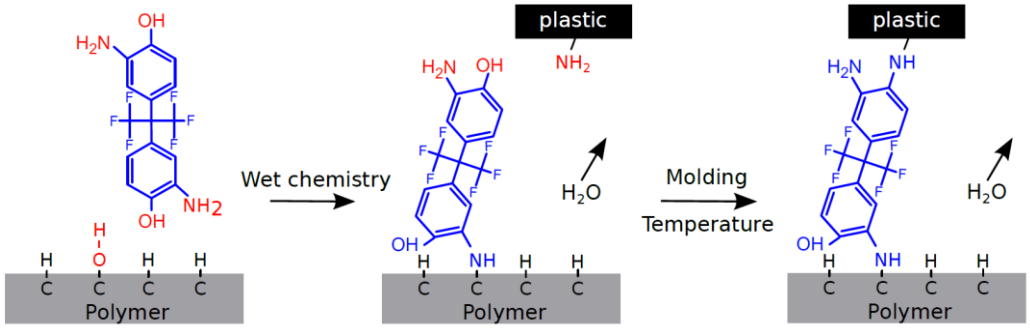

Fig. 2-9 Example of an adhesion promoter creating a connection between two polymers (one surface is plasma-activated). [20]

2.4.2 Silane adhesion promoters

As stated in previous chapter, two dissimilar materials can adhere to each other with an adhesion promoter, or a coupling agent, that is put between them. It will act at the organic-inorganic interface to chemically and physically connect them with a strong cohesive bond. In some cases, plasma enhancement is required before applying the coupling agent.

These promoters are chemical materials that contain dual functionality in their molecular structure. Its inorganic reactivity is given to by a metallic central atom (e.g. Si, Zr, Ti, Al…), especially if methoxy, ethoxy or hydroxyl groups are attached to the metal atom. As for organic reactivity of the adhesion promoter, an organofunctional group can be attached to the metal through an alkylene, arylene, or other type of organic bridge. [22]

A silicon-based chemical, that acts as a coupling agent, has a general structure of four substituents attached to a single silicon atom. The most common structure has three inorganic – reactive alkoxy groups, methoxy or ethoxy, and one organic group (sometimes it may have one of the alkoxy groups replaced by a methyl group). These coupling agents will act in the area between an inorganic and an organic substrate and create a bond or a bridge to improve adhesion between the two dissimilar materials (see fig. 2-10). [22]

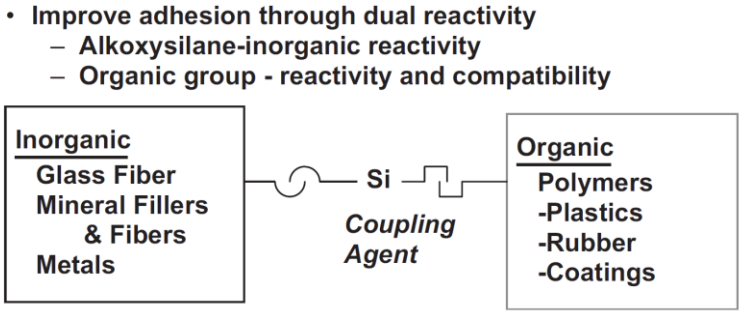

Fig. 2-10 Dual reactivity of a silane-coupling agents. [22]

2.5 Atomic layer deposition ALD

ALD is a vapor phase technique capable of producing thin films of variety of materials. It had demonstrated potential advantages over alternative deposition methods, such as chemical vapor deposition (CVD) and various physical vapor depositions (PVD) techniques, due to its conformality and control over materials thickness and composition.

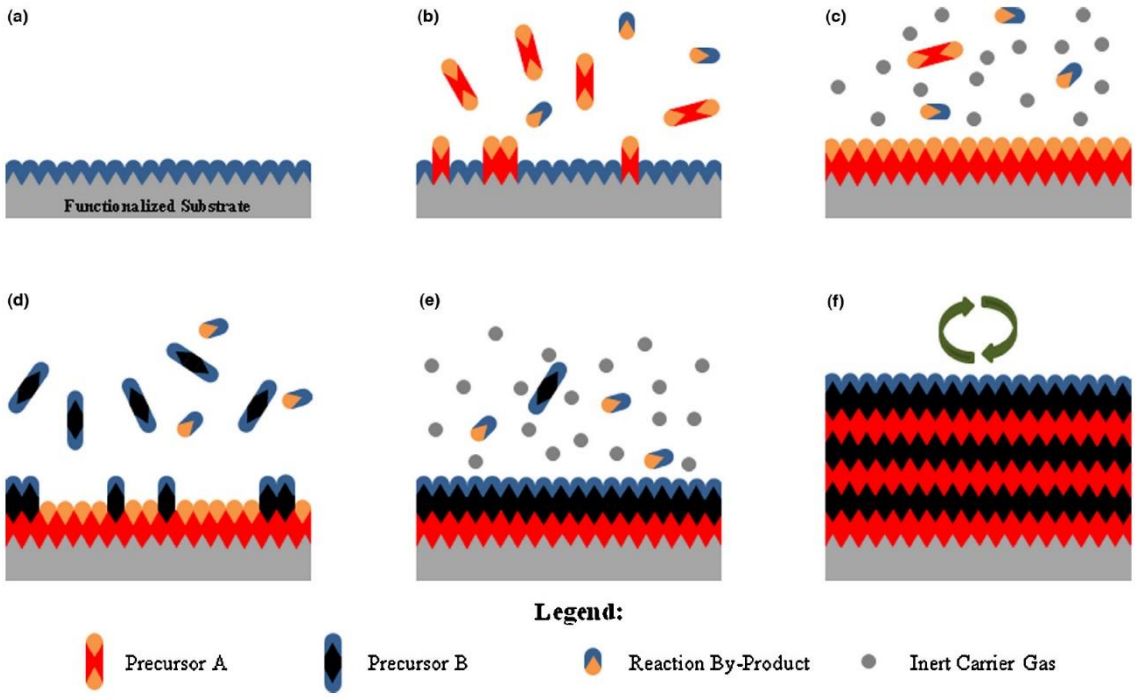

Fig. 2-11 Schematic of ALD process: (a) Substrate with natural or treated functionalization. (b) Pulse of precursor A and his reaction. (c) Purge of excess products by inert carrier gas. (d) Precursor B is pulsed and reacts. (e) Another purge by inert gas. (f) Previous steps are repeated until desired thickness is achieved. [23]

The process itself consists of sequentially alternating pulses of chemical precursors, which react with the surface (see fig. 2-11). One pulse of reactive precursor, called half-reaction, leaves no more than one monolayer at the surface. The half-reaction leaves some unreacted precursors and by-products which are purged with an inert carrier gas (typically it's N_2 or Ar). This is then followed by a counter-reactant precursor pulse and purge. That leaves a layer of the desired material and the surface is prepared for another cycles of precursor pulses and purges until the appropriate film thickness is achieved. Since those created monolayers are basically molecules, the growth of the film is usually less than 1 Å per cycle, depending on the individual process. Usually, the Ald processes are conducted at modest temperatures (<350 °C) and there is a temperature range called "ALD temperature window" which varies between processes. Temperatures outside this window will result in poor growth rates and quality. One of the desired qualities of ALD is its high conformality and aspect ratio. That is achieved by its self-limiting characteristic of growing only one layer at a time. Another quality derived from this is high thickness control. With this technique, one is able to grow very thin and conformal coatings of a wide variety of materials. [23]

2.6 Surface and structural characterization

The Gecko setae and their spatulas, due to their size, fall into the category of nanostructures (size <1 μm). For that reason, more advanced methods and equipment are required for characterising physical or surface properties of Gecko nanostructures. In this work, two methods are discussed, SEM (Scanning Electron Microscopy) and AFM.

2.6.1 Scanning Electron Microscopy (SEM)

This technique is one of the most widely used in characterization of nanomaterials and nanostructures. The resolution of such microscope is in a few nanometres and can operate at magnifications from ~10x to over 300 000x. [10] The construction of a scanning electron microscope is shown on fig. 2-12a.

The source of electrons could be represented by a thermal cathode (usually tungsten filament) and the electrons are emitted thermionically. For field emission guns (FEG), which are of a cold-cathode type (using tungsten single crystal) or thermally assisted Schottky type.

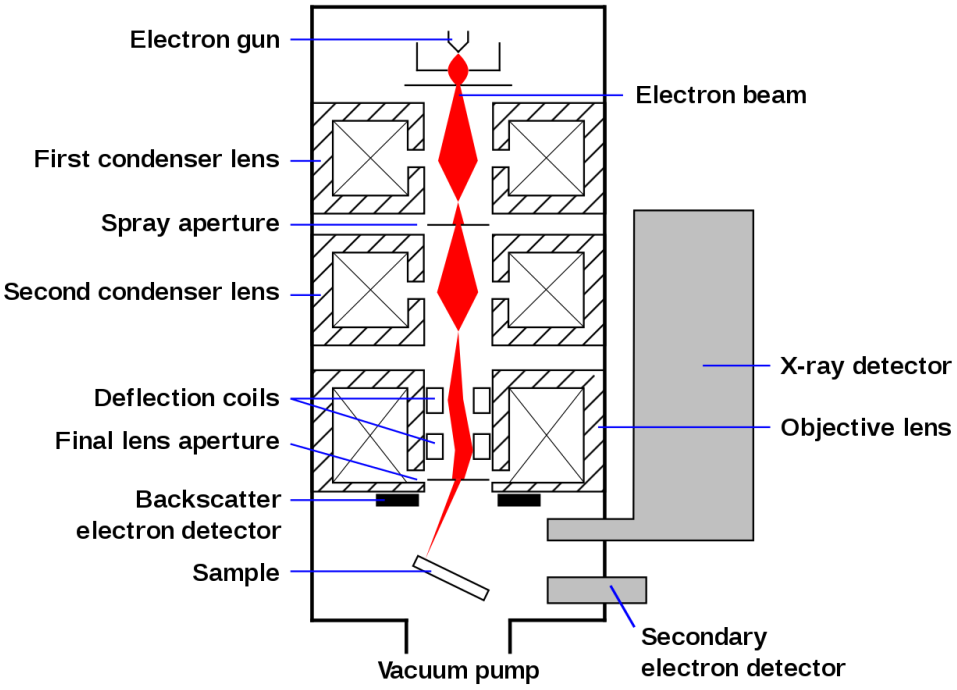

Fig. 2-12 Schematic of an SEM. [24]

This source of electrons is focused into a beam, with a spot size of ~5 nm (or less in modern SEMs) and has energy ranging from 100 eV to 50 KeV. Through the column, it is rastered with deflection coils over the sample surface and as the electrons hit the surface and penetrate it, a number of electron-sample interactions occur (fig. 2-12b). Three types of products of these interactions are typically utilised and detected in SEM imaging: secondary electrons (SE), backscattered electrons (BSE), and characteristic X-rays. An SE is formed, when a beam electron undergoes inelastic collision with an atomic electron to which the primary electron transfers part of its energy. The secondary electron

is then emitted from the sample. BSE were elastically scattered and essentially possess the same energy as the primary electrons. The probability of BSE increases with the atomic number of the sample material, so while they can hardly be used for topology imaging, they can develop a useful contrast between two materials of different atomic number. The primary electron can excite a core electron from the surface atoms, and the excited electron can emit a characteristic X-ray photon (Auger electron) while returning to its ground energy state, which can be used for chemical characterization. [10]

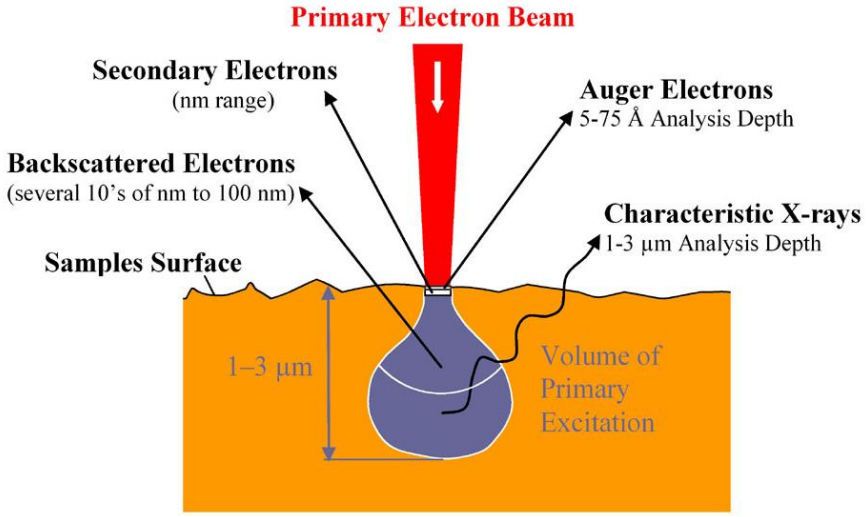

Fig. 2-13 Electron-sample interactions at the surface of the scanned sample and areas of their product's formations.[25]

The resolve power or resolution R of SEM instruments is determined by the wavelengths of the electron beam λ and the numerical aperture NA of the system:

$$R = \frac{\lambda}{2 \cdot NA} \tag{5}$$

where the numerical aperture NA is represented by each objective and condenser lens system.[10]

2.6.2 Atomic force microscopy (AFM)

On contrary of the SEM imaging, the scanning probe microscopy (SPM) offers the possibility to manipulate molecules or nanostructures on the sample surface and measure probe-to-sample interactions. Although there is some level of hybridization in SEM equipment, where a simple probe can be controlled above the sample for nanomanipulation (piezo mounted tips). SPM consists of many different techniques of sample-probe interaction but is represented by two major members scanning tunnelling microscopy (STM) and atomic force microscopy (AFM). [26]

By modifying the STM, Binning, Quate, and Gerber developed the AFM in 1986 as a collaboration between IBM and Stanford university. Unlike STM, the AFM can be used to study insulators, as well as semiconductors and conductors. The probe used is a sharp tip less than 5 µm tall and 10 µm in diameter at the base. This tip is located at the end of a cantilever beam that is usually 100-500 µm long. Some examples of tips can be found in fig. 2-14. [26]

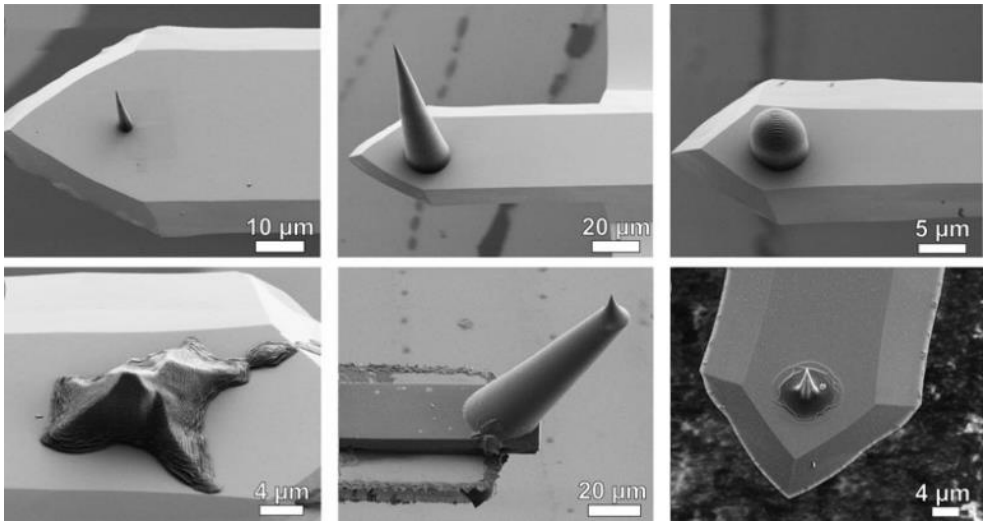

Fig. 2-14 Examples of tips of different shapes and sizes mounted at the end of a cantilever. [27]

The AFM obviously measures the tip-sample interactions and of various types. At short distances, the van der Waals interactions are predominant. They were discussed in chapter 1.3.1. In addition to van der Waals forces, some long-range forces may act and become significant at longer distances, where the weak van der Waals forces don't work. Such forces include electrostatic attraction/repulsion, current induced or static-magnetic interactions, and capillary forces (caused by water condensation on the tip and sample). [10, 26]

During measurement, the cantilever beam bends according to the interactions of the surface and the force, that causes that motion can be as small as 10^{-18} N. [28] The detection of this beam deflection is measured by a laser diode (fig. 2-16), which light is reflected from the surface at the cantilever end and an adjustable mirror onto a photodiode, that senses the small laser beam deviations (distances of 10^{-4} Å).

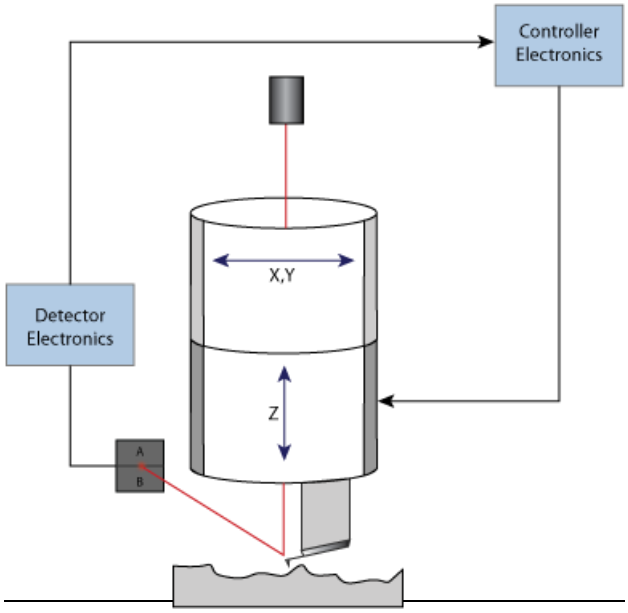

Fig. 2-15 Feedback loop control with a piezoelectric in an AFM system for maintaining constant cantilever deflection or oscillation amplitude. [28]

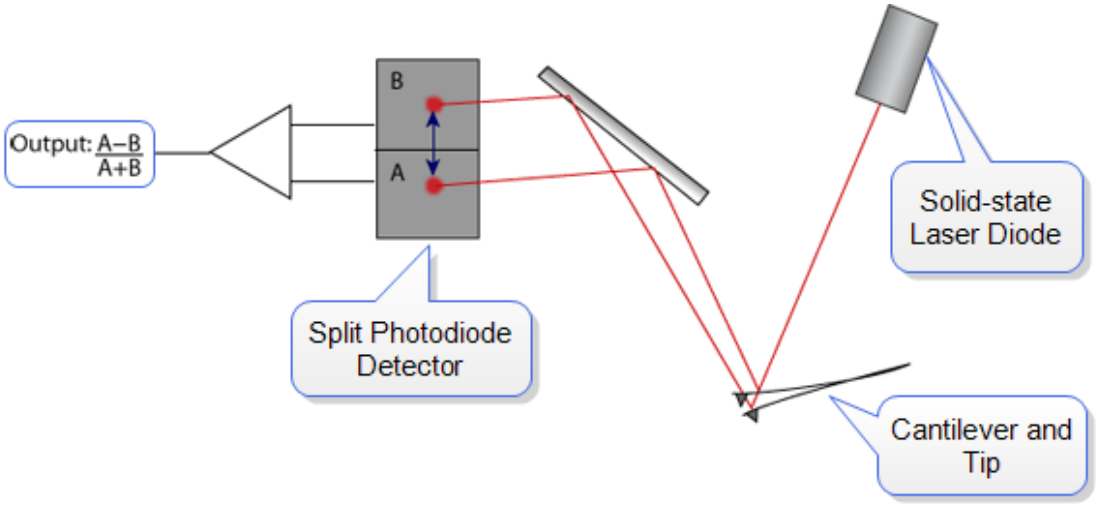

Fig. 2-16 The schematic of a cantilever beam deflection detection by a photodiode. [28]

There are 3 primary modes of AFM:

1) **Contact mode** where the tip is in perpetual contact with the sample. The probe gently scans the topology of the surface and the feedback loop maintains a constant cantilever deflection so the force between the tip and the sample remains constant. To maintain a "setpoint" deflection, the piezo scanner moves vertically to compensate for the tip deflection caused by surface roughness.

   This force is calculated from Hooke's Law [26, 28]:

$$F = -k \cdot x, \tag{6}$$

   where F is the deflection force, k is the spring constant (in contact mode, the spring constant is lower than the effective spring constant of the force holding atoms of a solid together) and x is the cantilever defection.
   Data collected by the computer are the vertical distances of the scanner, for each (x, y) data point. [28]

   Advantages: high scan speeds; "Atomic resolution" images; "Rough samples with extreme changes in vertical topography can be scanned more easily. [28]

   Disadvantages: lateral (shear) forces can distort features in the image; Forces normal to the tip-sample interaction can be high in air due to capillary forces from the adsorbed fluid layer on the sample surface; Combination of lateral forces and high normal forces can result in reduced spatial resolution and may damage soft samples (i.e., biological samples, polymers, silicon) due to scraping between the tip and sample. [28]

2) **Non-contact mode** is one of several vibrating cantilever techniques in which an AFM cantilever is vibrated near the surface of a sample. The spacing is generally on the order of tens to hundreds of Angstroms. The inter-atomic force between the cantilever and sample in this regime is attractive (largely a result of van der Waals interactions). [28]

   Advantage: no force exerted on the sample surface. [28]

Disadvantages: lower lateral resolution; Slower scan speed than Tapping Mode and Contact Mode to avoid contacting the adsorbed fluid layer; Usually only works on extremely hydrophobic samples, where the adsorbed fluid layer is at a minimum. [28]

3) **Tapping Mode**™, the most commonly used of all AFM modes, is a patented technique (Bruker) that maps topography by lightly tapping the surface with an oscillating probe tip. The cantilever's oscillation amplitude changes with sample surface topography. [28]

   In general, Tapping Mode is much more effective than non-contact AFM, but especially for imaging larger areas on the sample that may include greater variation in topography. [28]

   Advantages: higher lateral resolution on most samples (1 nm to 5 nm); Lower forces and less damage to soft samples imaged in air; Lateral forces are virtually eliminated, so there is no scraping. [28]

   Disadvantage: Slightly slower scan speed than Contact Mode AFM. [28]

2.6.3 Force-Distance Curves

A good way to measure the force between a cantilever tip and a surface are Force-distance curves, that measures the cantilever deflection while it is approaching the sample surface. The deflection is directly proportional to the tip-sample force. The force distance curves contain the following useful information:

- The sensitivity of the detection method can be determined;
- Properties like the sample elasticity or the maximum tip-sample adhesion force can be accessed;
- The working point (setpoint for the cantilever deflection signal) for subsequent AFM imaging can be characterized and chosen properly. For instance, when imaging is performed in the attractive force regime it can be determined how far the working point is located from the point of snap-to-contact.
- A force-distance curve can be used to determine the tip-sample force-distance dependence, at least partly.[26]

The aim is to obtain the tip-sample force $F_{ts}(d)$ as a function of the tip-sample distance d, as indicated in fig. 2-17. What is actually measured when acquiring a force-distance curve is the deflection of the cantilever z_{tip} (which is proportional to the tip-sample force) as function of the z-position of the sample z_{sample}.

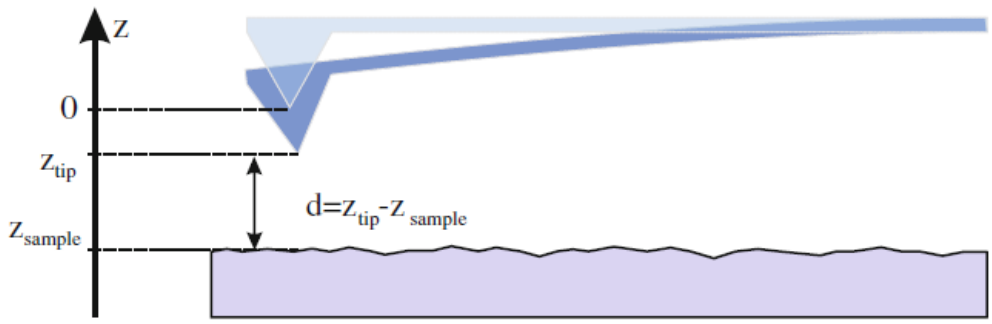

Fig. 2-17 Denotation for the coordinates used in force-distance plots. [26]

An example of a force-distance measuring plot is shown on fig. 2-18 where the *blue curve* corresponds to an approach (extension) of the tip toward the sample, while the *red curve* corresponds to a retraction of the tip. At points *c* and *f* the force gradient becomes equal to the spring constant of the cantilever and when the force value further increases, the plot jumps to point *d* (snap-to-contact). The maximal cantilever deflection at point *c* multiplied by the spring constant gives the maximum attractive force before snap-to-contact (usually quite small). [26]

At $z_{tip} = 0$ the cantilever is unbent, because the tip-sample interactions compensate each other. When the tip pushes further into the surface, the tip moves with the surface and the slope of the repulsive force rises very sharply upwards. Specifically for a stiff sample with a high elastic modulus, the $z_{tip}(z_{sample})$ curve is a straight line with a slope of one. If the sample is soft, the slope can be (initially) smaller than one (due to an indentation of the tip into the sample), resulting in information about the elastic/plastic deformation of the sample. [26]

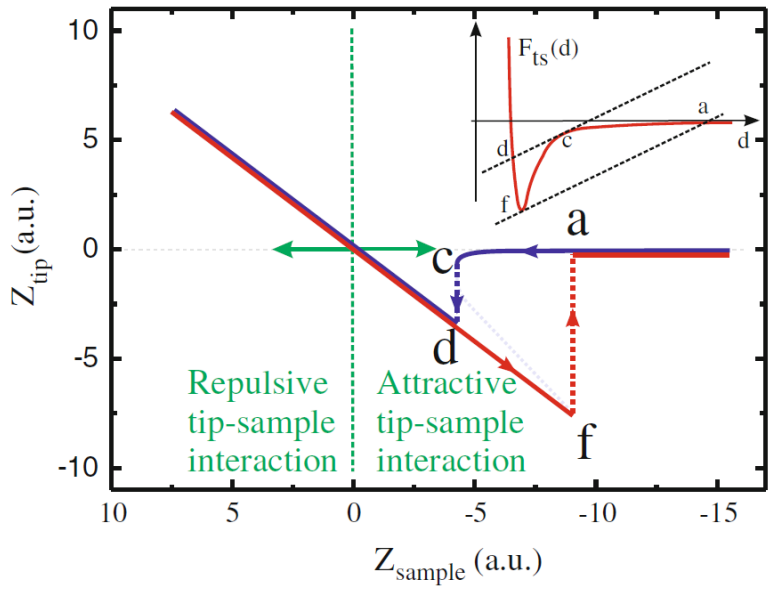

Fig. 2-18 A force measuring plot where the horizontal axis describes movement of the tip towards the sample and the vertical axis is the deflection of the tip caused by attractive and repulsive forces. [26]

If the direction of the sample motion is reversed, the tip motion follows the same straight line in the reverse direction (red line) for stiff samples. The repulsive tip-sample force decreases continuously and finally the attractive regime is entered again, where tip and sample adhere to each other as long as the tip-sample force gradient is smaller than the cantilever spring constant. If the force gradient becomes larger than the cantilever spring constant, the cantilever snaps out of contact (point *f*). The tip snaps back to a position where the deflection of the cantilever is close to zero (point *a*). Point *f* corresponds to the position at which the maximum attractive force (adhesion force) between tip and sample acts. [26]

2.6.4 Wetting properties of materials and their measurement

The wettability of a surface material is influenced by its surface chemistry. That means, that the interactions with water molecules depends on how well the material surface corresponds to the polar nature of a specific liquid. Based on the interactions of water droplets on a solid surface, the surface can be categorized as hydrophilic, hydrophobic or superhydrophobic. A hydrophilic surface shows strong affinity towards water and the water contact angle is < 90°, whereas a hydrophobic surface strongly repels the water at a contact angle > 90° and water tends to "bead" on the surface. Fig. 2-19 doesn't show a superhydrophobic contact, when the contact angle is > 150° [29, 30]

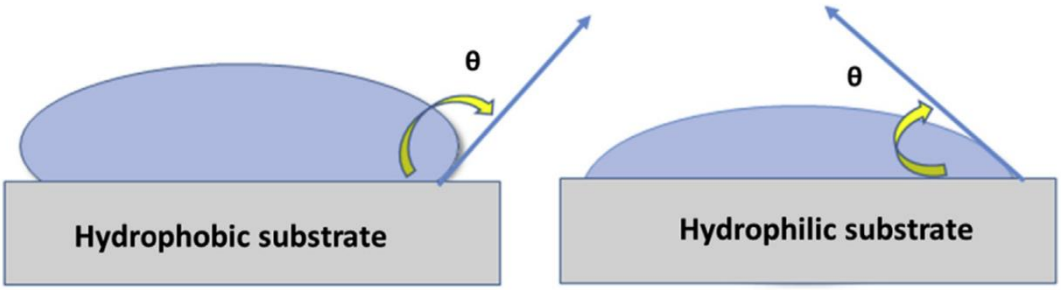

Fig. 2-19 Schematic look of interaction of water molecules with different substrate. [29]

The contact angle is an effective method to understand surface interaction with three phase system (solid/liquid/air). When a drop of water is added onto a surface, the intersection of these three phases appears in one point (fig. 2-20). The contact angle depends mainly on the steady forces at this boundary. It is the significant measure of surface wetting behaviour; it is expected to be the characteristic property of given surface in the particular environment and was first discussed by Thomas Young. The contact angle on an ideal flat surface is described by the Young's equation [29, 31]:

$$\cos\theta_{\mathrm{Y}} = \frac{\gamma_{\mathrm{SG}} - \gamma_{\mathrm{SL}}}{\gamma_{\mathrm{LG}}} \tag{7}$$

where θ_{Y} represents Young's contact angle, γ_{LG}, γ_{SG} and γ_{SL} symbolize the liquid-vapor, solid-vapor and solid-liquid interfacial tensions, respectively. Young's equation is derived from the hypothesis that the surface is an ideal surface – rigid, flat, nonreactive, inert, homogenous, insoluble, smooth, and nonporous. [29]

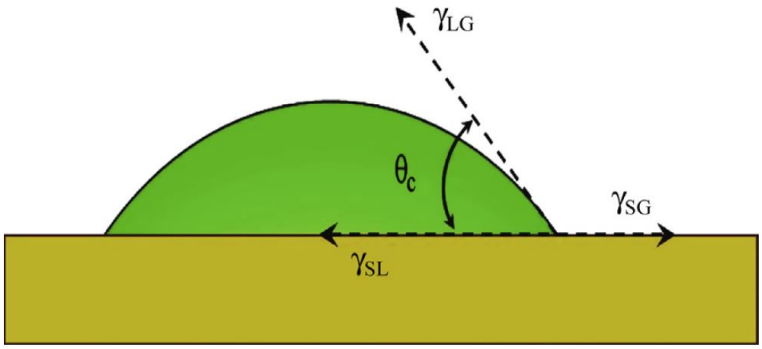

Fig. 2-20 Contact angle formed when the liquid spreads over the surface. [29]

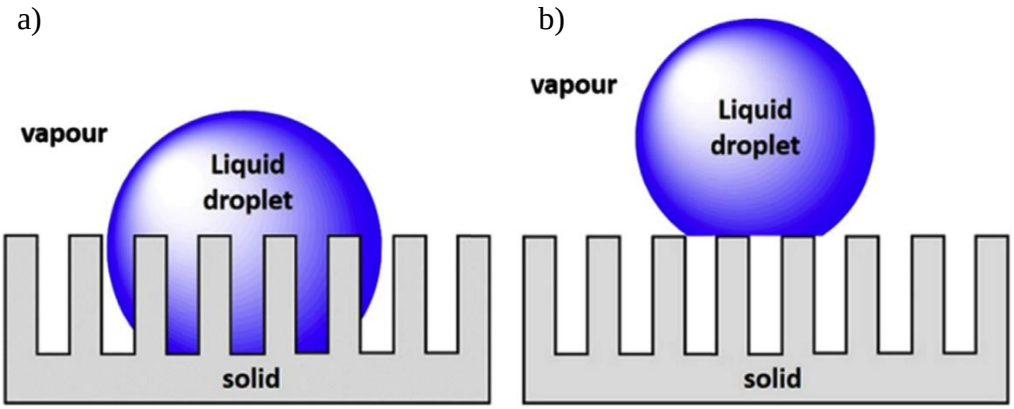

Fig. 2-21 A schematic showing the behaviour of a water droplet on a rough surface in (a) Wenzel's and(b) Cassie's state. [29]

For a rough surface, the contact angle can be described by Wenzel's model or Cassie-Baxter's model (see fig. 2-21). In the Wenzel model, the droplet was assumed to permeate into the rough surface and to contact the rough surface thoroughly. The contact angle on the rough surface (θ_W) can be estimated by Wenzel equation [29, 31]:

$$\cos\theta_W = R_f \cos\theta_Y \tag{8}$$

where the roughness factor (R_f) is defined as the ratio of the actual to the apparent surface area and, hence, is larger than unity. The topological features of the surfaces are presumed to be insignificant related to the drop dimensions. Also, their geometry is irrelevant as long as it does not affect the surface area. [29]

On the other hand, the Cassie-Baxter model assumes the droplet in contact with solid with air trapped in the interface. The Cassie equation was depicting derived contact angle changes for two components [29]:

$$\cos\theta_C = f_1 \cos\theta_1 + f_2 \cos\theta_2 \tag{9}$$

where θ_C is the Cassie contact angle, f_1 is the fractional surface area with contact angle θ_1,

and f_2 is the fractional surface area with contact angle θ_2. The Cassie-Baxter equation is a simplified equation (9) for a porous surface ($\theta_2 = 180°$) and it was given as[29]:

$$\cos\theta_C = f_1 \cos\theta_1 - f_2 \tag{10}$$

Primarily, the Cassie-Baxter equation was derived to determine the wetting characteristic of porous substrate and it is applicable to a hydrophobic rough surface when liquid molecules do not penetrate into the surface structure. One of the advantages of Cassie-Baxter approach over Wenzel's model is that it pronounces the real systems analysis more precisely [32], but it fails to accurately determine the parameters f_1 and f_2 for randomly rough surfaces.

Contact angle measurement – Sessile drop technique

This method is one of the most extensively employed for directly analysing the tangent angle at the three-phase equilibrium interfacial point. Contact angle for flat surfaces is determined by direct measurement of contact angle by viewing the drop profile. On fig. 2-22 it is shown, that an image of an adhering liquid drop can be projected onto a screen and the outlines traced, there after the angle is measured. [29]

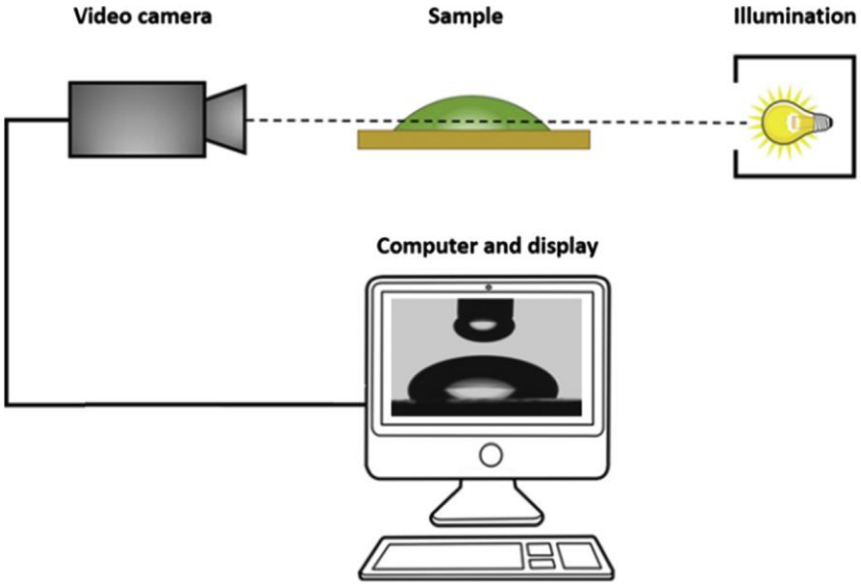

Fig. 2-22 A schematic of an analyser for the sessile drop technique. [29]

This method has the advantage of simplicity in operation and only small surface area of substrates and small amounts of liquid are required. On the other hand, there is a comparatively higher influence of impurities due to the small size of the substrate and liquid. The reproducibility and accuracy of contact angle measurement mainly depend on the assignment of the tangent line and consistency of the operator. [29]

Some guidelines for practical application of this technique:

- the telescope/camera should be tilted down slightly (1-2 degrees) off the horizon so that the surface-liquid phase is not out of the line of sight and a part of the reflection of the formed drop is observed;
- starting the growth of drop, it should have a diameter of about 5 mm and the needle should have the smallest diameter possible, to not distort the drop profile shape;
- measuring both sides of the liquid drop and using averaged angles is advisable. [29]

Drawbacks of this method are an environmental effect on the measuring surface (e.g. humidity) and lower contact angles (below 20°) add an uncertainty value to accuracy of measurement, because the droplet profile is almost flat. Also, the surface roughness and dust may cause deviations in the contact point along the three-phase contact line. Furthermore, the dependency of the contact angle on the drop profile also causes a systematic problem. Despite all these constraints, the sessile drop technique is deliberated to be the most effective method. [29]

3 DESIGN AND FABRICATION OF GECKO BIOMIMETICS

The term “biomimetics” (from Greek word *biomimesis)* refers to artificial designs or derivations inspired by objects found in nature. From understanding the basic principles of how these natural “tools” work at the nanoscale, at least, one can try to recreate nanostructures, nanomaterials and processes with desired functionality, in other words, mimicking biology of creatures or plants in nature. [2, 33]

Considering this in creating a gecko inspired design, it’s important to state what is the desired functionality of final structures. The aim of this work is to create a surface on which mechanical forces will be measured and analysed and additionally modified to enhance its capabilities.

3.1 Topology

It is technologically not feasible (practically impossible), with available tools, to recreate the same fine fibrillar structures as on the gecko setae. But for the purposes of this work a simple array of small polymeric pillars, with distances comparable to their size, are sufficient. The adhesive forces can be then measured on a larger set or on an individual pillar. The topology of such array has been created in CNST Nanolithography Toolbox, which is shown in fig. 3-1 and fig. 3-2 below.

The design created is made of 4x4 mm square array of dots with a diameter of 1 μm and with a 4 μm pitch (spacing) drawn in a hexagonal pattern (see fig. 3-1 and fig. 3-2d). The topology is sized for a 10 cm (4 inch) wafer piece. Therefore, the squares are distributed orthogonally with a spacing of 1 mm, so that most of the effective surface of the wafer is covered (fig. 3-2a). The total amount of dots per square is around 1 150 000.

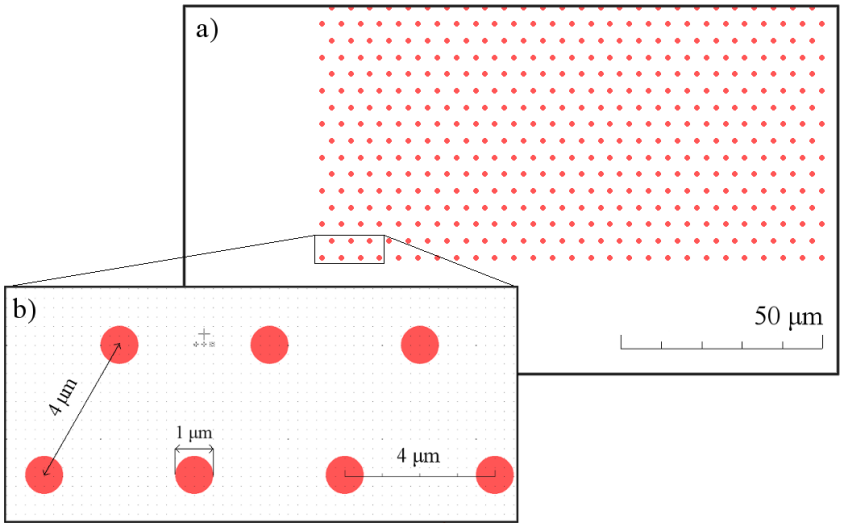

Fig. 3-1 (a) Design dots representing top-view of individual Gecko pillars and (b) details of arrangement and dimensions of the dots

Around the squares are additional comb-shaped and L-shaped check markings of different sizes (e.g. 1 µm check mark in fig. 3-2e) to inspect deviations of dimensions from different fabrication steps. For similar reasons, four 4x4 mm windows were added to the design instead of dots, so they can also be used for reference purposes later in the fabrication process (red squares in fig. 3-2).

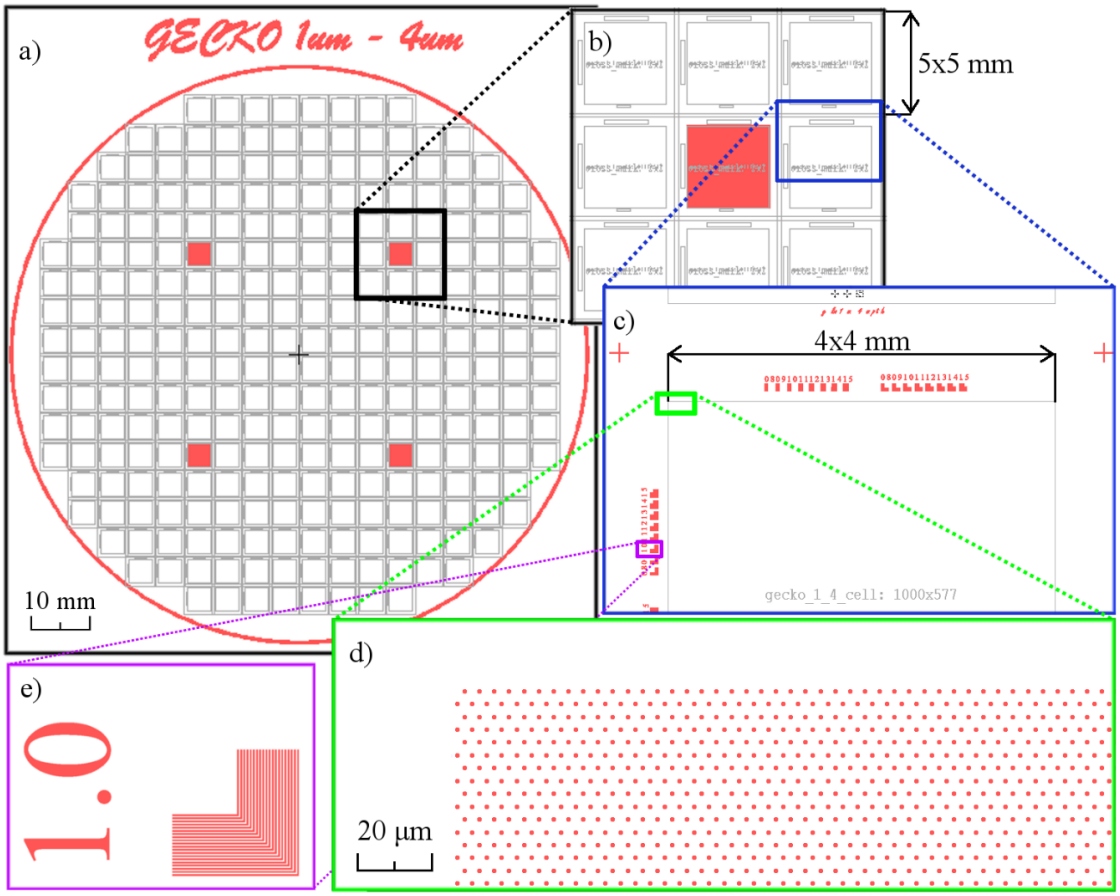

Fig. 3-2 (a) Levels of topology fitted for a 4 inch wafer; (b) detail on the copies of squares with one of the reference windows (red square); (c) dimensions of a single square with (d) the array of dots; purple rectangle shows (e) an example of an L-shaped 11 µm sized check mark.

The layout presented is only one version of many variations, including larger (up to 2 µm) and smaller dots (0,5 µm) and different pitch. The level of spacing will probably have effect on the adhesive behaviour of the final Parylene C structures. Mostly, the finer layout will be used, that is 0,5 µm dots with 1 µm pitch for the creation of the pillars, and 0,5 µm dots with a pitch of 2 µm and higher for adding “bubbles” on top of the pillars. The preparation of structures with “bubbles”, and their function, will be discussed in the following chapters.

3.2 Photolithography of Gecko wafers

A 380 μm thick, one-side polished, silicon (Si) P-type wafer and with a 200 nm layer of PECVD grown silicon dioxide (SiO_2) was chosen as the substrate for next fabrication steps. The requirement of SiO_2 layer will be explained in following chapters. The photolithography and development were carried using Resist coating and development system SÜSS MicroTec RCD8 and the Mask Aligner, Nanoimprint Lithography SÜSS MicroTec MA8/BA8 Gen3.

The RCD8 coat and develop platform provides an option to semi-automatically coat resists with a GYRSET® enhanced coater and after reconfiguration it works as a puddle & spray developer tool. It can handle small pieces as well as standard wafers up to 200 mm and serves therefore ideally for daily R&D work up to small scale production.

MA8/BA8 Mask aligner is great for resist film preparation for fabrication of nano- and microstructures. It houses a mercury arc lamp with a light source of a wavelength from the UV spectrum (193 – 405 nm) to expose thick and thin photoresist films.

Fig. 3-3 Finished negative glass mask carrier after DWL lithography with 1 μm sized dots with 4 μm pitch.

For Gecko lithography a glass mask was chosen, with one side coated with a thin layer of chromium covered with a photo-resistive polymeric film. Using UV Direct Write Laser (Heidelberg Instruments DWL 66-fs) lithography system the PR film was exposed, and the uncovered metal further etched. The photo of this mask is on fig. 3-3.

Using the previously prepared mask carrier the whole photolithography procedure follows these steps:

1. Cleaning the wafers using oxygen plasma in Resist stripper Diener Plasma cleaner from any surface contamination.
2. HMDS – coating a monolayer adhesion promoter for the PR. The reason is the layer of SiO_2 which is hydrophilic and on surface forms OH^- groups that decrease the wetting properties of the PR. HMDS, formed on the surface from vapor at around 135 °C, replaces them with alkyl groups.
3. Coating AZ 5214E on RCD8 – the spin-coater applies this PR uniformly by spinning it at fast speeds. In this case, the rotating speed of 6000 rpm spreads the PR layer to form a thin film. Due to capillary forces, the layer at the edge of wafer is slightly elevated, which could result in an unwanted gap between the mask and the PR during exposure in contact mode. So, while spinning, the edge bead is removed by a small stream of solvent.
4. Softbake the PR – the 110 °C temperature the evaporation of the solvent agent causes PR hardening and additional thinning to final thickness of ~1,1 µm. Cooling of the wafer is needed before next step.
5. Exposure in contact mode – exposing the PR with a dose of 90 mJ/cm^2 (around 60 sec) using MA8 while the glass mask carrier is in contact with the surface of the PR coated substrate.
6. Developing with AZ 726 MIF (solution of TMAH and deionized water with surfactants) – RCD 8 is configured for development. The developer forms a "puddle" on the wafer dissolving exposed areas of PR. Then it is rinsed off and the wafer is spun for final drying with blowing nitrogen gas nozzle.

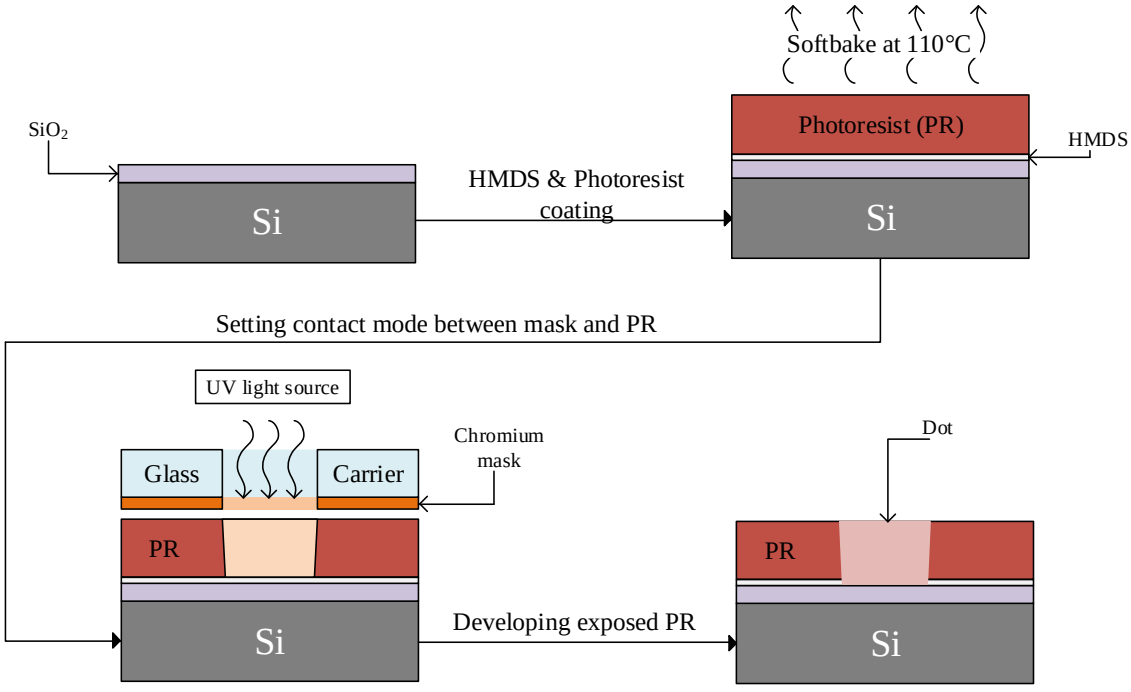

Fig. 3-4 Process chart of the lithography fabrication phase (not to scale).

After these process steps (see fig. 3-4) the result is an oxidised Si wafer coated with ~1,1 μm thick positive PR film with the desired pattern developed forming a negative polymeric mask (photo in fig. 3-5a). The PR profile achieved in the area of dots is expected to have a positive slope slightly less than 90° (>85°).

As stated in previous chapter, a smaller scale version of the layout has been prepared. Additional samples (whole 4" wafers) were provided with dots scaled to 0,5 μm in diameter and with a 1 μm/2 μm/5 μm pitch. To create such fine image with available lithography tools is proven difficult, therefore, they have been prepared in a foreign facility NIST (National Institute of Standards and Technology – USA) and are included in next fabrication and analysis steps. One example is shown in fig. 3-5b as a photo-image of the wafer after finished photolithography. It's important to note, that the thickness of these wafers is 525 μm with 100 up to 560 nm of thermal SiO_2.

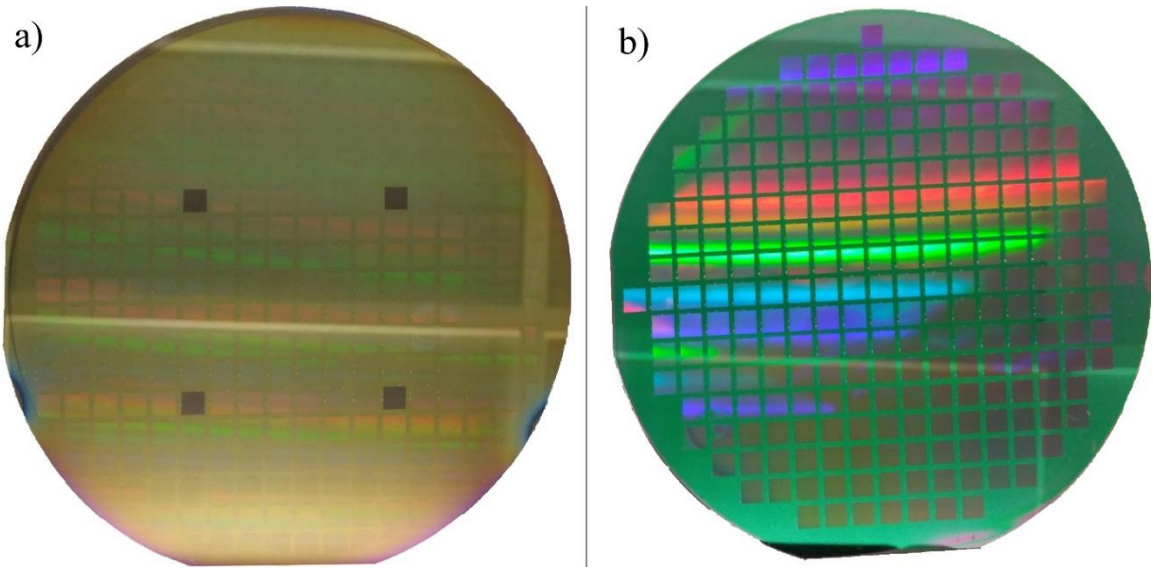

Fig. 3-5 Photos of wafers after photolithography: (a) 1 μm holes/ 4 μm pitch; (b) 0,5 μm holes/ 1 μm pitch.

3.3 Creating holes by plasma etching the SiO_2 and Si

In this stage of fabricating gecko pillars, the topology image has been developed on the PR and the SiO_2 layer is uncovered. In the next step, the SiO_2 is dry-etched in C_4F_8 plasma, while the PR is used as a masking layer. For etching, and later for Si etching, PlasmaPro 100 (Oxford Instruments Plasma Technology) DRIE of Si-based materials is used.

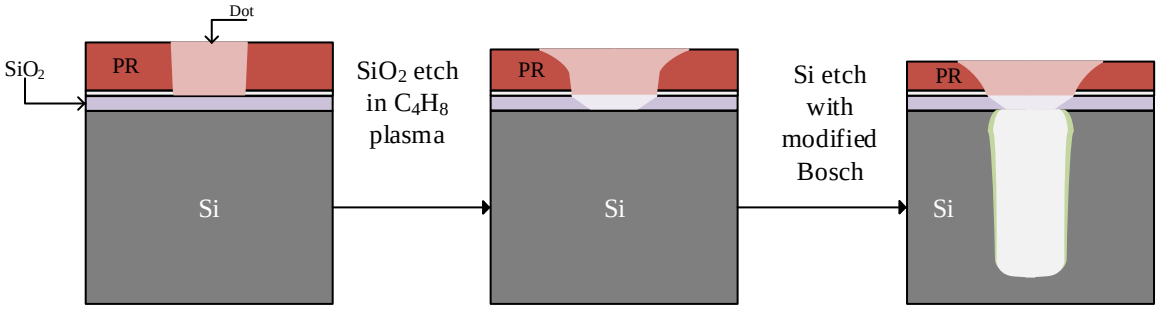

Fig. 3-6 Process chart for etching holes in silicon using modified Bosch process. (in the last step, green layers on the Si walls represent the

After the SiO_2 layer is gone (the parameters of plasma for SiO_2 etch are in table 3-1), the process parameters are set for Bosch etching process. This process step is very critical, because changing the process parameters has fundamental effect on the shape and desired quality of etched holes. Ideally, the profile would have smooth straight walls without under-etching of the mask (SiO_2), and the aspect ratio of >10:1. Two processes have been tried and optimized: modified basic Bosch process and smooth Bosch process.

Standard (basic) Bosch processes used in MEMS fabrication usually aim for high etch rates and vertical profile. [34] Setting the etching and passivation steps to shorter times than is usual in Bosch processes ensures, that the etch rate is slow enough to create small sized scallops. On fig. 3-6 a process chart of the two etching steps is shown, with emphasis on resist erosion. Due to highly accelerated anisotropic ions in the plasma, the PR edges erode, which might uncover the edges of the SiO_2 layers below, that might begin to erode too.

Table 3-1: Process parameters for etching of SiO_2 with table temperature at 5 °C.

Constant process parameters	Various times for different oxide thicknesses	
	Thickness [nm]	Time [s]
• pressure control setpoint at 4 Pa, • ICP power of 2500 W, • forward DC bias of ~120 V, • gas flow: $Q(C_4H_8)$ = 100 $cm^3.min^{-1}$, $Q(O_2)$ = 15 $cm^3.min^{-1}$,	100	30
	360	70
	560	105

3.3.1 Basic Bosch

First process was tried on the wafers with a layout of 1 µm and 4 µm pitch. After photolithography, the SiO_2 layer was etched and immediately after, the substrate table was cooled to – 10 °C and holes were etched for a total duration of 10 minutes (100 cycles). The process parameters (taken from [35]) used can be seen in table **3-2**.

Table 3-2 Process parameters for basic Bosch at -10 °C.

Process tree:	Parameter:	DEP[1]	ETCH
100 cycles ⌊ DEP ⌊ ETCH	ICP power [W]	600	600
	HF power [W] (DC Bias [V])	10 (~70)	30 (~135)
	Pressure [Pa]	1,5	1,5
	$Q(SF_6)$ [$cm^3.min^{-1}$]	10	50
	$Q(C_4H_8)$ [$cm^3.min^{-1}$]	110	10
	Time [s]	2	4

[1] - deposition of passivation layer

On fig. 3-7 below, the SEM images show the resulting structures using the basic Bosch process. The images were taken by Scanning Electron Microscope TESCAN LYRA3. From the images it is clear, that the scalloping is too small to be visible with current magnification. But measuring the width of the holes shows, that it has widened by ~320 nm from the originally designed diameter of 1 µm. Measured depth of ~8,5 µm indicates etching rate of 0,85 $\mu m.min^{-1}$. It's important to note, that the etch rate is not constant with increasing depth, due to process aspect ratio.

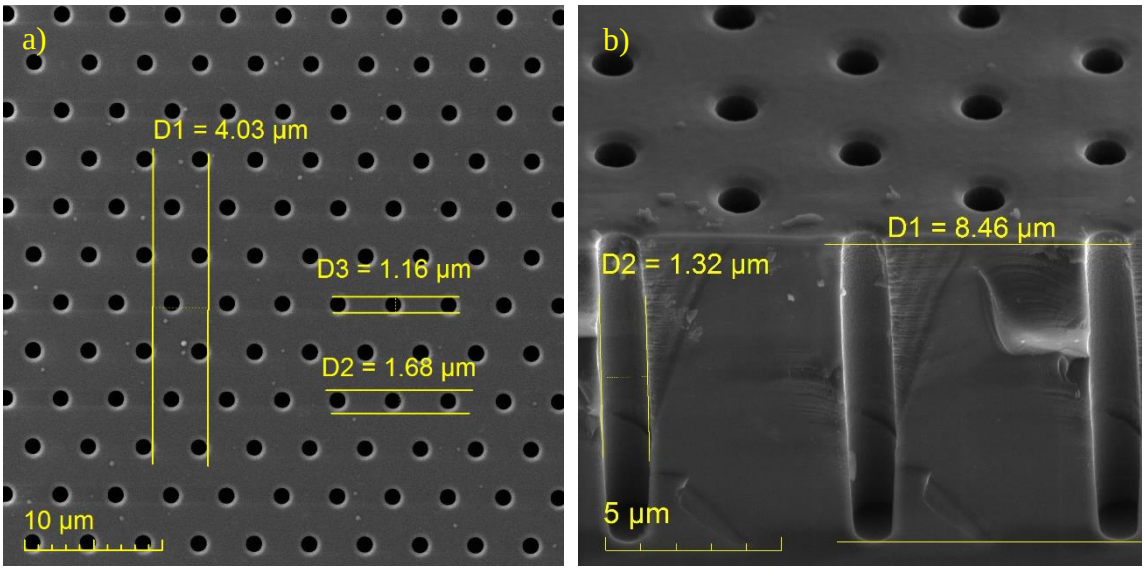

Fig. 3-7 SEM images of 1 µm holes with 4 µm pitch. (a) Top view of the etched holes and measuring the diameter of holes in SiO_2 layer and the erosion of this layer's edge. (b) Tilted cross section of holes and their dimensions.

3.3.2 Smooth Bosch modified process

The process in the previous chapter had eliminated a problem with large scalloping of the walls. The hole widening of ~30% is not a big problem with a 4 μm space between holes, but if the holes are half the diameter and spaced 1 μm from each other, there is a risk of the walls intersecting and, at best, the pillars in final phase might be too close to each other and start attracting themselves.

Therefore, the basic Bosch process needed to be slightly modified to acquire a good profile. A complete overhaul of basic Bosch process is needed -> smooth Bosch has a middle step between passivation and etching step, set to break through the passivation layer on the bottom before an actual Si etch occurs. The duration of this step needed to be optimized, so that the deposited C4F8 polymer is removed but the silicon is not yet etched. After this step, the actual etching of Si occurs. The process uses parameters from table 3-3 (optimised according to [15]).

Table 3-3 Process parameters for smooth Bosch - deep etching of holes into Si at 5 °C.

Process tree[1]:	Parameter:	DEP	BREAK[2]	ETCH #1	ETCH #2	ETCH #3
15 cycles DEP BREAK ETCH #1 15 cycles DEP BREAK ETCH #2 25 cycles DEP BREAK ETCH #3	ICP power [W]	1750	2000	2000	2000	2000
	HF power [W] (DC Bias [V])	-	40 (~120)	-	-	-
	Pressure [Pa]	6.7	4	4	4	4
	$Q(SF_6)$ [$cm^3.min^{-1}$]	10	200	120	170	200
	$Q(C_4F_8)$ [$cm^3.min^{-1}$]	200	10	10	10	10
	Time [s]	0,9	1,1	0,3	0,4	0,5

[1] - etch rates separated into 3 phases with increasing etch time for better profile control.
[2] - break through passivation layer

From the process tree in the table, it is obvious, that the process has more phases. It was important, that the wall profile would be as smooth and vertical as possible. That was done with dividing the process into 3 phases of different number of cycles, where the time and SF_6 flow during etching was set lower at the beginning for minimum scalloping at start. That time had to be increased after a few cycles, because the horizontal etching is decreasing with depth, which would result in narrower holes at the bottom, thus, the profile stops being vertical.

Small initial scalloping can be seen first few cycles on fig. 3-8 but further deep it disappears. The distance D1 marks the depth of ~4,3 μm, which, considering etch time of 2 min and 13 seconds (55 loops) translates to ~1.9 $\mu m.min^{-1}$. This time, the issue of hole widening has improved. Distance D2 indicates, that the hole diameter increased by no more than 16 % of the original diameter of 500 nm. The thickness of SiO_2 layer is not measured in the image, but different measurements showed a thickness of ~90 nm.

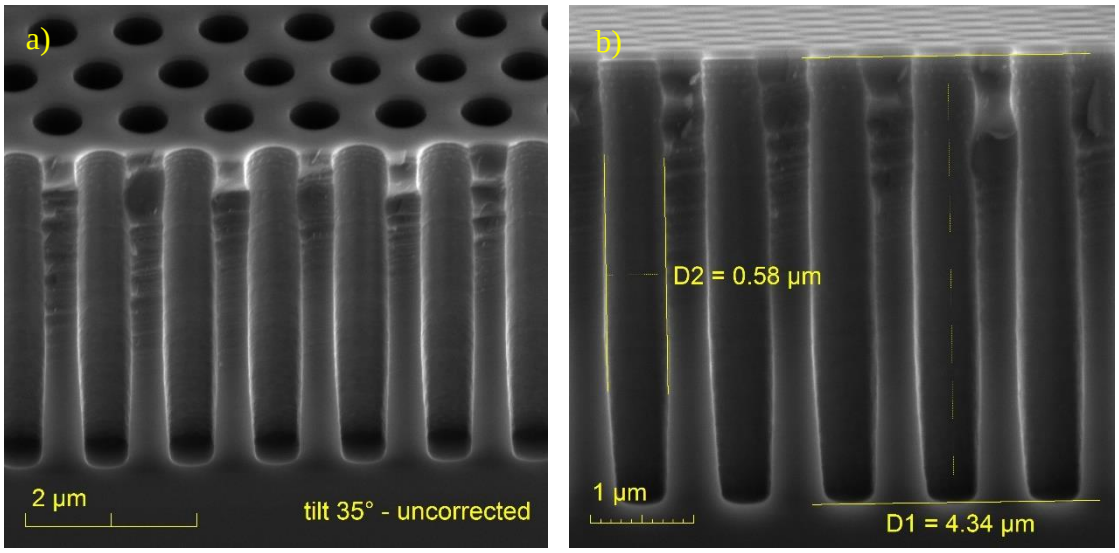

Fig. 3-8 SEM images of (a) tilted cross cross-section showing etched 500 nm holes with 1 µm pitch; (b) dimensions of deep silicon etching of these holes.

This variation of the Bosch process showed more than 2x increase of etch rate. Most likely, during passivation and etching cycles of the first process, basic Bosch suffers from over-passivation. The polymer layer deposition step inhibits the isotropic effectivity of the etching step downwards and also causes higher etching in the horizontal direction. This simple problem is eliminated in smooth Bosch by inserting a break-through step in between passivation and etching step to break the polymer.

3.4 Forming Parylene pillars

After the holes are etched with desired quality, they can now be used as a sort of form for making pillars out of Parylene C polymer. Before the deposition, the PR from the wafers is stripped and they are cleaned in O_2 plasma for removal of any residual organics, including the thin layer of passivation polymer. The backside of the wafers is covered with some adhesive tape to prevent Parylene C from forming there (for later backside Si removal). Fig. 3-9 shows the final fabrication steps of forming the Parylene pillars.

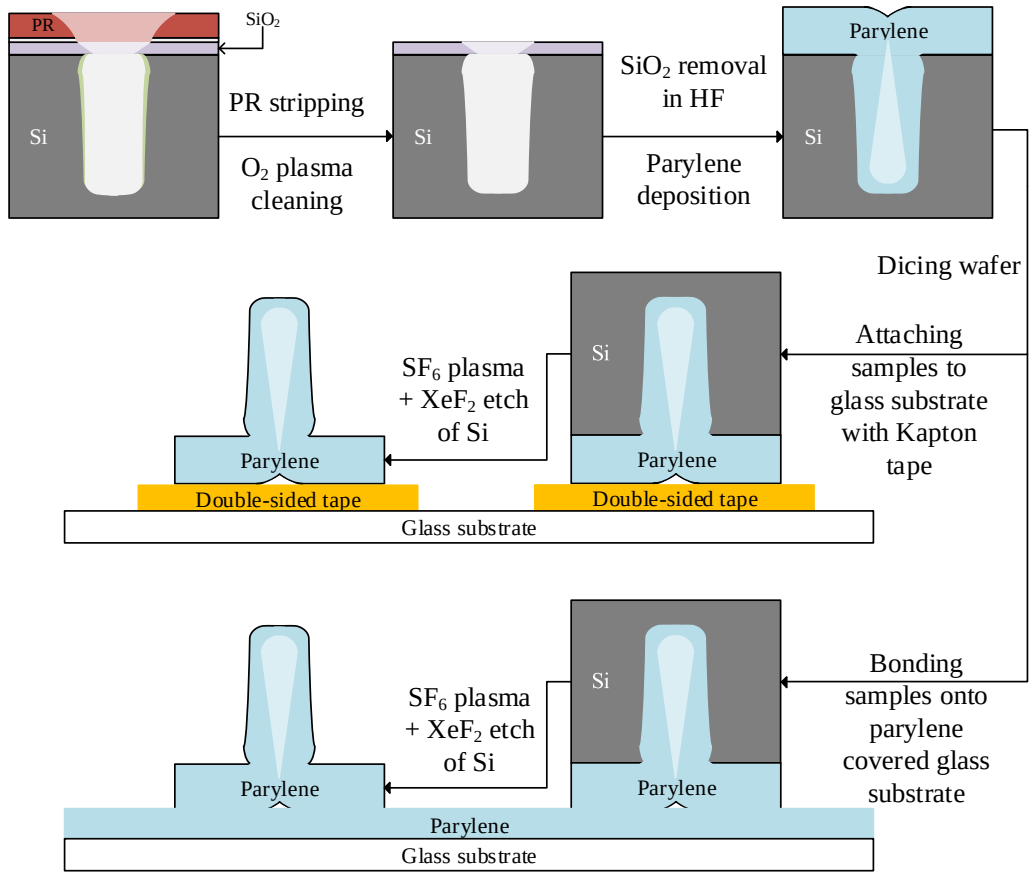

Fig. 3-9 Process chart showing formation of Parylene pillars (light blue shows a cavity inside the pillars), and their preparation for surface modification and adhesion force measurements. (not to scale)

Deposition is carried out in PDS 2010 Labcoter^{TM} 2 with the setup parameters from table 3-4. After polymer deposition, the wafers containing individual sets of pillars are diced into 5×5 mm^2 large pieces. Some of them are selected and mounted top-down onto a thin glass substrate with double sided Kapton tape. Chapter 2.3.1 was exploring a possibility of bonding two Parylene covered substrates together. Some samples were therefore mounted on a Parylene C covered glass substrate and put in an annealing furnace. The result was a moderately strong coherent bond, that is required to hold the polymer structures after XeF_2. At this point, the silicon substrate is fully exposed and its whole volume needs to be etched away to reveal Parylene C pillars.

Table 3-4 : Process parameters for Parylene C deposition using 4 g of Parylene C dimer (resulting in ~4 μm thick polymer layer).

Furnace temperature [°C]	Vaporizer temperature [°C]	Chamber (pressure) gauge temp. [°C]	Pressure setpoint [Pa]
690	175	135*	1,6

* – this temperature prevents polymer deposition on the pressure gauge.

Table 3-5 Setting of the annealing furnace for Parylene C bonding (taken and modified from[19]).

Chamber and table temperature [°C]	Process vacuum [Pa]	Press force applied [N]	Annealing time [min]
240	$< 8{,}22.10^{-5}$	10	60*

* – with a rising ramp of 5 °C. min^{-1}

Low process pressure is important for increasing the mean free path of gas molecules. The greater the mean free path, the easier it is for Parylene C monomers to fit through very small openings, such as the holes of gecko structures. However, a uniform growth of Parylene C is still limited by aspect ratio and is slowed down as the diameter of holes reduces with growing layer of polymer. That results in forming of a cavity inside the buried pillars. During annealing process, high vacuum may help removing most of the gas molecules from between the bondable surfaces and increasing the bonding strength.

The prepared samples, with a silicon thickness of 540 μm, are first etched in DRIE set to isotropic etching process. The SF_6 plasma has shown high isotropic etch rates under right conditions. But the Parylene structures cannot be uncovered in plasma, since they may be damaged by it and by elevated heat generated by high energy ion bombardment. For the same reason, the substrate had to be actively cooled with liquid nitrogen. Therefore, the samples were only thinned using SF_6 plasma isotropic etching down to around 180 μm thickness or less. After that, they were placed inside the vacuum chamber of an XeF_2 isotropic silicon etching system. The XeF_2 gas is non-reactive in any way with Parylene C, so the remaining silicon is etched away. The etching parameters of both processes are in table 3-6.

Table 3-6 Comparison of two different dry isotropic methods for 540 μm Si etching.

Etching method	ICP power [W]	Pressure [Pa]	$Q(SF_6)$ [$cm^3.min^{-1}$]	Cycles [-]	One cycle duration [s]	Etch rate[1] [$\mu m.min^{-1}$]
DRIE isotropic pre-etch	2500	10	300	13	120 (+30)[2]	~ 21
Etching in XeF_2 gas	-	267	-	200	30	~ 5,4

[1] - etch rates measured for 1 cm^2 of uncovered Si surface area;
[2] – each etching cycle followed by 30 seconds of inactivity for cooling purposes.

The table shows, that on 1 cm^2 of etched Si surface area, the DRIE is 4 times faster. Using only XeF_2 gas alone to etch those 0,5 mm thick samples would take around 2 hours. To save a little time and preserve fluoro-xenon gas supply, it's more effective to pre-etch it in SF_6 plasma.

After there is no trace of silicon on the samples, they are ready for surface modification or measurements. On fig. 3-10 the pillars of different dimensions are shown. Parylene C is non-conductive, so prior to SEM imaging, the samples hat to be sputtered on with a few nanometres of gold layer (~20 nm) to prevent charging.

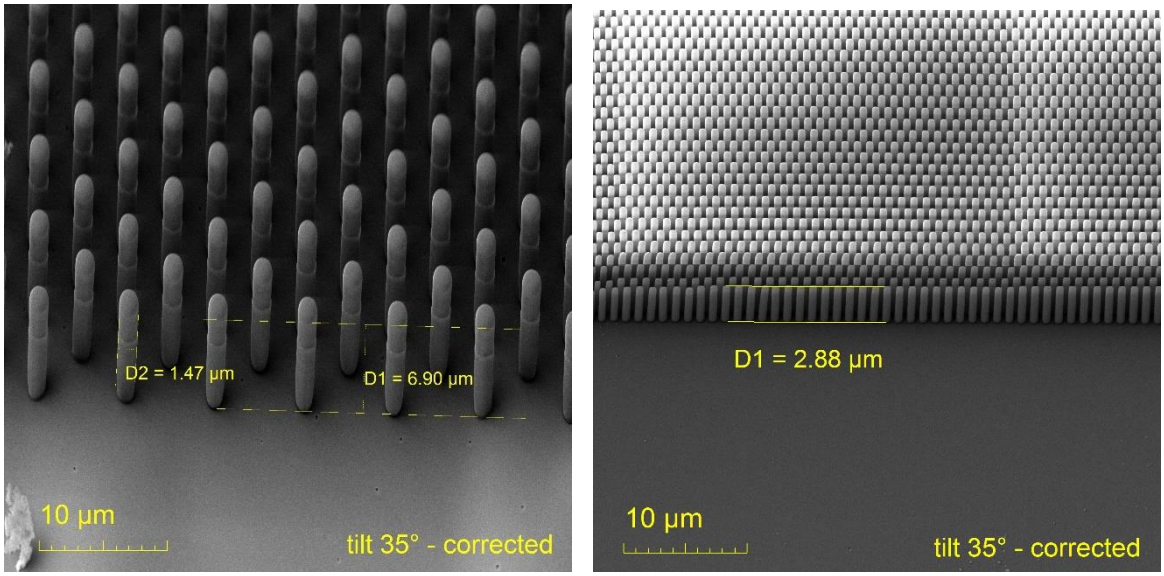

Fig. 3-10 SEM image of (a) ~7 µm tall pillars with ~1 µm diameter and 4 µm pitch; (b) ~2,9 µm tall pillars with ~500 nm diameter and 1 µm pitch

Few details have been noticed during SEM imaging. A flexing of some 500 nm pillars was visible, caused by repulsion of individual pillars after they were charged by a higher density of electron beam current for a few minutes (see fig. 3-11a,b). It means that the stiffness of these pillars might be comparable to the stiffness of gecko spatulas. Another observation confirmed the presumption, that the pillars are hollow (a cavity formed during Parylene C deposition), when some of the pillars broke by some external influence (see fig. 3-13c). This fact could mean a limitation for further miniaturisation of the pillars, since the cavity has been sealed shut under process vacuum. And because Parylene is the atmospheric pressure is several orders of magnitude higher, and the gas permeability of Parylene C is low [36] relative to the sudden pressure shock caused by venting the chamber to atmospheric pressure, thinner pillars might be prone to flattening, or imploding. This phenomenon was also observed in SEM and it is shown on fig. 3-11c.

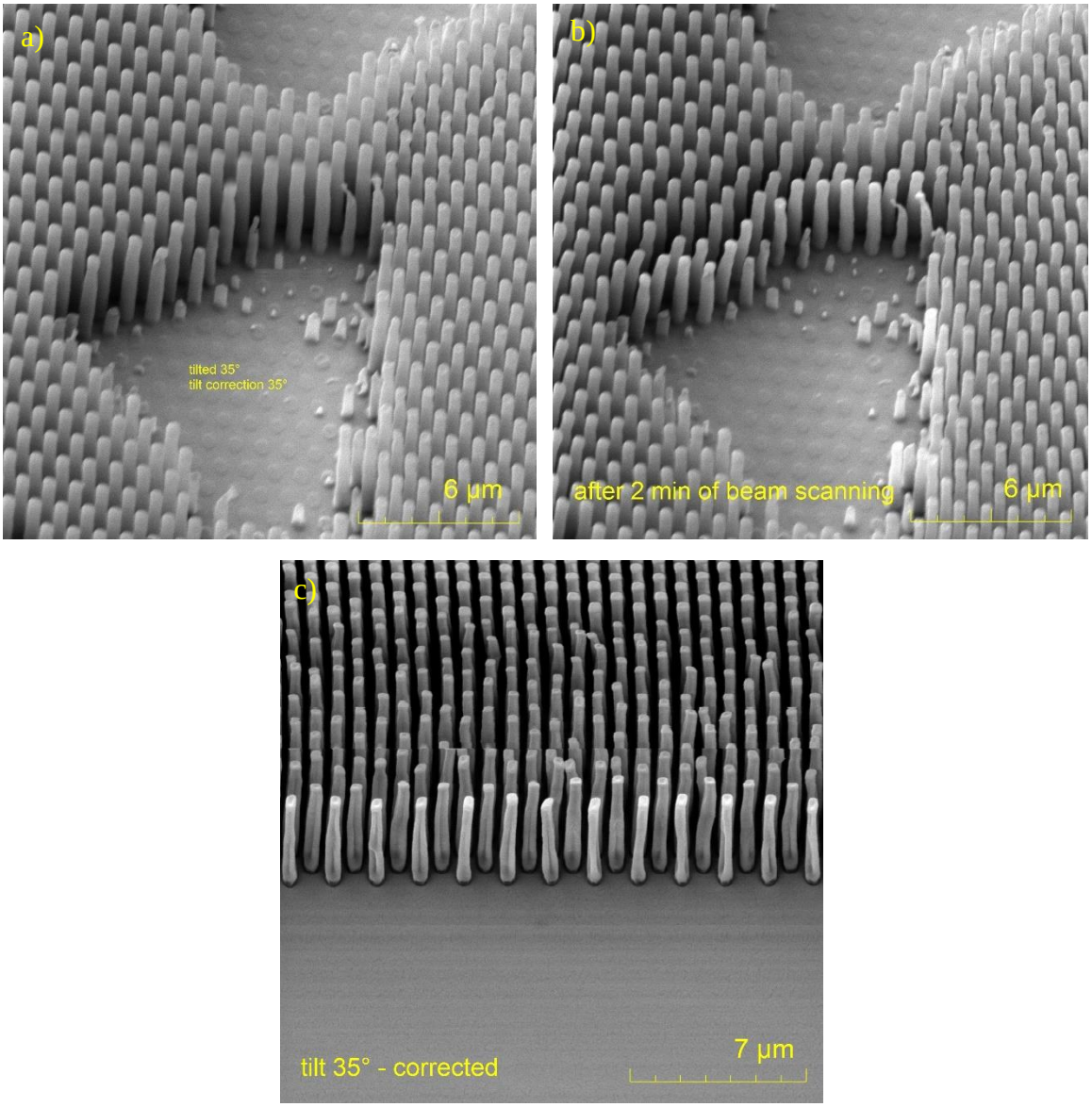

Fig. 3-11 (a) SEM image of 500nm/1 µm pillars on a 35° tilted surface (tilt corrected); (b) a comparison picture, showing bending of pillars after 2 minutes of scanning; (c) thinner pillars being flattened due to atmospheric pressure.

3.5 Forming bubbles on top of pillars

To possibly enhance adhesion of artificial gecko structures, one way is to further increase the surface area. And using knowledge of the fact, that filling holes with Parylene results in hollow structures, one can implement this idea into forming enlarged tips of pillars. The tips would be hollow as well and would resemble a "bubble". The cavity inside would make the bubble extra conformal to the roughness of the surface, which in theory might increase considerably surface-to-surface adhesion.

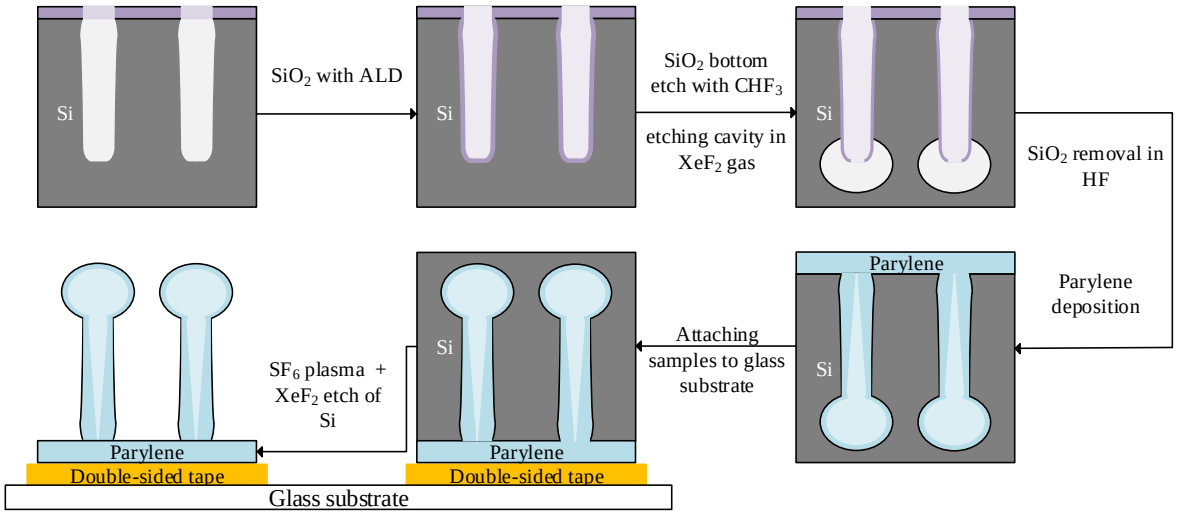

Fig. 3-12 Process chart for creating bubbles from Si substrate with holes etched after DRIE.

Fig. 3-12 shows manufacturing steps to form such structures. Using the technology of ALD and its ability to deposit conformal coating even on deep vertical surfaces, one can grow a thin (~ 5nm) layer of SiO_2 on the inside of the holes etched after Bosch process, while the original substrate oxide layer remains and cover the top surface.

Table 3-7 Process steps for plasma enhanced ALD of 5 nm SiO_2 using TDMAS as a precursor.

Step	Parameter	Value	Comments
1	Deposition chamber temp. [°C]	150	Set the chamber stabilisation and waiting for stabilization.
2	$Q(Ar)_1$ [$cm^3.min^{-1}$]	30	Set process argon flow rates.
3	$Q(Ar)_2$ [$cm^3.min^{-1}$]	100	
4	TDMAS pulse time [s]	0,4	Precursor pulse at room temp., followed by 5 sec. purge.
5	$Q(O_2)$ [$cm^3.min^{-1}$]	50	Oxygen flow for plasma step
6	Plasma ICP [W]	300	Plasma turned on for 20 sec.
7	Cycles [-]	80	Number of repetitions from step **4** for 5 nm thin SiO_2 layer.

The process of atomic layer deposition, that was used (table 3-7), runs under medium vacuum below 0,1 Pa. The prefixed "plasma enhanced" points to the fact, that the process uses O_2 plasma as a surface precursor activation that sets a base for TDMAS precursor. One pulse of 0,4 seconds equals around 4,1 mg of the silane precursor being consumed. One cycle creates an oxide layer of 0.63 Å, so for a required 5 nm of SiO_2, 80 cycles are needed.

The thin ALD SiO_2 layer on the bottom of the holes is etched through with a CHF_3 plasma in RIE (see table 3-8). After the Si on the bottom is revealed, a cavity is etched into it with an XeF_2 gas diluted in N_2 for a short period of time (depending on the desired bubble diameter). The parameters of the etching are in table 3-8.

Table 3-8 Parameters of processes used in forming bubble cavities in silicon.

Etching method	CCP power [W]	Pressure [Pa]	$Q(CHF_3)$ [$cm^3.min^{-1}$]	Q(Ar) [$cm^3.min^{-1}$]	Etch time [s]
RIE SiO_2 etch in CHF_3	200	4	12	38	40
	XeF_2 pressure [Pa]	N_2 pressure [Pa]	Cycles [-]		One cycle duration [s]
Etching in XeF_2 gas	200	400	1-2*		5-10*

* - etching of such small cavities is very dependent on the etched surface area and temperature.

To optimize the time needed for etching of ALD oxide at the bottom of a hole with a certain depth had to be optimizes, which was not a difficult task. Controlling the etching of XeF_2 was, on the other hand, very difficult because the amount of material etched is considerably little, and there is a risk of over-etching the bubbles.

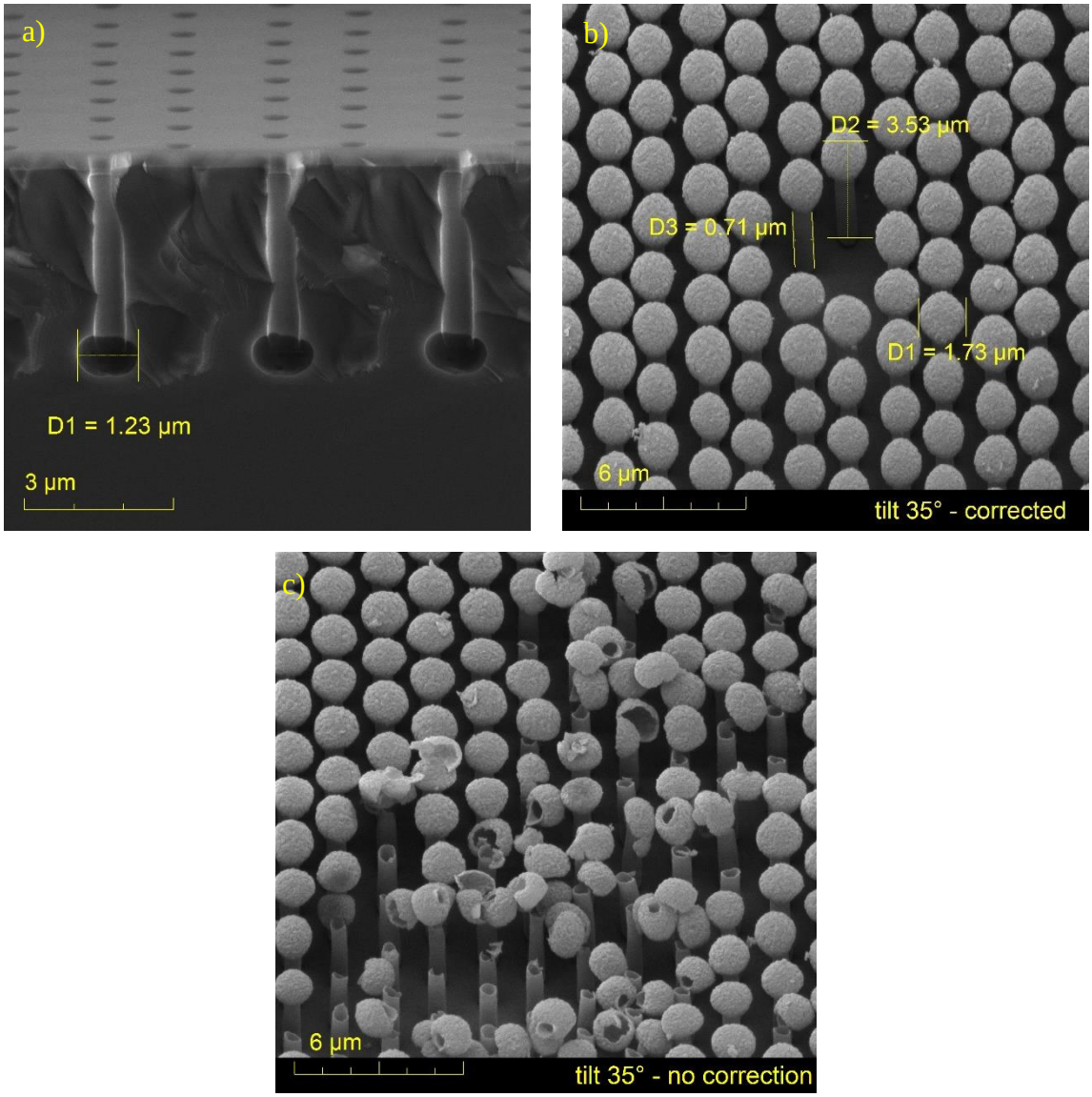

Fig. 3-13 SEM images (a) cross-section of holes with etched cavities for bubble formation; (b) view on Parylene bubble structures with 35° tilted surface (tilt corrected) and their dimensions; (c) proof, that pillars and bubbles are hollow.

3.6 Surface modifications procedures

Surface cure with oxygen plasma:

- The chamber was depressurized below 50 Pa; the flow of oxygen was set to $Q(O_2) = 25\ cm^3.min^{-1}$, and the plasma was fired with 300 W power;
- Duration of the oxygen plasma activation was from 1-1,5 minute and tests were taken on a Parylene C deposited surface, which shown, that the activation has degraded over time, but slowly;
- It is a necessary step before SiO_2 ALD or any silane cross-linking, because it creates OH^- groups.

ALD modification of Parylene surfaces with thin layer (5 nm) of SiO_2:

- An important step before crosslinking β-keratin on gecko biomimetic structures. Unfortunately, the only ALD process chart available for this cause (discussed in previous chapter) is incompatible with Parylene C structures. Possibly, too much strain from plasma radicals with combination of high temperature during ALD on the structures results in their complete destruction.
- The samples, however, survived intact under the temperature alone, therefore the possibility of ALD cover of structures remains open, if a different process parameters are implemented.

Keratin binding on SiO_2

1.) Oxygen plasma activation;
2.) Linking APTES:
    a. Using vacuum oven or Self-Assembly Monolayer chamber– applying 20 ul of APTES near samples -running the process at 120°C/30min;
    b. With toluene:
        - rapidly immersing samples in a solution of 2% V/V APTES in dry toluene;
        - rinse in toluene, then methanol and finally water (each time 5 min and with agitation for the last 2);
        - annealing of the samples at 120C for 2h;
3.) Prepared samples need to be stored dry (in N_2) if possible or be use the same day;
4.) Incubation in 10% glutaraldehyde in potassium-phosphate buffer solution (PBS) (10 mM, pH 7) for 1 hour;
5.) Rinse in PBS and then water twice (each time 5 min under agitation)
6.) Next step is adding keratin of 0.1mg/ml in PBS or other preferred buffer (it's important to mind the Ph of the solution so that the protein stays nicely folded) and leave it for 2h (or overnight);
7.) Rinse in PBS (twice with agitation) and storing wet (in PBS).

4 WETTABILITY AND ADHESION MEASUREMENT

First method used in this chapter is contact angle analysis of various surfaces using water droplets, thus, determining the hydrophobicity or hydrophilicity of the samples. Secondly, the adhesive force direct measurements of these samples are carried out using AFM equipment to measure force curves on the surface.

4.1 Contact angle measurement

Measuring the wettability of different surface variations is a simple, but important step to determine adhesion properties on the surface. It has been done using a SEO Phoenix 300 contact angle analyser consisting of an adjustable table for samples, a water syringe holder with a PC controlled stepping motor (with manual screw override) for dispensing water droplets. The imaging is done with an optically adjustable camera against white LED illuminated background and image processing using Surfaceware 8 software. The software features a surface energy calculator, curved surface sample measuring function

A series of comparative measurements of various surfaces has been carried out. Two variations: unstructured (flat) and structured (pillars/bubbles) surfaces of Parylene C have been observed, either untreated or treated/modified with O_2 plasma, SiO_2 (ALD), silanes and β-keratin.

On fig. 4-1a, the surface of untreated Parylene C shows a contact angle >90°, which makes the sample slightly hydrophobic. On the contrary, fig. 4-1b shows, that treating the unstructured Parylene surface with oxygen plasma significantly increases the adhesion.

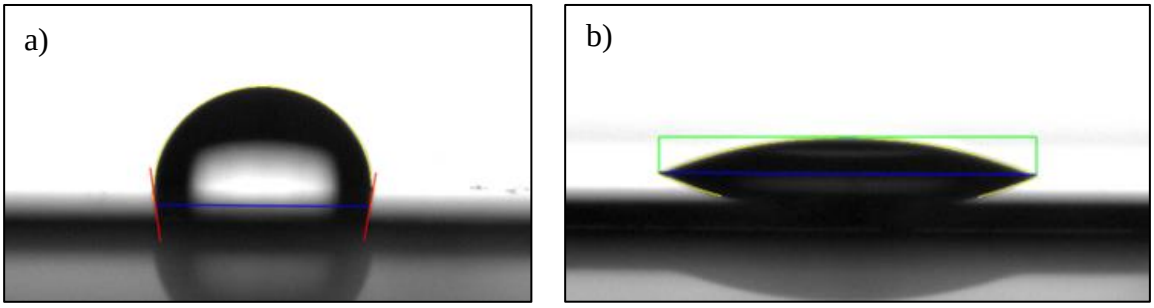

Fig. 4-1 Contact angle of a water drop on: (a) untreated Parylene C flat surface (99°) and (b) flat Parylene C surface treated with O_2 plasma (23°)

Parylene pillars of 0,5 μm diameter and 1 μm pitch (fig. 4-2) showed a different result when treated with plasma. The roughness caused by the structures present made the surface more hydrophobic than is the case of an untreated flat Parylene surface. Therefore, it has been concluded, that the plasma treatment might not have an effect on surface hydrophobicity and the and that there is an apparent correlation with the behaviour of a water droplet on a rough surface explained by Wenzel and Cassie and discussed in chapter 2.6.4.

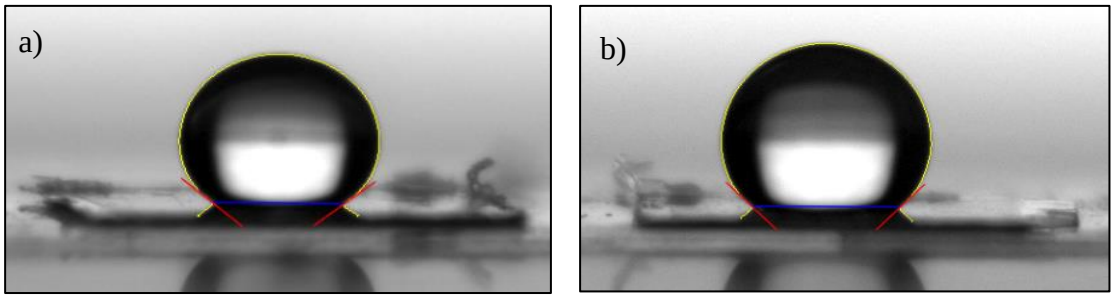

Fig. 4-2 Contact angle of a water drop on Parylene C 500 nm/1 μm pillar structures with: (a) untreated surface (140°) and (b) plasma treated surface (134°).

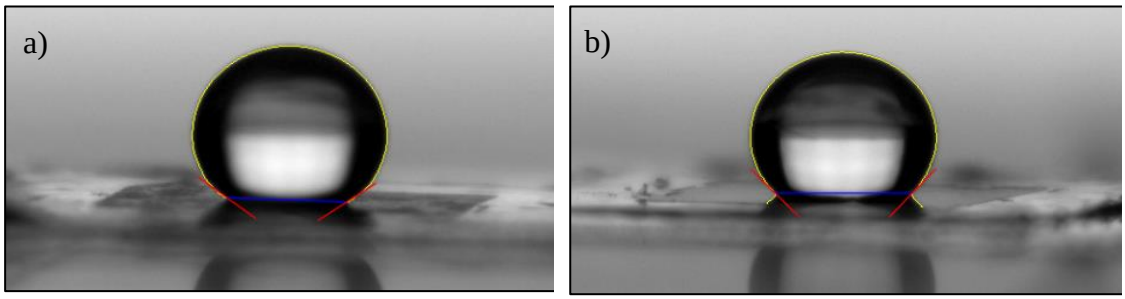

Fig. 4-3 Contact angle of a water drop on Parylene C 500 nm/2 μm bubble tip (1,4 μm diameter) structures with: (a) untreated surface (144°) and (b) plasma treated surface (133°).

The results of contact angle measurements on the bubble structure surface (fig. 4-3) are surprisingly similar to the results on the pillars. In both cases, however, oxygen plasma treated structures showed minor decrease in contact angle, but it is negligible. Worth mentioning might also be contact angle measurements of different surface modifications of flat Parylene C (deposited on silicon). APTES showed an angle of 63° on the Parylene and SiO_2 phase (fig. 4-4a) which was expected. A higher angle on fig. 4-4b probably means, that no silane link occurred. A very hydrophilic surface of ALD silicon oxide is not surprising, but the angle is very close to oxygen plasma treated Parylene surface (fig. 4-4c). An attempt to link animal keratin onto the Parylene surface with no SiO_2 layer was made, but following the image on fig. 4-4d, its possible, it was unsuccessful.

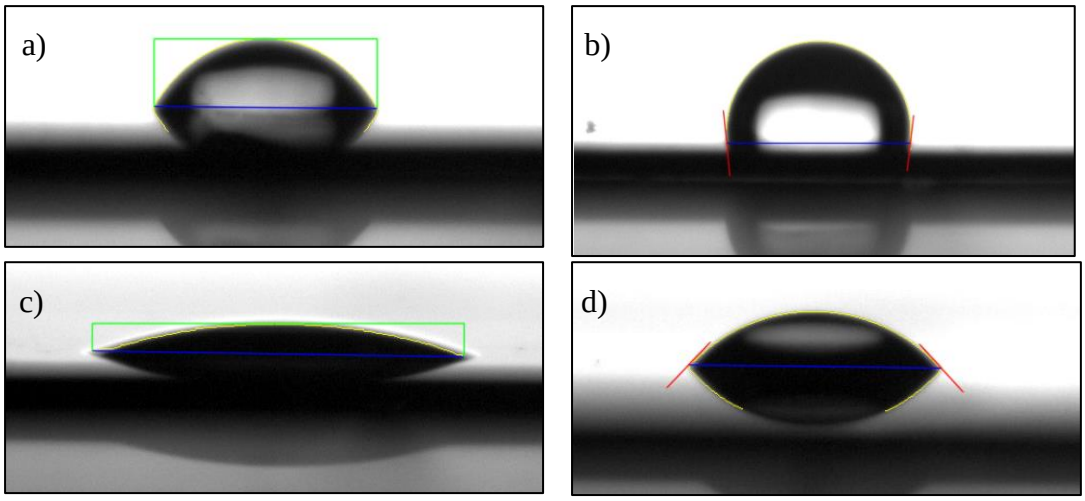

Fig. 4-4 (a)APTES on Parylene C + ALD SiO_2 (63°); (b) APTES on Parylene C (96°); (c) ALD SiO_2 on Parylene C (18°); (d) Parylene C with ALD SiO_2 + APTES and Glutaraldehyde crosslinkers for β-keratin (47°)

4.2 AFM measurements

AFM measurements were carried out with an ICON-SPM Bruker in AFM – contact mode and also two different cantilevers were used: a tip-less cantilever from ScanSens GmbH model: CSG01/TL/15 with a spring constant of k = 0.1 - 0.6 $N.m^{-1}$ and a custom modified ScanSens tip-less cantilever of same model.

4.2.1 Creating custom made spherical tip cantilever

A CSG01 cantilever had a glass sphere of ~100 μm glued as a tip with the help of an epoxy adhesive while the cantilever was mounted onto the probe station. The procedure is shown on Fig. 4-5.

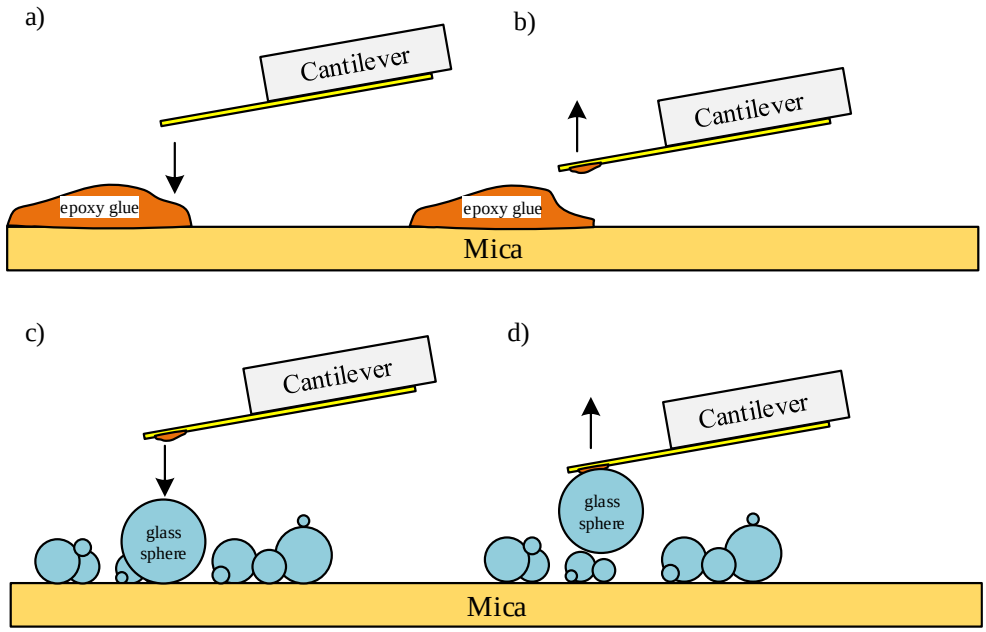

Fig. 4-5 Mounting of glass sphere onto the tip-less cantilever: (a) steadily approaching the surface with epoxy adhesive; (b) as the adhesive is applied, the cantilever moves above a spill of glass spheres; (c) approaching a fitting sphere and waiting for a few seconds; (d) the glass sphere is glued onto the cantilever and it waits to dry.

This glass-sphere mounted cantilever was specifically made for measuring adhesive forces on Parylene C structures (pillars and bubbles). At the sample-tip connection it would comply to the flexible structures better than a tip-less cantilever and might measure a local adhesion force of a group of pillars/bubbles.

The original cantilever's properties are listed in Table 4-1 and will all change after glass sphere has been mounted (except the spring constant *k*). Custom created glass sphere cantilever is on Fig. 4-6.

Table 4-1 Physical properties of CSG01/TL/15 cantilevers (according to manufacturer).

Length [μm]	Width [μm]	Thickness [μm]	Resonant frequency [kHz]	Spring constant *k* [$N.m_{-1}$]
450 ± 5	49	2,5	11 - 19	0,1 – 0,6

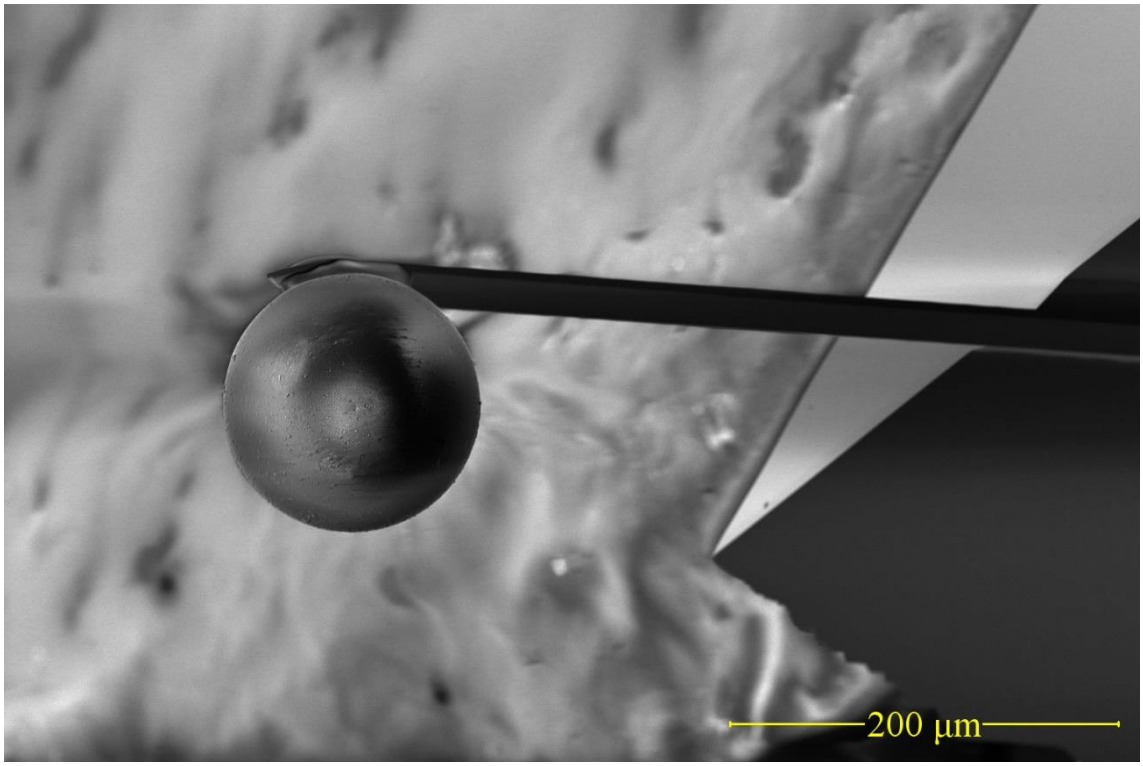

Fig. 4-6 An SEM image of the glass sphere mounted on ScanSens cantilever.

4.2.2 Force-distance Curves

The force curves were measured on three Parylene surfaces: a flat, unstructured surface and structured surfaces (pillars and bubbles). Tested were also variations, where another same three surfaces were cured with oxygen plasma (using parameters from chapter 3.6). The measurements and AFM control has been done with a Bruker software tool Nanoscope 9.6.

Before measurement (and after each cantilever exchange) the parameter calibration of both cantilevers, which were used, had taken place. Especially the deflection sensitivity has been updated and the spring constant *k* was determined from Thermal Tune tool. Both cantilevers had the same *k* value of 0,2 $N.m^{-1}$, which is important for adhesion force calculations from cantilever deflection. Another influential factor is relative air humidity, which varied from 40 – 50% and had often taken negative effect on the measurements, when surface humidity caused high tip-to-surface capillary adhesion. That also had to be taken into consideration.

Figures from 4-9 to 4-14 show all six adhesion force plots of studied samples. The resulting adhesion force difference between untreated and oxygen plasma treated flat Parylene C surface correlates with findings in chapter 4.1, where the contact angle difference was expected. Measurements on the structures, once again, have shown that there is no great difference between structured surface properties which have been treated with oxygen plasma, and those that haven't. The adhesion force was measured as a difference between points marked *a* and *f* in the plots.

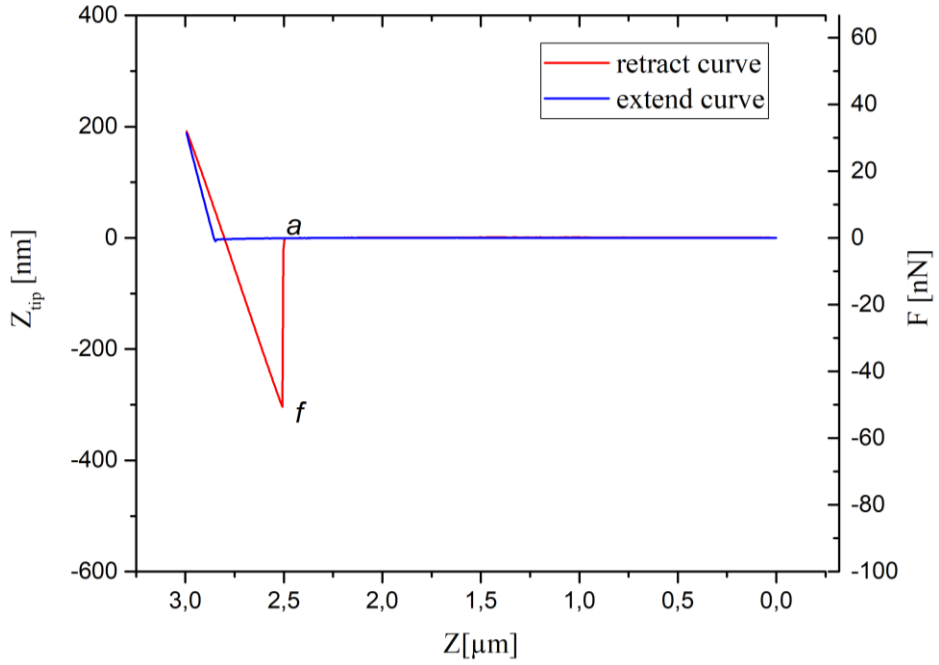

Fig. 4-7 Tip-less ScanSens probe – on flat Parylene C cured with O_2 (force ~ 69 nN). Graph zero is fit to extend curve.

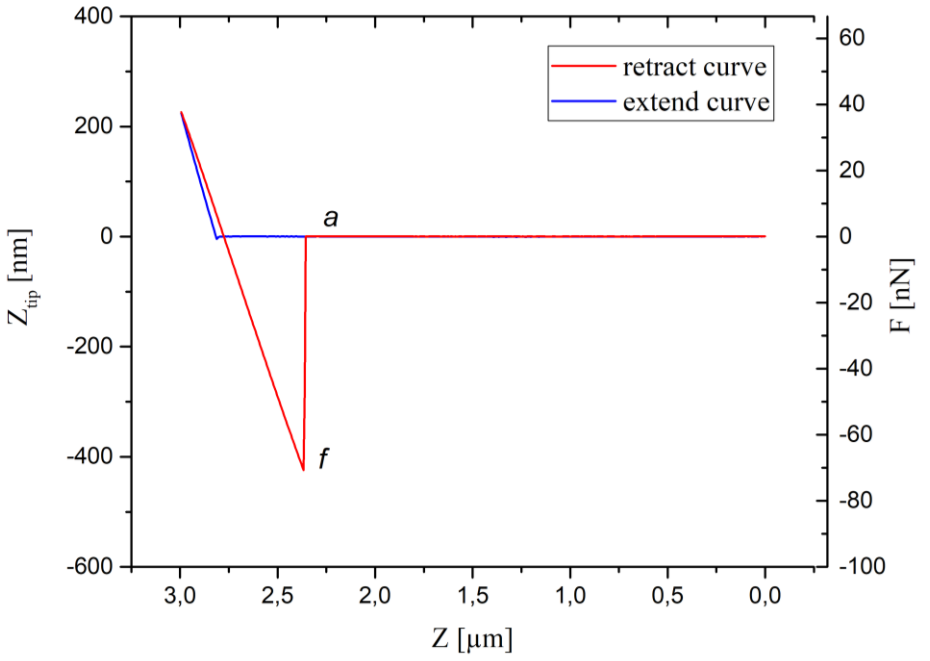

Fig. 4-8 Tip-less ScanSens – flat Par. C (force ~ 49 nN).

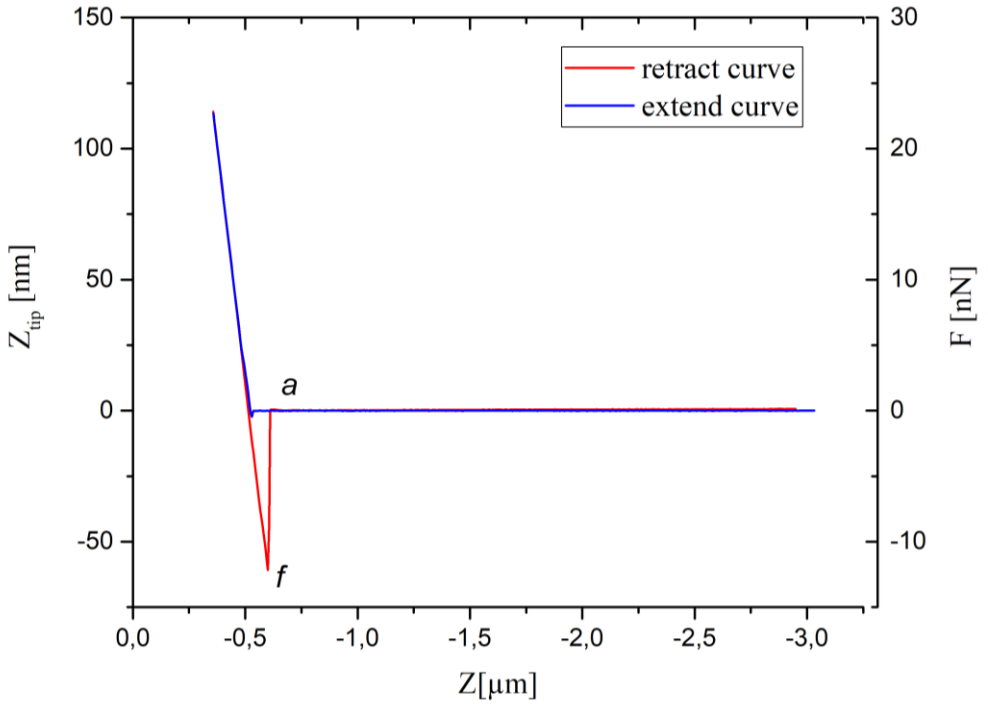

Fig. 4-9 Glass sphere mounted ScanSens probe – on pillar structured sample (0,5/1 µm), untreated (force ~ 13 nN).

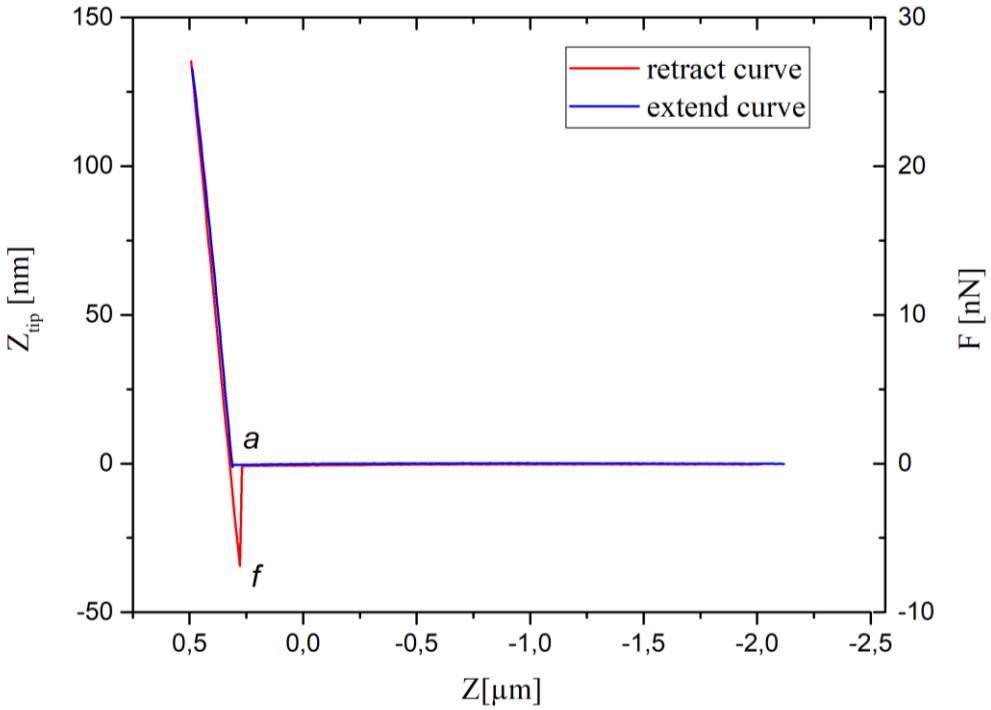

Fig. 4-10 Glass sphere mounted ScanSens probe – on pillar structured sample (0,5/1 µm), treated with O_2 plasma (force ~ 7 nN).

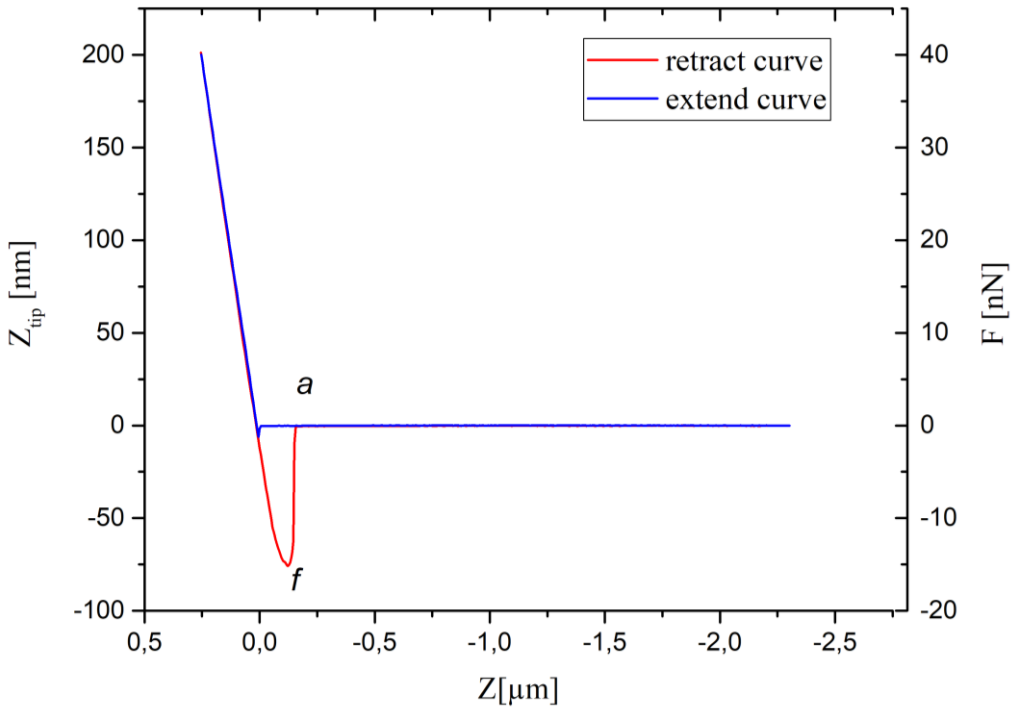

Fig. 4-11 Glass sphere mounted ScanSens probe – measurement on bubbles sample (0,5/2 µm), not treated (force ~ 16 nN).

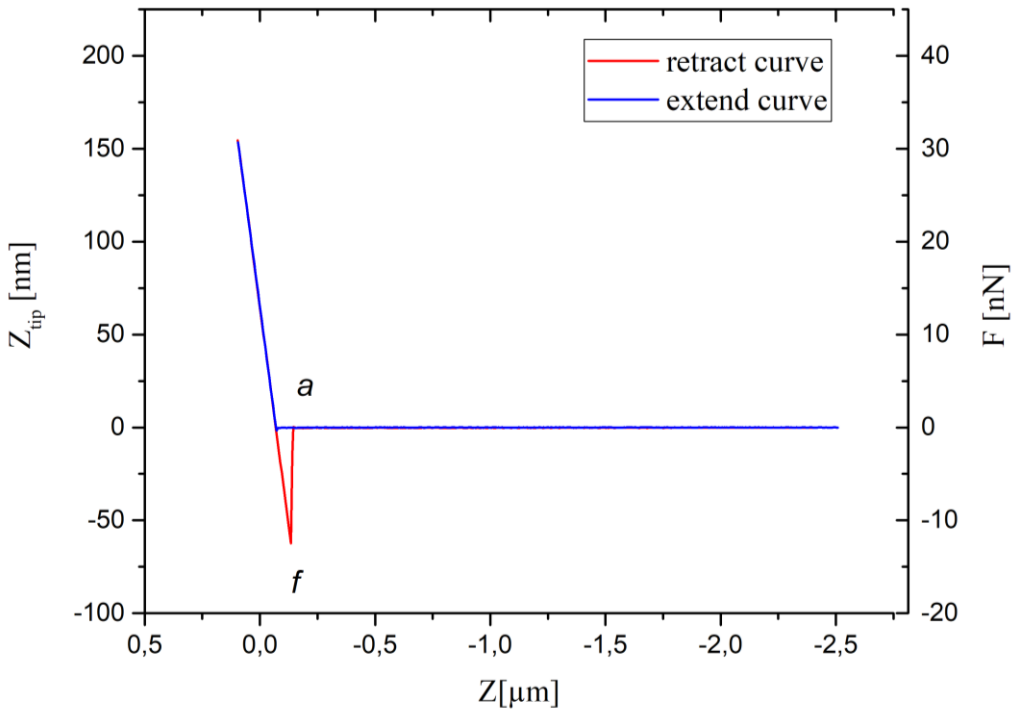

Fig. 4-12 Glass sphere mounted ScanSens probe – measurement on bubbles sample (0,5/2 µm) treated with O_2 plasma (force ~ 13 nN).

5 CONCLUSIONS

Researching this work's topic, *Gecko mimicking surfaces*, showed, that there have been numerous attempts to create structures simulating adhesion properties of a gecko (especially the Tokay Gecko) and some ideas to create functional biomimetics have been successful. Some interest has also arisen in the commercial sphere with the prospect of utilizing aforementioned qualities for production of dry adhesives, that would be able to stick to almost any surfaces.

A consensus has not yet been stated among scientists conducting research regarding adhesion of gecko setae. There are three main factors, which play a role: weak van der Waals forces, capillary forces, and electrostatic forces, that require further research to establish which one is dominant.

Prior to that, some structures have been created for measurements. Prepared were micropillars made of polymer Parylene C, which might have some comparable mechanical properties with biological setae of a gecko (such as stiffness, etc.). Improving the tips of the micropillars with bubbles was also accomplished and their conformality (due to being hollow) mechanically resembles a set of gecko lamellae. Next aim was modifying the surfaces of these micropillars and bubbles with materials harbouring better adhesion when bind to other materials, such as silicon dioxide SiO_2 and a crosslinker (SiO_2-APTES/GTA), to promote bonding of β-keratin.

As was discussed in chapter 3.6, some of the surface modifications implementations failed in being applied on Parylene C structures. One of the important ones, plasma enhanced ALD growth of SiO_2 is too destructible. However, there are methods of oxide growth in ALD, which do not require plasma activation pulses. Thermal processes, that use water or ozone [37] [38] exist, but would need to be accommodated for available equipment, which was used for progression purposes of this work. There are also different techniques of SiO_2 deposition, including magnetron sputtering and PECVD (it's also plasma enhanced, but grow rates are much higher [39]).

These reasons ruined the intentions of applying crosslinkers to created structures, but an attempt to bind the crosslinkers directly onto Parylene C was made, without the intermediate oxide layer. The contact angle measurements haven't concluded, if the binding of silanes, or even crosslinking keratin took place. A rather advanced methods of chemical characterisation are required.

The results of this work demonstrate, that it is very much possible to create desired structures and even the simplest modifications can change their surface properties considerably.

6 REFERENCES

[1] K. Autumn and J. Puthoff, "Properties, Principles, and Parameters of the Gecko Adhesive System," in *Biological Adhesives*, A. M. Smith, Ed., ed Cham: Springer International Publishing, 2016, pp. 245-280.

[2] B. Bhushan, "Bioinspired structured surfaces," *Langmuir,* vol. 28, pp. 1698-714, Jan 24 2012.

[3] M. Carlo and S. Metin, "A Biomimetic Climbing Robot Based on the Gecko," *Journal of Bionic Engineering,* vol. 3, pp. 115-125, 2006/09/01/ 2006.

[4] A. K. Geim, S. V. Dubonos, I. V. Grigorieva, K. S. Novoselov, A. A. Zhukov, and S. Y. Shapoval, "Microfabricated adhesive mimicking gecko foot-hair," *Nat Mater,* vol. 2, pp. 461-3, Jul 2003.

[5] H. Lee, B. P. Lee, and P. B. Messersmith, "A reversible wet/dry adhesive inspired by mussels and geckos," *Nature,* vol. 448, pp. 338-41, Jul 19 2007.

[6] M. T. Northen and K. L. Turner, "A batch fabricated biomimetic dry adhesive," *Nanotechnology,* vol. 16, pp. 1159-1166, 2005.

[7] H. Izadi, K. M. Stewart, and A. Penlidis, "Role of contact electrification and electrostatic interactions in gecko adhesion," *J R Soc Interface,* vol. 11, p. 20140371, Sep 6 2014.

[8] W. Federle, "Why are so many adhesive pads hairy?," *J Exp Biol,* vol. 209, pp. 2611-21, Jul 2006.

[9] R. G. Beutel and S. N. Gorb, "Ultrastructure of attachment specializations of hexapods, (Arthropoda): evolutionary patterns inferred from a revised ordinal phylogeny," *Journal of Zoological Systematics and Evolutionary Research,* vol. 39, pp. 177-207, Dec 2001.

[10] G. Cao, *Nanostructures & Nanomaterials: Synthesis, Properties & Applications*: Imperial College Press, 2004.

[11] H. L. Liu and G. X. Cao, "Effectiveness of the Young-Laplace equation at nanoscale," *Scientific Reports,* vol. 6, Apr 1 2016.

[12] R. G. Horn and D. T. Smith, "Contact Electrification and Adhesion between Dissimilar Materials," *Science,* vol. 256, pp. 362-364, Apr 17 1992.

[13] K. Nojiri, *Dry Etching Technology for Semiconductors*: Springer International Publishing, 2014.

[14] S. Franssila and L. Sainiemi, "Reactive Ion Etching (RIE)," ed, 2015, pp. 2911-2921.

[15] H. V. Jansen, M. J. de Boer, S. Unnikrishnan, M. C. Louwerse, and M. C. Elwenspoek, "Black silicon method X: a review on high speed and selective plasma etching of silicon with profile control: an in-depth comparison between Bosch and cryostat DRIE processes as a roadmap to next generation equipment," *Journal of Micromechanics and Microengineering,* vol. 19, Mar 2009.

[16] I. Gablech, J. Somer, Z. Fohlerova, V. Svatos, J. Pekarek, S. Kurdik, *et al.*, "Fabrication of buried microfluidic channels with observation windows using femtosecond laser photoablation and parylene-C coating," *Microfluidics and Nanofluidics,* vol. 22, Sep 2018.

[17] D. H. Xu, B. Xiong, G. Q. Wu, Y. C. Wang, X. Sun, and Y. L. Wang, "Isotropic Silicon Etching With XeF2 Gas for Wafer-Level Micromachining Applications," *Journal of Microelectromechanical Systems,* vol. 21, pp. 1436-1444, Dec 2012.

[18] "PDS 2010 LABCOTER™ 2 Parylene Deposition System: Operator's Manual," Rev 37 ed: Specialty Coating Systems, 2004.

[19] H. Kim and K. Najafi, "Characterization of low-temperature wafer bonding using thin-film parylene," *Journal of Microelectromechanical Systems,* vol. 14, pp. 1347-1355, 2005.

[20] P. D. Uwe Stöhr, "Surface activation of plastics by plasma for adhesion promotion," P. E. GmbH, Ed., ed: WOTech Technical Media, 2016, p. 9.

[21] M. Lessel, O. Baumchen, M. Klos, H. Hahl, R. Fetzer, M. Paulus, *et al.*, "Self-assembled silane monolayers: an efficient step-by-step recipe for high-quality, low energy surfaces," *Surface and Interface Analysis,* vol. 47, pp. 557-564, May 2015.

[22] P. G. Pape, "15 - Adhesion Promoters," in *Handbook of Adhesives and Surface Preparation*, S. Ebnesajjad, Ed., ed Oxford: William Andrew Publishing, 2011, pp. 369-386.

[23] R. W. Johnson, A. Hultqvist, and S. F. Bent, "A brief review of atomic layer deposition: from fundamentals to applications," *Materials Today,* vol. 17, pp. 236-246, 2014/06/01/ 2014.

[24] S. Thapa, "DEFECTS AND FERROMAGNETISM IN TRANSITION METAL DOPED ZINC OXIDE," 2016.

[25] P. Bouckenooge, H. Terryn, and I. Vandendael, "Ultimate Lateral Resolution in Electron Microscopy by FE-Auger."

[26] B. Voigtländer, *Scanning probe microscopy : atomic force microscopy and scanning tunneling microscopy*. Heidelberg: Springer Heideberg New York Dordrecht London, 2015.

[27] G. Goring, P. I. Dietrich, M. Blaicher, S. Sharma, J. G. Korvink, T. Schimmel, *et al.*, "Tailored probes for atomic force microscopy fabricated by two-photon polymerization," *Applied Physics Letters,* vol. 109, Aug 8 2016.

[28] Bruker. (2010). *SPM Training Guide*. Available: http://www.nanophys.kth.se/nanophys/facilities/nfl/afm/icon/bruker-help/Content/SPM%20Training%20Guide/SPM%20Training%20Guide.htm

[29] R. S. Hebbar, A. M. Isloor, and A. F. Ismail, "Chapter 12 - Contact Angle Measurements," in *Membrane Characterization*, N. Hilal, A. F. Ismail, T. Matsuura, and D. Oatley-Radcliffe, Eds., ed: Elsevier, 2017, pp. 219-255.

[30] S. S. Latthe, C. Terashima, K. Nakata, and A. Fujishima, "Superhydrophobic Surfaces Developed by Mimicking Hierarchical Surface Morphology of Lotus Leaf," *Molecules,* vol. 19, 2014.

[31] Y.-C. Tsai and W.-P. Shih, "Artificial Petal Effect on Nanofibrillar Parylene™ Surface," *The Journal of Adhesion,* vol. 88, pp. 32-54, 2012/01/01 2012.

[32] A. Marmur, "Equilibrium contact angles: Theory and measurement," *Colloids and Surfaces a-Physicochemical and Engineering Aspects,* vol. 116, pp. 55-61, Sep 16 1996.

[33] S. D. Strauss, *The Big Idea: How Business Innovators Get Great Ideas to Market*: Dearborn Trade Pub., 2002.

[34] O. I. P. Technology. (2019, 19 May 2019). The Bosch Process for Etching Micro-Mechanical Systems (MEMS) - Principles, Advances and Applications. Available: https://www.azonano.com/article.aspx?ArticleID=2738

[35] K. Miller, M. X. Li, K. M. Walsh, and X. A. Fu, "The effects of DRIE operational parameters on vertically aligned micropillar arrays," *Journal of Micromechanics and Microengineering,* vol. 23, Mar 2013.

[36] A. Tanioka, N. Fukushima, K. Hasegawa, K. Miyasaka, and N. Takahashi, "Permeation of gases across the poly(chloro-p-xylylene) membrane," *Journal of Applied Polymer Science,* vol. 54, pp. 219-229, 1994/10/10 1994.

[37] D. Hiller, R. Zierold, J. Bachmann, M. Alexe, Y. Yang, J. W. Gerlach, *et al.*, "Low temperature silicon dioxide by thermal atomic layer deposition: Investigation of material properties," *Journal of Applied Physics,* vol. 107, p. 064314, 2010/03/15 2010.

[38] L. Han and Z. David Chen, *Ultrathin SiO2 Films Grown by Atomic Layer Deposition Using Tris(dimethylamino)silane (TDMAS) and Ozone* vol. 58, 2013.

[39] S. Ping, L. Jie, G. Shang, L. Ping, W. Xiao, S. L. Wu, *et al.*, "PECVD Grown SiO2 Film Process Optimization," *Silicon Photonics Vi,* vol. 7943, 2011.

LIST OF SYMBOLS AND ABREVIATIONS

Abbreviation	Full name
AFM	…Atomic force microscopy
ALD	…Atomic layer deposition
APTES	…3-(aminopropyl)triethoxysilane
BSE	…Backscattered electrons
CCP	…Capacitively coupled plasma
CE	…Contact electrification
DRIE	…Deep reactive ion etching
DWL	…Direct write laser
EUV	…Extreme ultraviolet
FEG	…Field emission gun
GTA	…Glutaraldehyde
HMDS	…Hexamethyldisilane
ICP	…Inductively coupled plasma
M(N)EMS	…Micro-(Nano-)electromechanical systems
PBS	…Potassium-phosphate buffer solution
(PE)CVD	…(Plasma enhanced) Chemical vapor deposition
PDMS	…Polydimethylsiloxane
PP	…Polypropylene
PR	…Photoresist
PVC	…Polyvinylchloride
PVD	…Physical vapor deposition
RF	…Radio frequency
RIE	…Reactive ion etching
SE	…Secondary electrons
SEM	…Scanning electron microscopy
SPM	…Scanning probe microscopy
STM	…Scanning tunnelling microscopy
TDMAS	…Tris(dimetylamino)silane
TMAH	…Tetramethylammonium hydroxide

Symbol	Meaning	Units
ϵ_o	…Permittivity in vacuum	[$F.m^{-1}$]
γ	…Liquid surface tension	[$N.m^{-1}$]
σ_s	…Magnitude of charge per unit area	[$C.m^{-2}$]
Φ_A	…Van der Waals attraction	[J]
A_i	…Hamaker constant	[J]
F_A	…Force per unit area	[$N.m^{-2}$]
NA	…Numerical aperture	[-]
Δp	…Pressure difference (liquid surface)	[Pa]
Q	…Gas flow	[$cm^3.min^{-1}$]
R	…Resolving power (resolution)	[m]
K	…Spring constant	[$N.m^{-1}$]
θ	…Contact angle	[°]
R_f	…Roughness factor	[-]

LIST OF FIGURES

LIST OF TABLES